

## **UC Santa Cruz**

### **UC Santa Cruz Electronic Theses and Dissertations**

#### **Title**

Ion Conducting Materials and Devices for Bioelectronics

#### **Permalink**

<https://escholarship.org/uc/item/22c3f3f0>

#### **Author**

Jia, Manping

#### **Publication Date**

2021

Peer reviewed|Thesis/dissertation

UNIVERSITY OF CALIFORNIA

SANTA CRUZ

**Ion Conducting Materials and Devices for Bioelectronics**

**A dissertation submitted in partial satisfaction**

**of the requirements for the degree of**

DOCTOR OF PHILOSOPHY

in

ELECTRICAL AND COMPUTER ENGINEERING

by

**Manping Jia**

December 2021

The Dissertation of Manping Jia is approved by:

---

Professor Marco Rolandi, chair

---

Professor Holger Schmidt

---

Professor Nobuhiko Kobayashi

---

Peter F. Biehl  
Vice Provost and Dean of Graduate Studies



## Table of Contents

<b>INTRODUCTION .....</b>	<b>1</b>
<b>1. Bioelectronics.....</b>	<b>1</b>
<b>2. Materials in bioelectronic devices.....</b>	<b>7</b>
<b>2.1 Metals and metal nanoparticles.....</b>	<b>7</b>
<b>2.2 Conducting polymers and carbon materials .....</b>	<b>8</b>
<b>2.3 Proton/Ion Conducting Materials .....</b>	<b>9</b>
<b>3. Ion Transport Mechanism .....</b>	<b>12</b>
<b>RESEARCH CONTRIBUTION .....</b>	<b>21</b>
<b>4. Measuring Proton Conductivity .....</b>	<b>21</b>
<b>4.1 Proton conductivity of Glycosaminoglycans .....</b>	<b>21</b>
4.1.1 Introduction.....	22
4.1.2 Materials and Methods.....	24
4.1.3 Results and Discussion .....	26
4.1.4 Conclusions.....	34
<b>4.2 Proton conductivity of the gel within the electrosensory organs of cartilaginous fishes.....</b>	<b>36</b>
4.2.1 Introduction.....	36
4.2.2 Result .....	39
4.2.3 Discussion .....	43
4.2.4 Limitations of the study .....	46
<b>4.3 Proton conductivity of Single-Crystal Polycationic Polymers .....</b>	<b>47</b>
4.3.1 Introduction.....	48
4.3.2 Proton Conductivity .....	51
4.3.3 Conclusion .....	55
<b>4.4 Proton conductivity of Nanotubes .....</b>	<b>57</b>
4.4.2 Result and discussion.....	61
4.4.4 Experiment section.....	67
<b>5. Ion Conducting Hydrogel.....</b>	<b>70</b>
<b>5.1 Introduction.....</b>	<b>70</b>
<b>5.2 Results .....</b>	<b>74</b>
<b>5.3 Conclusion .....</b>	<b>90</b>
<b>5.4 Experiments section .....</b>	<b>91</b>
<b>6. Electrophoretic Delivery of ions and biomolecules with bioelectronic devices 94</b>	

<b>6.1 Delivery of Acetylcholine by polyelectrolyte hydrogel .....</b>	<b>94</b>
<b>6.2 Chloride pump .....</b>	<b>107</b>
6.2.1 Introduction.....	107
6.2.2 Cl <sup>-</sup> to electron transducer .....	109
6.2.3 Kinetics of the conversion between Ag and AgCl.....	113
6.2.4 Chloride modulator with cells.....	120
6.2.5 Conclusion .....	125
6.2.6 Experiment section.....	126
<b>6.3 Four-ion pump .....</b>	<b>132</b>
6.3.1. Introduction.....	132
6.3.2. Result and Discussion .....	134
6.3.3 Conclusion .....	141
6.2.4 Experiment section: .....	142
<b>7. Outlook .....</b>	<b>147</b>
<b>8. Reference .....</b>	<b>149</b>

## Table of Figure

Figure 1 Comparison of Young's moduli and ion conductivity of cell/tissue and materials commonly used at the bioelectronics interface. Metals are much stiffer than cells and tissue; polymers are relatively softer and can be ion-conducting, which is a critical property for electron-to-ion signal conversion at the interface; hydrogels have similar Young's modulus as cells and tissue and are ion conductors. .... 2

Figure 2 Iontronic components and applications. The basic OEIP structure for a) selective cation transport and b) selective anion transport. Ionic bipolar membrane diodes with c) lateral junction and d) stacked junction; zoom shows accumulation and depletion of the BM junction in forward and reverse bias. e) npn-IBJT in forward bias. f) pnp-IBJT with a neutral junction; zoom shows accumulation and depletion of the neutral junction in forward and reverse bias. g) Collection of iontronic components in applied systems, including from left to right the bioelectronic neural pixel,<sup>36</sup> fast vertical release devices, and freestanding OEIPs. Varying chemical stimulation gives varying cellular response that can be monitored externally or internally by, for example, optical read-out or electrical sensing.<sup>24</sup> ..... 4

Figure 3 (A) Grotthuss mechanism for the conduction of  $H^+$  as hydronium ion along proton wires. (B) An equivalent mechanism for  $OH^-$  conductivity as proton hole along proton wire. .... 14

Figure 4 Energy diagram representation of conduction in hydrogen bonded proton wire. (a) A wire with no  $H^+$  or  $OH^-$  defect does not conduct. (b) For an intrinsic proton wire, the protochemical potential  $\mu_{(H^+)H1}$  is in the middle of the bandgap. (c) An acid donates a  $H^+$  into the conduction band of a proton wire to yield a  $H^+$ -type protonic conductor. (d) A base accepts a  $H^+$  to create a  $OH^-$  (proton hole) in the valence band of a proton wire to yield a  $OH^-$ -type protonic conductor.<sup>320</sup>, with permission from Nature. .... 16

Figure 5 (a) Schematic showing setup for impedance spectroscopy on a hydrogel. The gel is sandwiched in between two electrodes and upon applying an electrical signal, electrical double layers are formed at both the electrodes. (b) Equivalent circuit for the setup described in (a) where  $C_e$  represents the capacitance of the electrical double layers,  $C$  represents the capacitance formed by the electrodes and  $R$  shows the resistance of the bulk electrolyte, (c) Real and imaginary parts of the impedance calculated using impedance spectroscopy. .... 18

Figure 6 (a) Given a negative potential,  $H^+$  is first adsorbed onto the surface of Pd ( $Pd_{ads}$ ), then absorbed into the subsurface layer,  $Pd_{subs}$ , and further diffuses into bulk Pd to form  $PdH_{bulk}$ . (b) Given a positive potential,  $H^+$  is first released from the surface,  $PdH_{ads}$ , then from the subsurface layer ( $Pd_{subs}$ ) to the surface ( $Pd_{ads}$ ) and further diffuses from  $PdH_{bulk}$ . .... 19

Figure 7 The keratan sulfate.(A) Chemical structure of KS. (B) An illustration of a three-monomer segment of KS. Possible intra- and inter-molecular hydrogen bonds as well as the hydrogen bonds between the water of hydration and the polar parts of the molecule form a continuous network comprised by hydrogen-bond chains. The sulfate group interacts with the hydrogen-bond network and forms an H<sub>3</sub>O<sup>+</sup> (hydronium) ion. .... 24

Figure 8 Proton conduction measurement of KS. A) Palladium hydride (PdH<sub>x</sub>) electrode behavior. Under a VSD, PdH<sub>x</sub> source split into Pd, H<sup>+</sup>, and e<sup>-</sup>. Protons are injected into the KS, whereas electrons travel through external circuitry and are measured. B) TLM geometry. Varying the distance between source and drain (LSD) distinguishes between the fixed PdH<sub>x</sub> – KS interface contact resistance and the varying bulk resistance. C) Optical image of TLM geometry with hydrated KS on the surface. Scale bar, 500 μm. D) Transient response to a 1V bias in KS at 75%, 90%, 90% H<sub>2</sub> RH, in which the current under 90% with hydrogen is much higher than that under 90% RH without hydrogen. E) Deuterium current (black) at 90% D<sub>2</sub> humidity is lower than proton current (red). F) The normalized resistance RLN as a function of LSD, A linear fit gives a bulk material proton conductivity of 0.50 ± 0.11 mS cm<sup>-1</sup>. 27

Figure 9 Current under different RH of GAGs family: (a) hyaluronic acid, (b) heparan sulfate, (c) chondroitin sulfate A and (d) dermatan sulfate. The current under 90%RH with hydrogen is much higher than 90%RH without hydrogen. .... 30

Figure 10 Kinetic isotope effect in members of GAGs family: (a) hyaluronic acid, (b) heparan sulfate, (c) chondroitin sulfate A and (d) dermatan sulfate. Current measured in a 5% deuterium (black) atmosphere at 90%RH vs a 5% proton atmosphere at 90%RH (red). .... 31

Figure 11 Control experiments on Nafion. Conductivity of Nafion measured with this TLM device is 58.3 ± 2.5 mS cm<sup>-1</sup>. It's slightly lower than the literature value of 78 mS cm<sup>-1</sup>, which is attributed to sample preparation. The reported literature value is after immersion in heated sulfuric acid, while the sample here was simply drop-cast from solution. .... 33

Figure 12 Anatomy of Ampullae of Lorenzini (AoL)(A) An image showing a type of chimaera called a spotted ratfish (*Hydrolagus collieii*). Yellow arrowheads delineate the locations of some AoL pores. Image taken by Mick Otten.(B) A diagram showing three AoL below the skin surface. Pores lead into canals filled with a gel (as made visible by the cutaway). Neurons (yellow) synapse with specialized electrosensory cells in the alveoli and project onto the hindbrain. .... 37

Figure 13 Proton conductivity of *H. collieii* AoL gel before and after proteinase K digestion. Two-terminal device used for EIS measurement. .... 41

Figure 14 Nyquist plots of native AoL gel (blue) and digested AoL gel (black) at 90% relative humidity. ....	41
Figure 15 Equivalent circuit model. A constant phase element (CPE) was used to describe the nonideal interface capacitance; $R_b$ and $C_b$ represent the resistance and capacitance of the sample, respectively. ....	42
Figure 16 Nyquist plots of native <i>H. colliciei</i> AoL gel (D) and proteinase-K-digested <i>H. colliciei</i> AoL gel (E) in the presence of H <sub>2</sub> O vapor (black) and D <sub>2</sub> O vapor (red). ....	42
Figure 17 Design concept and strategy for the synthesis of single-crystalline polycationic polymers. (a) Schematic diagram for the preparation of polymer crystals from the crystallization of preorganized monomers, followed by the topochemical photopolymerization. (b) The unfavorable self-repulsive interaction in a parallel manner. (c) The self-complementary interactions facilitate the proximity of two reactive sites in an antiparallel manner. (d) Structural formula of the monomer. (e) Scheme for photopolymerization. ....	50
Figure 18 Nyquist plots showing the impedance of the polymer at 298 K with varying relative humidity (RH) between 0.1 MHz and 0.1 Hz. The Nyquist plots of 50%–90% RH are also shown in Figure S34 in detail. (e) The dependence of the proton conductivity of the polymer on the RH. (f) A snapshot of water chains in the 1D channels of the simulated structure. H <sub>2</sub> O molecules are illustrated as space-filling representations, while the organic fragments and BF <sub>4</sub> <sup>-</sup> counterions are shown as surface model representations. ....	52
Figure 19 Two-terminal device used for EIS measurement. The two-terminal devices used in EIS measurements were fabricated on glass. Prior to device fabrication, the substrates were cleaned by sequential sonication in Me <sub>2</sub> CO and iPrOH. Then, a 10 nm Titanium adhesion layer overlaid with a 100 nm gold was electron-beam evaporated onto the clean substrates through a shadow mask. The dimensions of the paired electrodes were 2.5 cm wide by 2.0 cm long with an inter-electrode separation of 50 μm. The devices were completed by dropping cast the bulk polymer powders suspended in MeCN solution directly onto the electrode patterns, and the resulting films were allowed to dry in air overnight. ....	52
Figure 20 Equivalent circuit model used to fit the impedance data. A Constant Phase Element (CPE) was used to describe the non-ideal interface capacitance, $R_b$ and $C_b$ represent the resistance and capacitance of the sample, respectively. ....	53
Figure 21 Nyquist plots showing the impedance of the polymer between 0.1 MHz–0.1 Hz at 298 K with varying RH. Zoom-in of Figure 18. ....	54
Figure 22 Kinetic isotope effect of the polymer at 90% RH. A Nyquist plot for the polymer-bridged two-terminal device in the presence of water vapour (black) and in	



the presence of deuterium oxide vapour (red). The conductivity calculated from the Nyquist plots are  $3 \times 10^{-4} \text{ S cm}^{-1}$  ( $\text{H}^+$ ) and  $1.4 \times 10^{-4} \text{ S cm}^{-1}$  ( $\text{D}^+$ ), respectively ..... 54

Figure 23 Nyquist plot of Nafion at 90% RH, yielding a value of  $0.1 \text{ S cm}^{-1}$  ..... 55

Figure 24 Accessing high-aspect ratio nanotubes via acid-mediated macrocycle assembly. (Top) Previous work in which assembly under mild conditions was dictated by a pyridine-2,6-dicarboxaldehyde monomer residue, resulting in a system that assembles under mild conditions but is not easily generalized. (Bottom) A modular approach to imine-linked macrocycle formation and assembly relying on a pyridine junction embedded within the diamine monomer, allowing access to chemically and structurally diverse nanotubes in a single step..... 60

Figure 25 Structure-dependent proton conductivity of nanotubes prepared via acid-mediated macrocycle assembly. (A) Illustration of the two-terminal device used for EIS measurements. (B) Diagram of the equivalent circuit model used to analyze the impedance data. The circuit consists of a Constant Phase Element ( $\text{CPE}_{\text{int}}$ ) in series with both a resistor ( $R_b$ ) and a capacitor ( $C_b$ ), which correspond to the film/electrode interface capacitance, the film bulk resistance, and the film bulk capacitance, respectively. (C–F) Nyquist plots showing the impedance of nanotubes derived from DAPP-PDA, DAPP-PhenDA, DAPP-IDA, and DAPB-DFP macrocycles at  $25^\circ\text{C}$  with 90% R.H. The conductivities calculated from these plots were  $1.4 \times 10^{-5}$ ,  $6.3 \times 10^{-5}$ ,  $1.6 \times 10^{-3}$ , and  $1.5 \times 10^{-3} \text{ S m}^{-1}$ , respectively. (G) Comparison of observed conductivity values in different macrocycles. The data suggest that an increase in the size of the macrocycle results in lower conductivities, but other factors such as macrocycle shape and packing density may also play a role..... 62

Figure 26 Kinetic isotope effect experiment. Nyquist plots for the polymer-bridged two-terminal device in the presence of water vapor (black) and deuterium oxide vapor (red) of (A) DAPP-PDA, (B) DAPP-PhenDA, (C) DAPP-IDA, and (D) DAPB-DFP nanotubes at 90% R.H..... 65

Figure 27 Nyquist plot of DAPB-IDA nanotubes at 90% R.H..... 66

Figure 28 (a) Hydrogel polymerization reaction with AMPSA as the monomer, PEGDA as the crosslinker in the presence of the photo-initiator. (b) Schematic of the crosslinked polyelectrolyte hydrogel with fixed charges on the chain, counterions and water molecules in the polymeric network. (c) Optical image of the bulk hydrogel. Scale bar: 5 mm. (d) Schematic of the hydrogel ionic conductivity measurement experiment setup. A voltage ( $V$ ) across the AgCl electrodes drives  $\text{H}^+$  to move through the hydrogel in the capillary fiber, and the ionic flux is translated into an electronic current by the electrochemical reactions at the Ag/AgCl contacts. (e) Optical image of the hydrogel ionic conductivity measurement experiment setup. Scale bar: 5 mm. The hydrogel capillary fiber is between two electrolyte chambers

made from PDMS, and AgCl wires are used as the electrode contacts in each chamber. .....	74
Figure 29 Hydrogel resistor fabrication process.....	77
Figure 30 (a) The reaction between the glass and A174. (b) The reaction of hydrogel polymerization and covalent bonding in the glass capillary fiber. ....	77
Figure 31 (a) Ionic conductivity of hydrogels as a function of AMPSA and PEGDA content. With more AMPSA and less PEGDA, hydrogels exhibit higher conductivity. (b) Schematic of charge carrier density measurement using the ion exchange process. (c) Current response when we change the charge carrier from H <sup>+</sup> to K <sup>+</sup> . During the ion exchange process, the current under the gray area is integrated and leads to the charge carrier density. (d) Charge carrier density of the hydrogels as a function of AMPSA and PEGDA. The charge carrier density increases with AMPSA content because AMPSA directly provides charged sites, and slightly decreases with more PEGDA. (e) Effective diffusion coefficient (D <sub>eff</sub> ) of the hydrogels as a function of AMPSA and PEGDA. The D <sub>eff</sub> decreases with more AMPSA and shows no obvious trend while changing PEGDA. (f) Relationship between effective diffusion coefficient (D <sub>eff</sub> ) and bulk diffusion coefficient (D <sub>0</sub> ) of Na <sup>+</sup> , K <sup>+</sup> , H <sup>+</sup> , D <sup>+</sup> , DAPI in AP/2/0.5 hydrogel. ....	79
Figure 32. Dependence of ionic conductivity on AMPSA and PEGDA. ....	80
Figure 33 Dependence of charge carrier density on AMPSA and PEGDA ratio. ....	82
Figure 34 Dependence of effective diffusion coefficient (D <sub>eff</sub> ) on AMPSA and PEGDA. ....	83
Figure 35 (a) Schematic of water diffusing into the hydrogel due to osmotic pressure, which results in swelling of the hydrogel and enlarged pores. (b) Hydrogel swells in the glass capillary fiber. Scale bar: 2 mm. Optical images of swollen (c) AP/1/0.5, (d) AP/2/0.5, (e) AP/3/0.5, (f) AP/4/0.5, (g) AP/2/0.1, (h) AP/2/0.3, (i) AP/2/0.5, (j) AP/2/0.7 hydrogels. ....	85
Figure 36 SEM of hydrogels: (a) AP/1/0.5, (b) AP/2/0.5, (c) AP/3/0.5, (d) AP/4/0.5, (e) AP/2/0.1, (f) AP/2/0.3, (j) AP/2/0.5, (h) AP/2/0.7 hydrogels. Scale bar: 10 um. (i) Schematic of porosity. (j) Porosity change while changing AMPSA. (k) Porosity change while changing PEGDA. (l) Schematic of tortuosity. (m) Tortuosity change while changing AMPSA. (n) Tortuosity change while changing PEGDA.....	89
Figure 37 Swelling ratio of hydrogels as a function of AMPSA and PEGDA.....	90
Figure 38 Horizontal ion pump.....	94

Figure 39 Fabrication of hydrogel in the vertical ion pump. ....	95
Figure 40 Hydrogel swell out of the SU8 microfluidic channels into the target chamber when there is no silane treatment. ....	96
Figure 41 Reactions of SU8 surface treatment and hydrogel binding. ....	96
Figure 42 SU8 surface treatment by A174 in toluene. ....	97
Figure 43 SU8 surface treatment by A174 vapor in CVD. ....	98
Figure 44 Devices with SU8 surface treatment. ....	98
Figure 45 Hydrogels that swell too much break SU8 channels. ....	99
Figure 46 Molecules structure of acetylcholine. ....	100
Figure 47 Detection of acetylcholine. 200 $\mu$ M Amplex Red reagent, 0.1 U/mL choline oxidase, 0.5 U/mL acetylcholinesterase, 1U/mL HRP and the indicated amount of acetylcholine in 1X Reaction Buffer are contained in each reaction at ambient temperature. After approximately 30 mins, the measurement of fluorescence detection at $590 \pm 10$ nm was determined by a fluorescence microplate reader. ....	101
Figure 48 Photo of experimental setup for Ach <sup>+</sup> delivery of device, AgCl glass electrode and AgCl wire electrode contact are cathode and anode and immersed in two solutions, respectively; (B): Schematics of experimental setup. Target solution was 1x buffer with 300 $\mu$ L and the reservoir was 100 mM Acetylcholine chloride. ....	102
<i>Figure 49 The experimental result of channel 1 in device 1. According to the diagram, short running time is preferable with a high efficiency (~50 %). ....</i>	<i>103</i>
Figure 50 The experimental result of channel 2 in device 1. The diagram also shows that longer running time will result in low efficiency because of the depletion zone in the reservoir. ....	103
Figure 51 The experimental result of channel 1 in device 2. ....	104
Figure 52 Current data of three devices within 100 ms. ....	105
Figure 53 (A) COMSOL model of Ach <sup>+</sup> concentration after 100ms of Ach <sup>+</sup> injection. (B, C) FWHM at different heights above the ion pump pore from COMSOL model. ....	106
Figure 54 Schematic of prototype chloride transducer and working mechanism. This setup has a standard three-electrode configuration. MQAE is a fluorescence dye monitoring [Cl <sup>-</sup> ] change in solution, whose intensity increases with lower [Cl <sup>-</sup> ]. (a)	

Anodic voltage transfers  $\text{Cl}^-$  from solution into the Ag/AgCl contact, which decreases  $[\text{Cl}^-]$  and brightens MQAE. (b)  $[\text{Cl}^-]$  changes from 50 mM to 32 mM by applying 0.4 V for 100 s. (c) Cathodic voltage transfers  $\text{Cl}^-$  from the Ag/AgCl contact into solution thus increasing  $[\text{Cl}^-]$  and quenching MQAE. (d)  $[\text{Cl}^-]$  changes from 0 mM to 48 mM by applying -0.4 V for 100 s. .... 111

Figure 55 Stern–Volmer plot for quenching of MQAE by chloride. The volume of the solution is 20  $\mu\text{L}$ . .... 112

Figure 56 Selectivity of AgCl to  $\text{Cl}^-$  in stem cell culture media. .... 113

Figure 57 (a) Ag/ AgCl NPs electroplating and chlorination. (b-e) Morphology of Ag/AgCl NPs by SEM images of (b) Ag NPs after electroplating; (c) single Ag NPs with the signature shape; (d) Ag/AgCl with 20% chlorination; (e) Ag/AgCl with 40% chlorination. .... 116

Figure 58 Kinetics of the conversion between Ag/AgCl. (a) The linear relationship between  $V_{\text{OCP}}$  and logarithmic scale of  $[\text{Cl}^-]$  represents equilibrium as well as the threshold of Ag/AgCl conversion. In the white area above the line,  $\text{AgCl} + e^- \rightarrow \text{Ag} + \text{Cl}^-$ ; in the gray area under the line,  $\text{AgCl} + e^- \leftarrow \text{Ag} + \text{Cl}^-$ , (b) CV of Ag/AgCl electrodes with a series of scan rates, 20 mV/s, 40 mV/s, 60 mV/s, 80 mV/s, 100 mV/s. The redox peaks show that the reaction is electron transfer dominated, and the current increases with higher scan rate due to reduced diffusion layer. (c) Relationship of anodic peak current of Ag/AgCl ( $I_{\text{Cl}^-, \text{Peak}}$ ) versus square root of the scan rate in CV measurements. The excellent linear relationship shows that the reaction is limited by the diffusion of  $\text{Cl}^-$  to the electrode following Randles–Sevcik equation.<sup>285</sup> The standard error is derived from 3 electrodes. .... 117

Figure 59 Relationship of anodic peak current of Ag/AgCl ( $I_{\text{Cl}^-, \text{Peak}}$ ) versus square root of the scan rate in CV measurements of 3 AgCl NPs electrodes, which all show excellent linear relationship. .... 120

Figure 60 Chloride modulator. (a) Schematic of the chloride modulator (side view) and operating principle. Reservoir and target are connected by an anion exchange membrane (AEM), in which  $\text{Cl}^-$  are driven by  $V_{\text{Cl}^-, \text{R}}$ . Reservoir has a high  $[\text{Cl}^-]$  solution providing  $\text{Cl}^-$  source, and  $[\text{Cl}^-]$  in target is under control. (b) Optical image of the chloride modulator. The reservoir (black line) and target (red line) are separated by SU 8 microfluidic channels and the holes on the glass slide provides the inlet and outlet. (c)  $[\text{Cl}^-]$  change results from the 4-step process in Table 1 for 3 cycles, which is indicated by the MQAE fluorescence intensity. Temporal change corresponding to each step is shown with different colors in the second cycle as a representation. (d)  $V_{\text{mem}}$  change of cells results from the same operation is indicated by ArcLight fluorescence intensity. The data come from 3 devices. (e) Fluorescence images of the cells over MEAs with high  $V_{\text{mem}}$  ( $t = 75$  s) and low  $V_{\text{mem}}$  ( $t = 119$  s). The highlighted row is under operation. .... 122

Figure 61 Diffusion limited spatial resolution of the  $\text{Cl}^-$  modulator..... 124

Figure 62 Fabrication scheme for the proton pump array. (1) E-beam deposition of Au electrodes and traces. (2) Electrochemical deposition of Pd and Ag on the electrodes, followed by chlorination of Ag to form AgCl. (3) Parylene-C deposition. (4) Spin-coating of PVA: PDDA AEM and etching. (5) Parylene-C deposition. (6) SU8 patterning to form microfluidic walls. (7)  $\text{O}_2$  etch of Parylene-C to expose the ion bridge and the AgCl electrodes. (8) Spin-coating and patterning of the PVA: PSS CEM. (9) Sealing the fluidics with a thin microfluidic tap..... 129

Figure 63 (a) Schematic of multiple-ion pump. Each working electrode is independently controlled by voltage and able to deliver different ions. (b-e) optical image of the device (scale bar: 200  $\mu\text{m}$  for b and c, 500  $\mu\text{m}$  for d and e). b shows the different nanoparticles of microelectrodes. Every 4 microelectrodes form a group that can control  $\text{H}^+$ ,  $\text{K}^+$ ,  $\text{Na}^+$ ,  $\text{Cl}^-$ , respectively, and there are 3 x 3 matrix such groups. c shows the detailed position of four reservoirs and microelectrodes that are connected by ion channels. d shows the relative position of four reference electrodes in the reservoirs, microelectrodes and auxiliary electrode in the target. e shows the whole device including the geometry of microfluidic channels, and contact pads. .... 136

Figure 64 (a) Fluorescence image of 36 microelectrodes of the multi-ion pump. The four squares represent the microelectrodes that connected to four different reservoirs as a group. (b) The fluorescence intensity change of SNARF that indicates pH change, following the applied voltage: when  $V_1 = 1.6 \text{ V}$ ,  $\text{H}^+$  was delivered to the target, inducing pH decrease and fluorescence intensity decrease, vice versa. (c) The fluorescence intensity change of CoroNa that indicates  $[\text{Na}^+]$  change, following the applied voltage: when  $V_2 = 1.6 \text{ V}$ ,  $\text{Na}^+$  was delivered to the target, inducing  $[\text{Na}^+]$  increase and fluorescence intensity increase, vice versa. (d) The fluorescence intensity change of MQAE that indicates  $[\text{Cl}^-]$  change, following the applied voltage: when  $V_4 = -1.8 \text{ V}$ ,  $\text{Cl}^-$  was delivered to the target, inducing  $[\text{Cl}^-]$  increase and fluorescence intensity decrease, vice versa. (e) Fluorescence image of 4 microelectrodes that connected to four different reservoirs as a group. The yellow square represents the working electrode with applied voltage, and the four rectangulars represent the area where fluorescence intensity is measured. (f) The fluorescence intensity change of SNARF in the four rectangulars of e following the same protocol of b. (g) The fluorescence intensity change of CoroNa in the four rectangulars of e following the same protocol of b. (h) The fluorescence intensity change of MQAE in the four rectangulars of e following the same protocol of b..... 138

Figure 65 (a) -1.6 V was applied to the microelectrode in the black square versus the auxiliary electrode while 1.6 V was applied to the one in the blue square. (b) The fluorescence intensity in the black square went up, indicating pH increase, and meanwhile, the fluorescence intensity in the blue square went down, indicating pH decrease..... 140

Figure 66 Multi-ion pump controlled by machine learning with desired targets. .... 141

**Manping Jia**

**Ion Conducting Materials and Devices for Bioelectronics**

**Abstract**

Bioelectronics is an interdisciplinary field of materials science, electrical engineering, and biotechnology for the application of diagnosis and therapies in the healthcare industry. Owing to dissimilarities between soft, and wet living biological tissues and rigid, dry electronic devices at the human-machine interface, the development of more compatible materials and devices is a daunting challenge. Iontronics is a subdiscipline field that uses ions and biomolecules as the signal carrier to transfer information with biological systems, enabling direct and precise manipulation of physiological processes. They have been reported to trigger cell polarization status in vitro, controlling epileptiform activity in brain slice models, affecting sensory function in vivo, suppressing pain sensation in awake animals, and even modulating plant physiology. The core of iontronic devices is ion conducting materials that allow ions and biomolecules to move, such as polymers and hydrogels. The ion conducting materials also have the benefits of alleviating the mechanical mismatch between biological tissues and devices due to the low Young's modulus. However, they haven't obtained enough attention, and systematic study is absent.

This work showed representative examples of ion conducting materials, including biomaterials, single-crystal polymers, and nanotubes, and their ionic conductivity characterization using two major methods. Moreover, a systematic study on

polyelectrolyte hydrogel is presented with a novel method. The delivery of a large biomolecule, acetylcholine, is demonstrated with the optimized polyelectrolyte hydrogel. Additionally, I explored the design, fabrication, and implementation of bioelectronic devices that can deliver anions and even multiple ions with a single device. These results contribute to the iontronics field by broadening the knowledge of ion conducting materials and inspiring new device design for more complicated biological processes.



## Acknowledgement

I would like to express my deepest gratitude to the people who have provided me with great help and support in pursuit of my doctoral degree.

First and foremost, I'm deeply grateful to my supervisor, Marco Rolandi. He always encouraged me in my research and taught me how to present my idea and work to different audience.

I would like to offer my special thanks to my committee, Dr. Holger Schmidt and Dr. Nobby Kobayashi, for their time and valuable suggestions.

Thanks for being both great colleagues and friends: Le Luo and Harika Dechiraju. Look forward to your graduation in the near future! You're the best.

Thanks to the Rolandi Group members whom I have worked closely with: Dr. John Selberg, Dr. Houpu Li, Dr. Xenofon Strakosas, Dr. Chunxiao Wu, Dr. Jinhwan Kim, Dr. Sanhita Ray, Sergio Cordero, Raymond Breault, Sushmita Joardar, Tiffany Nguyen, and all the other past and present members.

Thanks to all the amazing collaborators in DARPA projects, Dr. Mohammad Jafari, Dr. Pattawong Pansodtee, Dr. Juanita Mathews, and Dr. Aadhar Jain. We really went through a hard journey along the way, but I enjoyed the time working with you all.

I also want to express my sincere thanks to the excellent collaborators: Dr. Molly Phillips, Dr. Michael J Strauss, and Dr. Qing-Hui Guo.

Out of the academia work, I'm grateful for all my friends who made my life wonderful in Santa Cruz: Xueyan Wang, Binbin Gu, Xin Wang, Yu Cao, Peng Zhou, Bolun Wong, Chun Zhang, Ziye Han, Xiaoyi Chen, Eason Wen, for which there are

too many to mention. Thank you for keeping me accompanied, warm, and happy during this endeavor.

Last but not the least, I would like to thank my parents Zhi Jia, Shilin Zhu, and my brother, Bofan Jia, for their unwavering support and belief in me over the years.

Without them none of this would be possible.

Publications in this dissertation

- [1] **M. Jia**, & M. Rolandi. Soft and Ion-Conducting Materials in Bioelectronics: From Conducting Polymers to Hydrogels. **Advanced healthcare materials** 9.5 (2020): 1901372.
- [2] **M. Jia**, J. Kim, T. Nguyen, T. Duong, & Rolandi, M. (2021). Natural biopolymers as proton conductors in bioelectronics. **Biopolymers**, e23433.
- [3] **M. Jia**, S. Ray, R. Breault, M. Rolandi. Control of pH in Bioelectronics and Applications. **APL Materials** 8.12 (2020): 120704.
- [4] **M. Jia**, H. Dechiraju, P. Pansodtee, J. Mathews, C. Wu, M. Levin, M. Teodorescu, M. Rolandi. Bioelectronic Control of Chloride Ions and Concentration with Ag/AgCl Contacts. **APL Materials** 8.9 (2020): 091106.
- [5] **M. Jia**, L. Luo, M. Rolandi. Correlating Ionic Conductivity and Microstructure in Polyelectrolyte Hydrogels for Bioelectronic Devices. (Submitted)
- [6] **M. Jia**, ..., M. Rolandi. An Multi Ion Electrophoretic Pump for Simultaneous on Chip Delivery of H<sup>+</sup>, K<sup>+</sup>, and Cl<sup>-</sup>. (Submitted)
- [7] J. Selberg, **M. Jia**, & M. Rolandi. Proton conductivity of glycosaminoglycans. **PLoS One** 14.3 (2019): e0202713.
- [8] M. Phillips, M., Wheeler, A. C., Robinson, M. J., Leppert, V., **M. Jia**, M. Rolandi, M., ... & Amemiya, C. T. (2021). Colloidal structure and proton conductivity of the gel within the electrosensory organs of cartilaginous fishes. **IScience**, 24(9), 102947.
- [9] Q. H. Guo, **M. Jia**, Z. Liu, Y. Qiu, H. Chen, D. Shen, ... & Li, P. Single-Crystal Polycationic Polymers Obtained by Single-Crystal-to-Single-Crystal Photopolymerization. **Journal of the American Chemical Society** 142.13 (2020): 6180-6187.

[10] J. M. Strauss, **M. Jia**, ... & M. Rolandi, Dichtel, W. R. (2021). Diverse Proton-Conducting Nanotubes via a Tandem Macrocyclization and Assembly Strategy. **Journal of the American Chemical Society**.

[11] H. Dechiraju, **M. Jia**, L. Luo, M. Rolandi. Ion-Conducting Hydrogels and Their Applications in Bioelectronics. *Advanced Sustainable Systems*. **Advanced Sustainable Systems** (2021): 2100173.

Publications not in this dissertation:

[12] J. Selberg, M. Jafari, J. Mathews, **M. Jia**, P. Pansodtee., H. Dechiruji, C. Wu, S. Cordero, ... & M. Rolandi. Machine Learning Driven Bioelectronics for Closed Loop Control of Cells. **Advanced Intelligent Systems** 2.12 (2020): 2000140. (Featured in **Advanced Science News**)

[13] A. R. Foley, T. S. Finn, T. Kung, A. Hatami, H. W. Lee, **M. Jia**, ... & J. A. Raskatov. Trapping and Characterization of Nontoxic A $\beta$ 42 Aggregation Intermediates. **ACS chemical neuroscience** 10.8 (2019): 3880-3887.

[14] M. Jafari, G. Marquez, J. Selberg, **M. Jia**, H. Dechiraju, P. Pansodtee, ... & Gomez, M. Feedback Control of Bioelectronic Devices Using Machine Learning. **IEEE Control Systems Letters** 5.4 (2020): 1133-1138.

[15] C. Wu, J. Selberg, B. Nguyen, P. Pansodtee, **M. Jia**, H. Dechiraju, ... & M. Rolandi. A Microfluidic Ion Sensor Array. **Small** 16.6 (2020): 1906436.

[16] P. Pansodtee, J. Selberg, **M. Jia**, M. Jafari, H. Dechiraju, T. Thomsen, ... & M. Teodorescu. The multi-channel potentiostat: Development and Evaluation of a Scalable Mini-Potentiostat array for investigating electrochemical reaction mechanisms. arXiv preprint arXiv:2105.09810 (2021).

[17] B. Jafari, K. Zlobina, G. Marquez, M. Jafari, J. Selberg, **M. Jia**, M. Rolandi and M. Gomez. A feedback control architecture for bioelectronic devices with applications to wound healing. **Journal of the Royal Society Interface** 18.185 (2021): 20210497.

# INTRODUCTION

## 1. Bioelectronics

Bioelectronics merges electronic devices and biological systems by sensing and controlling biological processes.<sup>1-3</sup> The experiments from Galvani in the 1780s can be considered as the birth of bioelectronics. Galvani showed that connecting frog legs with metal electrodes resulted in the contraction of the muscles.<sup>4</sup> These early experiments inspired many more aimed at understanding the role of electricity in biological processes. Since the discovery of the action potential in 1843,<sup>5</sup> electrical stimulation has developed into a therapy with devices. Examples of bioelectronics include cardiac pacemakers and brain implants to manage arrhythmia, epilepsy, and Parkinson's; devices to stimulating the vagus nerve for the treatment of inflammation; and cochlear implants to restore auditory functions.<sup>6, 7</sup> Clinical applications of neuronal and cardiac stimulation have alleviated the pain of millions of people suffering from epilepsy, Alzheimer disease and other dementia, Parkinson's disease, depression, and many other diseases from aberrant neural behavior, as well as cerebrovascular diseases and infections.<sup>8</sup> Compared to traditional pharmaceutical methods, bioelectronics devices are able to provide personalized therapeutic treatment and localized intervention.<sup>9, 10</sup>

Bioelectronics bridges electronic devices and biological systems to monitor and control biological processes.<sup>2</sup> The bioelectronic devices have made remarkable advances with room for improvement in long-term stability due to the mechanical

mismatch between rigid electronics and soft tissues and the non-specificity of electrical stimuli with respect to the many ions and small molecules that carry information in our bodies.<sup>11</sup> The mechanical mismatch between tissue and bioelectronics devices is a widely discuss topic.<sup>12</sup> The Young's moduli of the two are mismatched by several orders of magnitude and result in severe foreign body reaction and tissue damage (Figure 1).<sup>13</sup> In addition, electricity in biological systems is carried mostly by ions not electrons. These ions have much higher conductivity in water-rich biological environment compared to electrons and holes. To this end, much research has emerged in soft and ion-conducting materials to mitigate the mismatch in mechanical properties and the need for electron to ion conversion at the bioelectronic interface, including conducting polymers, carbon-based nanomaterials, as well as ion-conducting polymers and hydrogels.<sup>14 15, 16</sup>

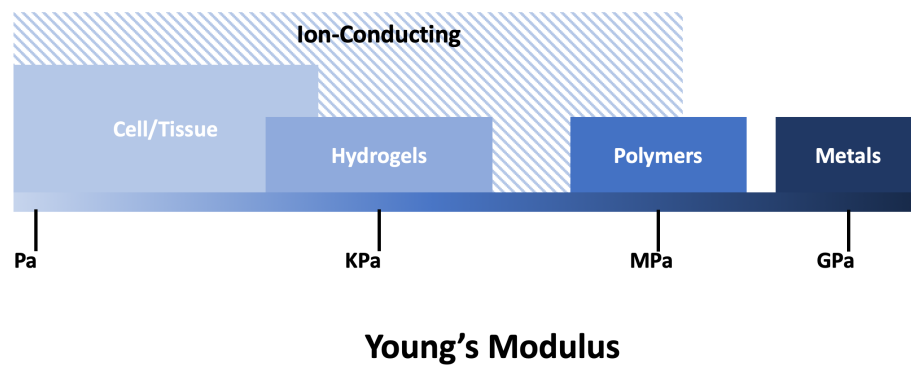


*Figure 1 Comparison of Young's moduli and ion conductivity of cell/tissue and materials commonly used at the bioelectronics interface. Metals are much stiffer than*

*cells and tissue; polymers are relatively softer and can be ion-conducting, which is a critical property for electron-to-ion signal conversion at the interface; hydrogels have similar Young's modulus as cells and tissue and are ion conductors.*

Iontronic devices generate, store, and transmit signals via the concentration, depletion, flow, as well as spatial and temporal distribution of ions.<sup>17</sup> These iontronic circuits behave analogous to traditional electronics, and allow for the development of fully chemical systems generating complex signal patterns at high spatiotemporal resolution and biochemical specificity. Examples include organic electrochemical transistors (OECTs),<sup>18</sup> organic field-effect transistors (OFETs),<sup>19</sup> organic electronic ion pump (OEIPs),<sup>20</sup> ionic diodes,<sup>21</sup> bipolar membrane junctions.<sup>22</sup> Cations and anions are similar to electrons and holes in conventional electrical devices, and need to be independently handled in iontronic devices. For this purpose, the most widely employed ionic conducting materials are polyelectrolyte that either selectively permeable to cations or anions.<sup>23</sup>



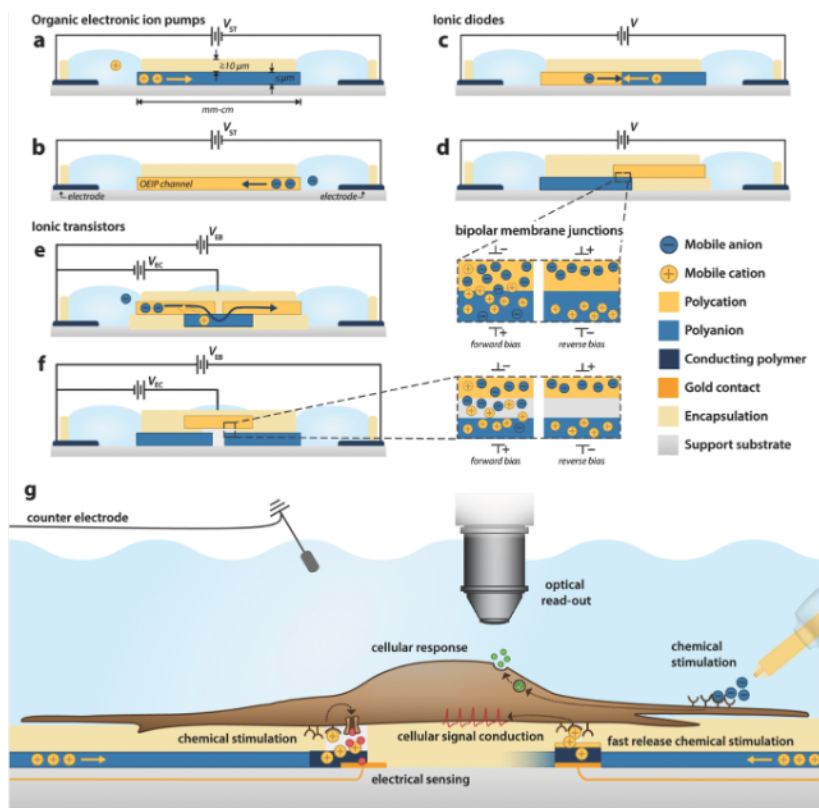


Figure 2 Iontronic components and applications. The basic OEIP structure for a) selective cation transport and b) selective anion transport. Ionic bipolar membrane diodes with c) lateral junction and d) stacked junction; zoom shows accumulation and depletion of the BM junction in forward and reverse bias. e) npn-IBJT in forward bias. f) pnp-IBJT with a neutral junction; zoom shows accumulation and depletion of the neutral junction in forward and reverse bias. g) Collection of iontronic components in applied systems, including from left to right the bioelectronic neural pixel,<sup>36</sup> fast vertical release devices, and freestanding OEIPs. Varying chemical stimulation gives varying cellular response that can be monitored externally or internally by, for example, optical read-out or electrical sensing.<sup>24</sup>

Among these iontronic devices, OEIPs are designed to deliver charged ions and biomolecules with high spatiotemporal resolution and dosage precision (one electron per delivered monovalent ion).<sup>25</sup> OEIP is an ionic resistor that connects the reservoir and target electrolytes. By applying an external electrical field, charged species are driven from the reservoir to the target through the ionic resistor. In recent years, OEIPs have been reported to deliver H<sup>+</sup>, K<sup>+</sup>, Ca<sup>++</sup>, GABA, which enabled triggering cell polarization status *in vitro*,<sup>25</sup> controlling epileptiform activity in brain slice models,<sup>26</sup> affecting sensory function *in vivo*,<sup>27</sup> suppressing pain sensation in awake animals,<sup>28</sup> and even modulating plant physiology.<sup>29</sup>

The traditional iontronic device are made of polymer-based ion-exchange membranes, such as over-oxidized PEDOT:PSS. More recently, polyelectrolyte hydrogels based iontronic devices have shown lots of advantages operating in aqueous media, such as better mechanical compatibility with tissues, biocompatibility, biodegradability, and permeability to larger biomolecules such as neurotransmitters. Hydrogels have been reported to be used in ionic diodes,<sup>30</sup> field effect transistors (FETs),<sup>31</sup> and ion pumps. For example, Seitanidou et.al designed an organic electronic ion pump (OEIP) based on glass capillary fibers filled with an ion exchange gel in the capillary “ion channel”.<sup>20</sup> A polycation, poly[2-(acryloyloxy) ethyl] trimethylammonium chloride (poly-AETMAC) was cross-linked with polyethylene glycol to create the gel used in the capillary. The OEIP was used to deliver acetylsalicylic acid and salicylic acid. Being able to pattern hydrogels within a capillary created easily implantable devices that could perform localized delivery at the target precisely. The same group also

developed capillary fiber OEIPs with an AMPSA (2-acrylamido-2-methylpropane sulfonic acid)-PEGDA (polyethylene glycol diacrylate) based hydrogel that were able to deliver protons, potassium ions and acetylcholine.<sup>32</sup>

## 2. Materials in bioelectronic devices

### 2.1 Metals and metal nanoparticles

Metal electrodes are the most commonly used in medical devices.<sup>33</sup> Platinum,<sup>34</sup> gold,<sup>35</sup> iridium,<sup>36</sup> and platinum-iridium<sup>37</sup> serve as microelectrodes in deep brain stimulation, cochlear implants,<sup>38</sup> and retinal implants.<sup>39, 40</sup> These noble metals are electrochemically stable, corrosion resistant, and have low reactivity in the complex biological environment.<sup>41</sup> With the miniaturization of bioelectronic devices, precise stimulation down to the single neuron level can be achieved with smaller microelectrodes.<sup>42</sup> Smaller metal electrodes require higher voltage to provide the same amount of current and stimulation due to increased impedance and decreased capacitance.<sup>11 43</sup> The electrolyte environment that surrounds cells and tissue is very sensitive to voltage and damage to both the tissue and the electrode may occur above a safe voltage threshold. This damage includes local heat, pH change, electrode degradation, and the generation of highly reactive chemical species.<sup>44</sup> To lower the impedance and reduce stimulation voltage, porous metal nanomaterials are used to modify the metal substrate.<sup>45</sup> Pt nanoparticles coated microelectrode arrays increase the active surface area and lower the impedance of the interface by up to two order of magnitudes.<sup>46, 47</sup> Ideally, desirable coating materials should have: 1) low impedance and effective charge injection, 2) electrochemical stability in physiological electrolyte, 3) good biocompatibility, 4) low Young's modulus matching cells/tissue, 5) compatibility with microfabrication.<sup>44</sup>

## 2.2 Conducting polymers and carbon materials

Hybrid materials that conduct both ions and electrons can create a seamless interface between bioelectronic devices and biological systems.<sup>48, 49</sup> This interface involves more efficient ion-to-electron conversion with low impedance<sup>50, 51</sup> in applications such as drug delivery,<sup>48, 52</sup> tissue regeneration,<sup>53</sup> and neural recording and stimulation.<sup>54, 55</sup>

Conducting polymers<sup>56, 57</sup> and carbon materials<sup>58, 59</sup> are commonly used as surface coatings for metal electrodes. PEDOT:PSS, polypyrrole (PPy), polyaniline (PANi), polythiophene and their derivatives have high conductivity, low cost, and good biocompatibility with cells.<sup>60-62</sup> Similar to metal nanoparticles, conducting polymers are deposited on metal electrodes with electrochemical polymerization that results in a rough nanoscale surface topology. This topology has lower impedance and a high surface area more conducive for cell attachment.<sup>63-65</sup> Many excellent reviews with additional examples exist on this topic.<sup>42, 66 67</sup>

Carbon materials, especially Carbon Nanotubes (CNTs) and graphene, are another type of popular surface coating because of their unique properties such as large aspect ratio and excellent chemical and mechanical stability.<sup>68-70</sup> The combination of CNTs and graphene with conducting polymers<sup>71, 72</sup> leads hybrid materials with an improved bioelectronic interface.<sup>73, 74</sup> For example, conducting polymers, like PEDOT, PPy, suffer from defects, delamination, and cracks during long-term stimulation.<sup>75</sup> Co-deposited PPy/SWCNT coated electrodes have significantly better mechanical stability.<sup>76</sup> In addition to the conductivity and stability of the electrodes, the adhesion

and close contact between cells and electrodes are also a critical prerequisite for good communication between bioelectronics devices and tissue.<sup>77</sup> To this end, bioactive materials, such as proteins and peptides, are mixed with the conducting materials to present to the cells a surface that induces adhesion and promotes proliferation.<sup>78, 79</sup>

### 2.3 Proton/Ion Conducting Materials

Ions and biomolecules are the languages that biological systems use to transfer signals in intracellular communication and organism function. As such, bioelectronic devices that conduct ions and biomolecules rather than electrons and holes are particularly suited for biological integration. In this scenario, ion conducting materials are one of the most critical part.

#### Hydrogels:

Hydrogels are physically or chemically crosslinked natural or synthesized 3D polymeric networks, which have the capacity to absorb a large amount of water (up to thousands of times more than their dry weight).<sup>80-82</sup> Hydrogels are intrinsically ion-conducting due to high water content that provides a good environment for ions to be mobile, which matches the signal carriers in biological systems.<sup>83-85</sup> Water rich property also imparts hydrogels low, tissue-like Young's modulus and results in a conformal interface with soft biological tissue.<sup>86, 87</sup> The unique combination of ionic conductivity, soft, elastic nature and optical transparency allows ion conducting hydrogels to be widely used in developing bioelectronics. In the 1960s, polyhydroxyethylmethacrylate (pHEMA) hydrogel was developed as a material for

permanent contact with human tissue and it was first used in contact lenses.<sup>88</sup> In the past decades, hydrogels have been successfully used in many biological applications such as extracellular matrix (ECM) for cell proliferation, tissue regeneration, artificial skin, and wound dressings.<sup>89, 90</sup> Recently, an increasing amount of research has focused on using hydrogels as the interface between electronics devices and physiological electrolytes because of the intrinsic ionic conductivity.<sup>91, 92</sup> Moreover, self-healing and self-adhesive hydrogels are ideal candidates for skin-attached electronics.<sup>93-96</sup>

Over the past decade, hydrogels made from natural biomaterials have come to the limelight because of their biocompatibility, hydrophilicity, and biodegradable nature.<sup>97</sup> Natural biomaterials are naturally derived materials, including polynucleotides, polypeptides, and polysaccharides (hyaluronic acid, alginate, chitosan, and cellulose).<sup>98, 99</sup> They are biocompatible, biodegradable and environmentally friendly, naturally abundant, sustainable, and have multiple reactive sites for chemical modification.<sup>100</sup> They can mimic the chemical and physical environments of an extracellular matrix thereby making them popular candidates for creating scaffolds for drug delivery and tissue engineering applications.<sup>99, 101</sup>

Although the majority of hydrogels are able to conduct ions because of their aqueous environment, here we mainly discuss the hydrogels that have fixed charges in the polymer network, polyelectrolyte hydrogels, because they have relatively high and selective ionic conductivity because of the mobile counterions. The ionic conductivity of polyelectrolyte hydrogels is affected by several parameters, such as water content,

charge carrier density and porosity. Water content depends on the ability of the hydrogel to absorb water, also defined as water uptake or swelling ratio and it plays an important role in affecting ionic conductivity.<sup>102</sup> With an increase in water content, the activation barrier for the ion transport is lowered and ionic dynamics are sped up.<sup>103</sup> Hydrogels with higher water content have higher ionic conductivity. More discussion about charge carrier density and porosity is shown in the next section after we introduce the ion transport mechanism.

This section is reproduced from<sup>51</sup>.



### 3. Ion Transport Mechanism

The history of ionic conductors can be traced back to the 1830s with the work of Michael Faraday on solid electrolytes.<sup>104</sup> The discovery of silver iodide and sodium alumina in 1967 is considered the beginning of the solid-state ionic field.<sup>105, 106</sup> Around the same time, Dupont synthesized a polymer ionomer known as Nafion, which is one of the best proton conductors.<sup>107</sup> Charge carriers in ionic conductors are negatively charged (anions) or positively charged (cations). There can be multiple ionic species with different charges, so the total conductivity of an ionic conductor is given by the sum of the contributions of all of charge carriers ( $\sigma = \sum_i Z_i e n_i u_i$  Equation 1):<sup>108</sup>

$$\sigma = \sum_i Z_i e n_i u_i \text{ Equation 1}$$

$\sigma$  is the sum of the ionic conductivity contributed by each mobile ion (i), where  $Z_i$  is the absolute value of the ion charge,  $e$  is the fundamental charge,  $n_i$  is the charge carrier density, and  $\mu_i$  is the mobility for each ion.

The ionic conductivity of a hydrogel is dependent on both the property of the ionic conductor, such as the charge carrier density, and the property of the charged species, such as their mobility. Charge carrier density can be defined as the total number of fixed charges per unit volume of the network.<sup>109, 110</sup> The assumption is that a hydrogel will be charge neutral so a fixed charge in the polymer backbone will result in the

same amount of mobile charge that can contribute to the ionic conductivity. The mobility ( $\mu$ ) of different ions is dependent on the temperature of the system (T), the diffusion coefficient (D), charge of the ion (q), and the Boltzmann constant ( $K_B$ ) as shown in  $\mu = \frac{Dq}{k_B T}$  Equation 2.

$$\mu = \frac{Dq}{k_B T} \text{ Equation 2}$$

$$\sigma = n \frac{Dq}{k_B T} \text{ Equation 3}$$

In a porous network, the diffusion coefficient of ions is smaller than the diffusion coefficient for the same ion in water and needs to be adjusted for the size and topography of the pores as shown in  $D_{eff} = D_0 \frac{\epsilon}{\tau}$  Equation 4: <sup>111, 112</sup>

$$D_{eff} = D_0 \frac{\epsilon}{\tau} \text{ Equation 4}$$

where  $D_{eff}$  is effective diffusion coefficient in a porous network,  $D_0$  is the diffusion coefficient in liquid,  $\epsilon$  is the porosity, and  $\tau$  is the tortuosity, which describes the non-linear path from one side of the membrane to the other.<sup>113</sup> Tuning charge carrier density, porosity, and tortuosity during hydrogel synthesis can optimize the ionic conductivity of the hydrogel.

Different from other ions, protons can follow a version of the mass diffusion, called the vehicle mechanism.<sup>114</sup> In the vehicle mechanism,  $H^+$  diffuse in the form of hydrated proton aggregates, such as the hydronium ion ( $H_3O^+$ ), the Zundel ion ( $H_5O_2^+$ ), and the Eigen ion ( $H_9O_4^+$ ), which move through aqueous channels as a single entity.<sup>114, 115</sup> In hydrogen bonded systems, such as water,  $H^+$  follow the Grotthuss mechanism, which results in higher mobility.<sup>116</sup> In the Grotthuss mechanism,  $H^+$  move faster because they quickly transfer along a network of hydrogen bonds- a proton wire<sup>117</sup>- via tunneling or hopping (Figure 3).<sup>116</sup> The translocation of a proton along the proton wire creates a Bjerrum D orientation defect in the water chain, which needs to rotate itself to accept another proton.<sup>118, 119</sup> Thus the dynamics in the Grotthuss mechanism are often referred to as “hop and turn”. Similarly to the transfer of  $H^+$ , hydroxyl ions ( $OH^-$ ) can also transfer along a proton wire in the form of proton holes.<sup>120</sup>

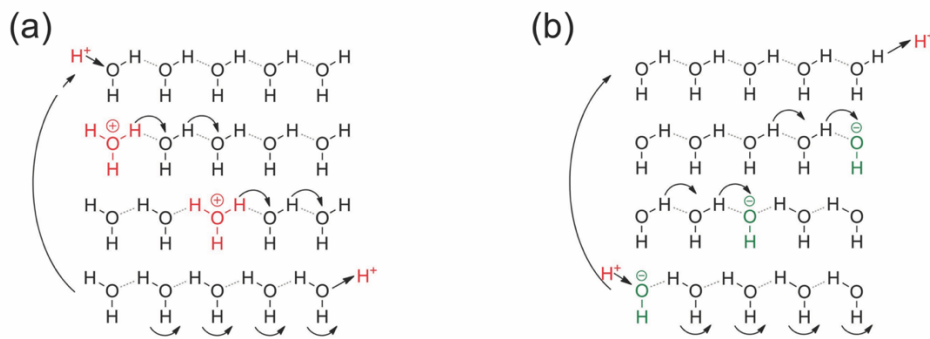


Figure 3 (A) Grotthuss mechanism for the conduction of  $H^+$  as hydronium ion along proton wires. (B) An equivalent mechanism for  $OH^-$  conductivity as proton hole along proton wire.

In this scenario, proton conduction can be qualitatively described using the same description used for electrons and holes “hopping” in amorphous in semiconductors with  $H^+$  are distributed between a “valence band” and a “conduction band” (Figure 4). Even when a proton is in the “conduction band”, it still needs to overcome a structure dependent potential barrier, which is typically comparable to the energy required to break a hydrogen bond (approximately 0.1 eV) in the second solvation shell.<sup>120-122</sup> Similarly to semiconductor, an intrinsic proton wire does not conduct until a  $H^+$  and  $OH^-$  pair is created. The energy required to create  $H^+$  and  $OH^-$  pair in the proton wire is derived from the Gibbs Helmholtz equation and the dissociation constant of water ( $K_w$ ) as:

$$E_{gap} = \Delta G^{0'} = -k_B T \ln K_w = 0.83 \text{ eV} \text{ Equation 5}$$

This value is similar to the activation energy measured in proton conducting biopolymers.<sup>123</sup> To increase the conductivity of a proton wire,  $H^+$  and  $OH^-$  dopants can be added with acidic and basic functionalities in the hydrogen bond network. In this case, we can substitute  $K_w$  with  $K_a$  (acid dissociation constant) or  $K_b$  (base dissociation constant) to in Equation 5 to find the activation energy (Figure 4).<sup>124, 125</sup>

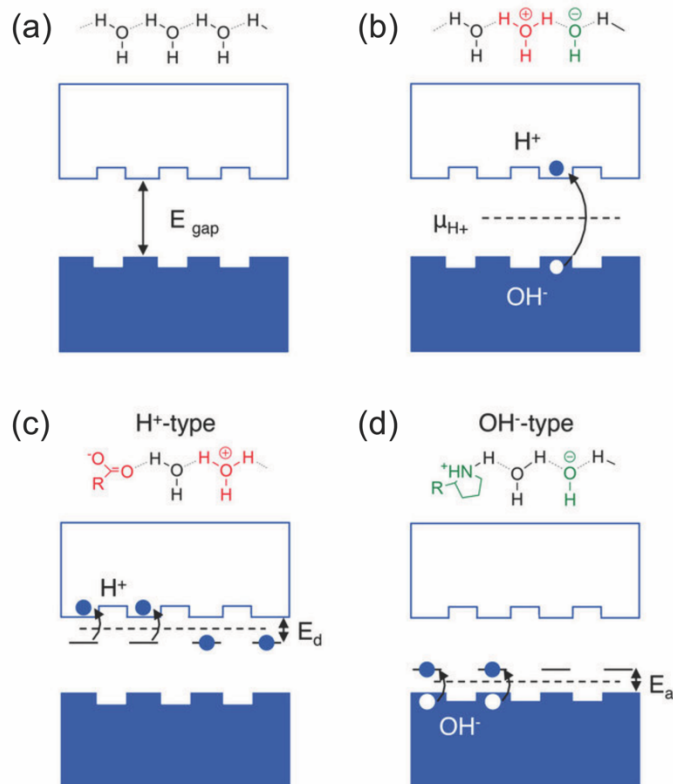
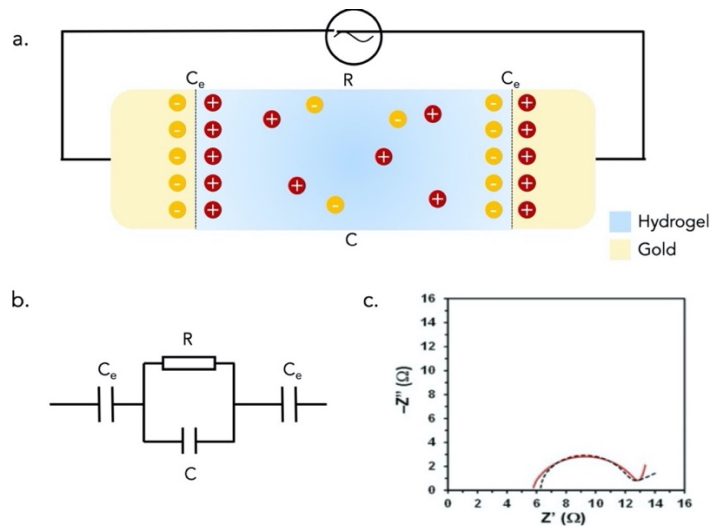


Figure 4 Energy diagram representation of conduction in hydrogen bonded proton wire. (a) A wire with no  $\text{H}^+$  or  $\text{OH}^-$  defect does not conduct. (b) For an intrinsic proton wire, the protochemical potential  $\mu_{\text{H}^+}$  is in the middle of the bandgap. (c) An acid donates a  $\text{H}^+$  into the conduction band of a proton wire to yield a  $\text{H}^+$ -type protonic conductor. (d) A base accepts a  $\text{H}^+$  to create a  $\text{OH}^-$  (proton hole) in the valence band of a proton wire to yield a  $\text{OH}^-$ -type protonic conductor.<sup>320</sup>, with permission from Nature.

The ionic conductivity is important for bioelectronic devices that manipulate ions directly, so the measurement is of great significance.

Electrochemical impedance spectroscopy is a popular technique to measure the ionic conductivity by analyzing the electrical behavior of a material sandwiched between two electrodes under applying an alternating electrical signal.<sup>110, 126</sup> When this electrical signal is applied to the sample, periodically the negative and positive ions accumulate at the respective electrodes forming a double layer (Figure 5a). Using impedance spectroscopy, an equivalent circuit can be generated where  $C_e$  represents the capacitance of the electrical double layers,  $C$  is the capacitance formed by the electrodes and the electrolyte and  $R$  represents the resistance of the bulk electrolyte (Figure 5b). Figure 5c is a representation of one such result where they found that the measured Nyquist plot was a semicircle, where the x-intercept of the curve gives the electrolyte resistance and the diameter of the semicircle corresponds to the charge transfer resistance at the electrode-electrolyte interface.<sup>127</sup>



*Figure 5 (a) Schematic showing setup for impedance spectroscopy on a hydrogel. The gel is sandwiched in between two electrodes and upon applying an electrical signal, electrical double layers are formed at both the electrodes. (b) Equivalent circuit for the setup described in (a) where  $C_e$  represents the capacitance of the electrical double layers,  $C$  represents the capacitance formed by the electrodes and  $R$  shows the resistance of the bulk electrolyte, (c) Real and imaginary parts of the impedance calculated using impedance spectroscopy.*

For protons, there is another method that can measure the conductivity. Most metals are excellent contacts for  $e^-$  but poor for  $H^+$ , so most investigations on proton conduction use alternating current to avoid ion accumulation at the interface. The couple Pd/PdH<sub>x</sub> can act as a  $H^+$  to electron transducer and have been used in artificial membranes containing ion channels, biohybrid photodetectors, the delivery of biochemical stimuli, pH sensitive glucose sensing,<sup>128</sup> and precise control of pH using machine learning.<sup>25</sup> Pd/PdH<sub>x</sub> is also a proton-transparent contact for DC measurements of proton conducting materials.<sup>129, 130</sup> Pd has a strong affinity to hydrogen and forms palladium hydride (PdH<sub>x</sub>) either by absorbing hydrogen from H<sub>2</sub> gas or from  $H^+$  in solution as a reversible hydrogen electrode in electrochemistry.

The incorporation of  $H^+$  from solution into Pd is potential dependent and follows the reversible reduction,  $H^+ + e^- \leftrightarrow H$ , at the Pd/PdH<sub>x</sub> - solution interface and the subsequent physisorption of H onto Pd to form PdH<sub>x</sub>.<sup>131</sup> An electrical potential

applied (V) on the Pd/PdH<sub>x</sub> contact shifts the reaction equilibrium and induces the transfer of H<sup>+</sup> to or from the solution, which effectively controls [H<sup>+</sup>] in the solution (Figure 6). In brief, when V < 0 and the contact is at a lower potential than the solution, an H<sup>+</sup> in solution is adsorbed to the Pd/solution interface where it is reduced to PdH<sub>ads</sub> by an incoming e<sup>-</sup>. The PdH<sub>ads</sub> subsequently absorbs into the Pd subsurface to form PdH<sub>subs</sub> and finally diffuses into the bulk Pd to form PdH<sub>bulk</sub> following the concentration gradient.<sup>132</sup> The net result is the removal of an H<sup>+</sup> from the solution for every e<sup>-</sup> provided by the leads. This in turn lowers [H<sup>+</sup>] and increases pH. When V > 0, some of the H that is part of PdH<sub>ads</sub> oxidizes at the Pd surface to form H<sup>+</sup> and dissolves into solution with the e<sup>-</sup> going into the electronic leads. The additional H<sup>+</sup> in solution increases [H<sup>+</sup>] and consequently decreases pH.

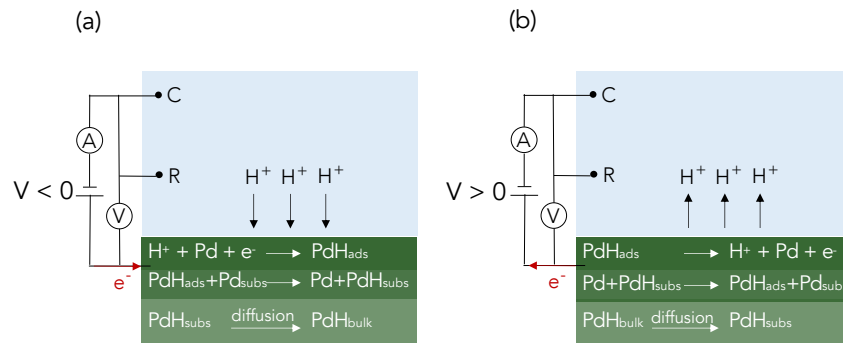


Figure 6 (a) Given a negative potential, H<sup>+</sup> is first adsorbed onto the surface of Pd (Pd<sub>ads</sub>), then absorbed into the subsurface layer, Pd<sub>subs</sub>, and further diffuses into bulk Pd to form PdH<sub>bulk</sub>. (b) Given a positive potential, H<sup>+</sup> is first released from the



surface,  $PdH_{ads}$ , then from the subsurface layer ( $Pd_{subs}$ ) to the surface ( $Pd_{ads}$ ) and further diffuses from  $PdH_{bulk}$ .

A more quantitative way to describe the  $H^+$  transfer across the interface uses the protochemical potential ( $\mu$ ) because  $H^+$  transfer does not only follow  $V$ , but is also affected by pH of the solution.<sup>133</sup> We can define the difference in protochemical potential between  $PdH_x$  ( $\mu_{PdH_x}$ ) and the solution ( $\mu_{pH}$ ) using Equation 6.

$$\mu_{PdH} - \mu_{pH} = eV + k_B T \ln \frac{a_{H^+}}{(p_{H_2})^{1/2}} \quad \text{Equation 6}$$

where  $a_{H^+}$  = activity of  $H^+$  in solution with  $pH = -\log a_{H^+}$ ,  $p_{H_2}$  = hydrogen partial pressure in the Pd,  $V$  = potential difference between Pd and solution.

When  $\mu_{PdH} - \mu_{pH} = eV + k_B T \ln \frac{a_{H^+}}{(p_{H_2})^{1/2}}$  Equation 6 leads a positive value,  $H^+$  will transfer from the contact to the solution until equilibrium is reached. When it leads a negative value,  $H^+$  will transfer from the solution to the contact until equilibrium is reached. In general, for solutions with low pH (high  $[H^+]$ ) the transfer of  $H^+$  into the Pd will be favored vs transferring  $H^+$  from the contact into the solution. The opposite is true for solutions with high pH (low  $[H^+]$ ).

We'll show the examples of proton conductivity measurement using Pd/ $PdH_x$  contacts in the next section.

This section is reproduced from <sup>134</sup>.

## RESEARCH CONTRIBUTION

### 4. Measuring Proton Conductivity

#### 4.1 Proton conductivity of Glycosaminoglycans

Proton conductivity is important in many natural phenomena including oxidative phosphorylation in mitochondria and archaea, uncoupling membrane potentials by the antibiotic Gramicidin, and proton actuated bioluminescence in dinoflagellate. In all of these phenomena, the conduction of protons occurs along chains of hydrogen bonds between water and hydrophilic residues. These chains of hydrogen bonds are also present in many hydrated biopolymers and macromolecule including collagen, keratin, chitosan, and various proteins such as reflectin. All of these materials are also proton conductors.

Recently, our group has discovered that the jelly found in the Ampullae of Lorenzini-shark's electro-sensing organs- is the highest naturally occurring proton conducting substance. The jelly has a complex composition, but we proposed that the conductivity is due to the glycosaminoglycan keratan sulfate (KS). Here we measure the proton conductivity of hydrated keratan sulfate purified from Bovine Cornea. PdH<sub>x</sub> contacts at  $0.50 \pm 0.11 \text{ mS cm}^{-1}$ , which is consistent to that of Ampullae of Lorenzini jelly at  $2 \pm 1 \text{ mS cm}^{-1}$ . Proton conductivity, albeit with lower values, is also shared by other glycosaminoglycans with similar chemical structures including dermatan sulfate, chondroitin sulfate A, heparan sulfate, and hyaluronic acid. This

observation supports the relationship between proton conductivity and the chemical structure of biopolymers.

#### 4.1.1 Introduction

Proton ( $H^+$ ) conductivity is important in many natural phenomena<sup>134</sup> including oxidative phosphorylation in mitochondria and archaea,<sup>135, 136</sup> uncoupling membrane potentials by the antibiotic Gramicidin<sup>137</sup>, and proton actuated bioluminescence in dinoflagellate<sup>138</sup>. In all of these phenomena, the conduction of  $H^+$  occurs along chains of hydrogen bonds between water and hydrophilic residues. These chains are often referred to as proton wires.<sup>139</sup> This conduction follows the Grotthuss mechanism in which a hydrogen bond is exchanged with a covalent bond contributing to the effective transfer of an  $H^+$  from a molecule to its next-door neighbor<sup>140</sup>. Following this mechanism, proton conductivity in hydrated biopolymers and macromolecules is widespread including collagen<sup>141</sup>, keratin<sup>142</sup>, chitosan<sup>143</sup>, melanin<sup>144</sup>, peptides<sup>131</sup>, and various proteins such as bovine serum albumin<sup>145</sup> and reflectin<sup>146, 147</sup>. In addition to the ability to support proton wires, typically these materials include an acid or a base group that serve as  $H^+$  or  $OH^-$  dopants and provide charge carriers for proton conductivity<sup>148-150</sup>. Following this trend, for example, the synthetic polymer Nafion, with a high proton conductivity of  $78 \text{ mS cm}^{-1}$ , contains very strong acid groups that donate  $H^+$  to the water of hydration for proton conduction<sup>151</sup>.

Our group has recently demonstrated that the jelly contained in the ampullae of Lorenzini, the electrosensing organ of sharks and skates, is the highest naturally occurring proton conductor<sup>152</sup>. We proposed that keratan sulfate (KS), a

glycosaminoglycan (GAG), was the material responsible for proton conductivity due to its similar chemical structure to other known proton conductors such as chitosan, and the ability to form many hydrogen bonds with water when hydrated (Figure 7A)<sup>153, 154</sup>. Given that it is difficult to purify KS from the shark jelly due to small amounts of sample per organism, we set to explore KS from different sources that were available to perform these measurements. Here, we have measured the proton conductivity of KS derived from bovine cornea<sup>155, 156</sup> and other GAGs using Pd based proton conducting devices<sup>143</sup>.

GAGs are long, linear, hydrophilic biopolymers composed of repeating of disaccharide units with many acidic groups that may support the presence of proton wires (Figure 7B) that transport protons through the Grotthuss mechanism<sup>157</sup>. Among these are hyaluronic acid (HA), heparan sulfate (HS), chondroitin sulfate A (CSA), dermatan sulfate (DS), and KS<sup>158, 159</sup>. Additionally, GAGs have important biological functions in regulating hydration and water homeostasis of tissues, which is derived from their ability to absorb very large amounts of water at high humidity<sup>160</sup>. They are also implicated in many fundamental operations such as cell patterning<sup>161</sup>, cell signaling, and regulation<sup>162</sup>.

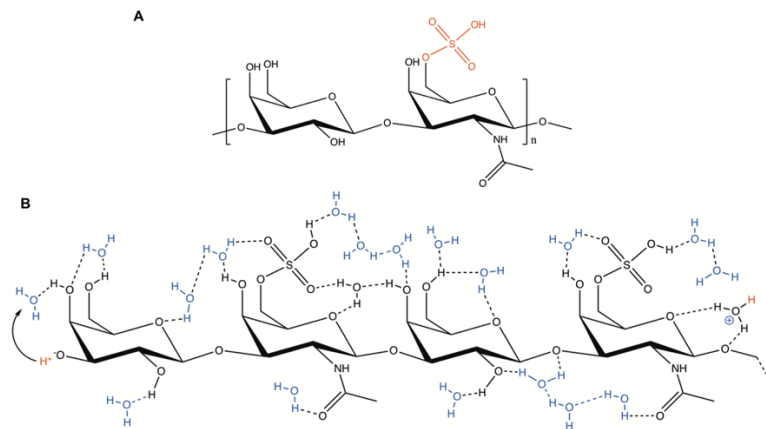


Figure 7 The keratan sulfate. (A) Chemical structure of KS. (B) An illustration of a three-monomer segment of KS. Possible intra- and inter-molecular hydrogen bonds as well as the hydrogen bonds between the water of hydration and the polar parts of the molecule form a continuous network comprised by hydrogen-bond chains. The sulfate group interacts with the hydrogen-bond network and forms an  $H_3O^+$  (hydronium) ion.

#### 4.1.2 Materials and Methods

**Materials.** Glycosaminoglycan samples were received from the Linhardt laboratory at Rensselaer University and stored dry at  $-15^{\circ}C$ . Including, 70% pure CSA isolated from bovine trachea (average MW: 20kDa), HA sodium salt from streptococcus zooepidemicus (average MW: 100kDa), DS from porcine intestinal mucosa (average MW: 30kDa), HS (porcine intestinal mucosa (average MW: 14.8kDa), and KS isolated from the bovine cornea (average MW: 14.3kDa) a biochemical description of the KS can be found at Weyers et al.<sup>156</sup>.

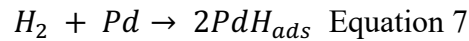
Device Fabrication. Two-terminal measurements were performed on Si substrates with a 0.1 $\mu\text{m}$  SiO<sub>2</sub> layer. Conventional photolithography was used to pattern 0.1 $\mu\text{m}$  thick Au and Pd contacts. Pd contacts were 500  $\mu\text{m}$  wide and separated by different channel lengths,  $L_{\text{SD}} = 5, 10, 20, 50, 100, 200, 500 \mu\text{m}$ . We performed both two terminal device measurements and transmission line measurements (TLM) to reduce the influence of contact resistance on the conductivity <sup>144</sup>.

Deposition of Glycosaminoglycans. All lyophilized samples were rehydrated in DI water (pH 6.7) at a concentration of 0.15 – 0.2 mg  $\mu\text{l}^{-1}$  and drop casted onto the devices. The samples were the dehydrated into a film with dry nitrogen gas flow.

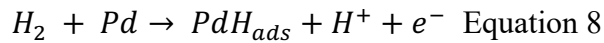
Proton Conductivity Measurements. Direct current–resistance measurements were performed using a Keithley 4200 source-meter and a two-contact probe station arrangement on devices. The devices were enclosed in an environmental chamber at room temperature in an atmosphere of nitrogen or hydrogen with controlled relative humidity (RH). We controlled RH by bubbling gases through a bubbler containing DI water at pH 6.7. Hydrated in sequence from dry to 75%RH in N<sub>2</sub>, 90%RH in N<sub>2</sub>, 90% RH in a mixture of 95% N<sub>2</sub> with 5% hydrogen, and 90% RH in a mixture of 95% N<sub>2</sub> with 5% deuterium gas to form PdH<sub>x</sub> or PdD<sub>x</sub> contacts. A one-hour incubation period was carried out after switching between humidity and gas compositions. During the measurement, the Pd/PdH<sub>x</sub> electrodes were contacted with tungsten probes. When we applied a source-drain potential difference,  $V_{\text{SD}}$ , the PdH<sub>x</sub> source injected protons (H<sup>+</sup>) into drain through the samples, inducing measurable electrical current in the circuit.

#### 4.1.3 Results and Discussion

Proton Conductivity Measurements. Palladium (Pd) devices are useful for studying proton transport in materials due to the nature of Pd to reversibly form palladium hydride ( $\text{PdH}_x$ )<sup>163-166</sup>. Several mechanisms for the formation of  $\text{PdH}_x$  are known (Equations 7-10).



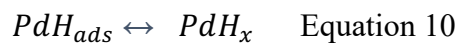
Equation 7 describes the adsorption and splitting of  $\text{H}_2$  molecules into two adsorbed H on the Pd metal surface without electron transfer in a reaction described by Tafel kinetics.



Equation 8 is the Heyrovsky reaction in which a  $\text{H}_2$  is split into an adsorbed H atom and a  $\text{H}^+$ ,  $e^-$  pair at the Pd surface, this  $e^-$  is transferred into the metal.



The Volmer reaction in Equation 9 describes a third mechanism, which involves an electron transfer to a  $\text{H}^+$  near the Pd surface allowing it to adsorb as  $\text{PdH}_{ads}$ . Once  $\text{PdH}_{ads}$  is formed on the metal surface, H can diffuse into the subsurface bulk forming  $\text{PdH}_x$  (eq. 4).<sup>133, 143, 167</sup>.



Pd devices were designed such that PdH<sub>x</sub> formation occurs spontaneously by Equation 7 in a 5% H<sub>2</sub> atmosphere on two Pd contacts. These Pd/PdH<sub>x</sub> contacts are separated by a channel consisting of a GAG film which completes the circuit (Figure 8). A voltage V<sub>SD</sub> between the Pd/PdH<sub>x</sub> contacts induces a current of H<sup>+</sup> to exit one Pd contact, travel through the film channel, and enter the second Pd contact according to Equation 10. In this manner, one e<sup>-</sup> travels through the circuit and is recorded as I<sub>d</sub> for each H<sup>+</sup> that is conducted through the channel. Considering the conductivity of the GAG films is expected to be much less than the conductivity of electrons in electrodes, the current that we measure during the experiments is indicative of the conductivity of the channel.

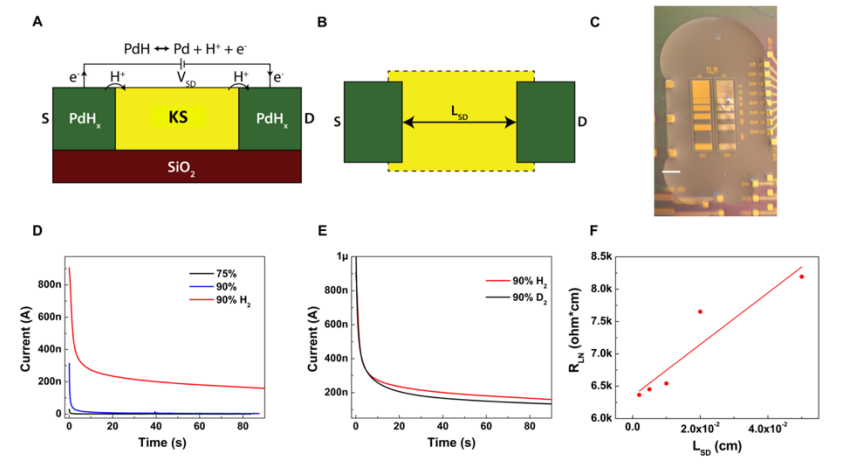


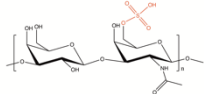
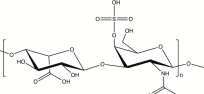
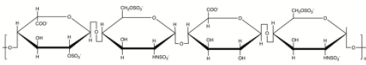
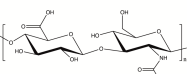
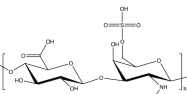
Figure 8 Proton conduction measurement of KS. A) Palladium hydride (PdH<sub>x</sub>) electrode behavior. Under a VSD, PdH<sub>x</sub> source split into Pd, H<sup>+</sup>, and e<sup>-</sup>. Protons are injected into the KS, whereas electrons travel through external circuitry and are



measured. B) TLM geometry. Varying the distance between source and drain (LSD) distinguishes between the fixed PdH<sub>x</sub> – KS interface contact resistance and the varying bulk resistance. C) Optical image of TLM geometry with hydrated KS on the surface. Scale bar, 500 μm. D) Transient response to a 1V bias in KS at 75%, 90%, 90% H<sub>2</sub> RH, in which the current under 90% with hydrogen is much higher than that under 90% RH without hydrogen. E) Deuterium current (black) at 90% D<sub>2</sub> humidity is lower than proton current (red). F) The normalized resistance RLN as a function of LSD, A linear fit gives a bulk material proton conductivity of  $0.50 \pm 0.11 \text{ mS cm}^{-1}$ .

After deposited directly onto the transmission line measurement (TLM) (Figure 8C) device surface without further processing, the KS film is thick, viscous, and optically transparent. After one hour of incubating at 50%RH, the KS film dries to a non-homogenous film. The film rehydrates fully after incubating at 90%RH for one hour and appears as wet as when it was drop-cast from solution (Figure 8C). This high-water content of KS films is a result of sulfate groups functionalizing either or both of the galactose and N-acetyl glucosamine sugars which make up the repeating disaccharide unit of the GAGs. Considering the other members of GAGs family, DS, HS, CSA, and HA also contain an abundance of repeating acidic groups which may stabilize proton wires, as shown in Table 1.

*Table 1 Glycosaminoglycan chemical structures, Pka and conductivity ( $\sigma$ ) estimated with TLM devices*

Materials	Chemical structure	Pka	$\sigma$ (mS cm <sup>-1</sup> )	$\sigma_{TLM}$ (mS cm <sup>-1</sup> )
<b>Keratan Sulfate</b>		2 <sup>168</sup>	0.015	0.50 ± 0.11
<b>Dermatan Sulfate</b>		1.9 <sup>169</sup>	0.030	-
<b>Heparan Sulfate</b>		-	0.012	-
<b>Hyaluronic Acid</b>		3.0 <sup>170</sup>	0.012	0.28 ± 0.06
<b>Chondroitin Sulfate A</b>		1.5 - 2 <sup>171</sup>	0.013	-

With  $V_{SD} = 1V$  on the Pd devices, we measured the drain current ( $I_D$ ) of KS, as shown in Figure 8D. First, at 75% RH in  $N_2$ ,  $I_D$  ( $\sim 0.5$  nA) is small (black in Figure 8D). With the RH increased to 90% in  $N_2$ , the increase in  $I_D$  was negligible (red in Figure 8D). However, after we changed the gas to 95% $N_2$  + 5% $H_2$ , the  $I_D$  increased more than 300 times to 155 nA (green in Figure 8D). The same measurements were performed with DS, HS, CSA, and HA family and followed similar trends (Figure 9). All GAGs displayed an increased current upon a 90%RH (5% $H_2$ ) atmosphere compared to a 90%RH  $N_2$  atmosphere, indicating that protons predominately contribute to the conductivity of GAGs materials at high relative humidity.

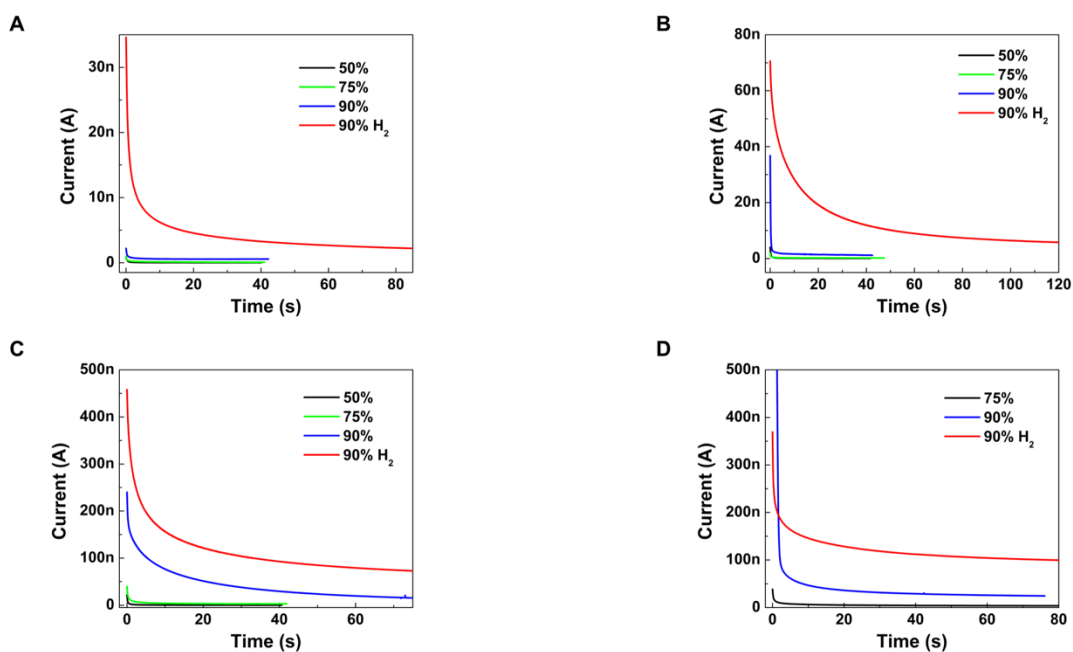


Figure 9 Current under different RH of GAGs family: (a) hyaluronic acid, (b) heparan sulfate, (c) chondroitin sulfate A and (d) dermatan sulfate. The current under 90%RH with hydrogen is much higher than 90%RH without hydrogen.

Kinetic isotope effect. To further test whether KS conductivity predominantly arises from protons, we investigated the kinetic isotope effect. Measurements were repeated while hydrating the sample with deuterium oxide ( $D_2O$ ) instead of water and exposing the sample to deuterium gas rather than  $H_2$ . Like protons, deuterium ions ( $D^+$ ) can transport along proton wires and hydrated materials, albeit with a lower mobility and an associated lower current due to the higher molecular weight and higher binding energy during H-bonding<sup>172</sup>. The kinetic isotope effect in KS is

evident as a drop in the conductivity when deuterium replaces hydrogen as the atom being transported (Figure 8E). Here, we observe a 15% drop in current when deuterium replaces hydrogen. The kinetic isotope effect observed with KS is relatively small. However, a similar small kinetic isotope effect was observed for the proton conduction of bovine serum albumin<sup>145</sup>. The other members in GAGs family display a larger kinetic isotope effect, the current drop is nearly 50% (Figure 10). The divergence of the KIE between the KS films and the other GAGs may be due to regions different transport regimes for H<sup>+</sup> in KS films. Where the binding energy plays a big role in H-bond mediated transport by the Grotthuss mechanism it will not be as noticeable by regions of bulk diffusion.

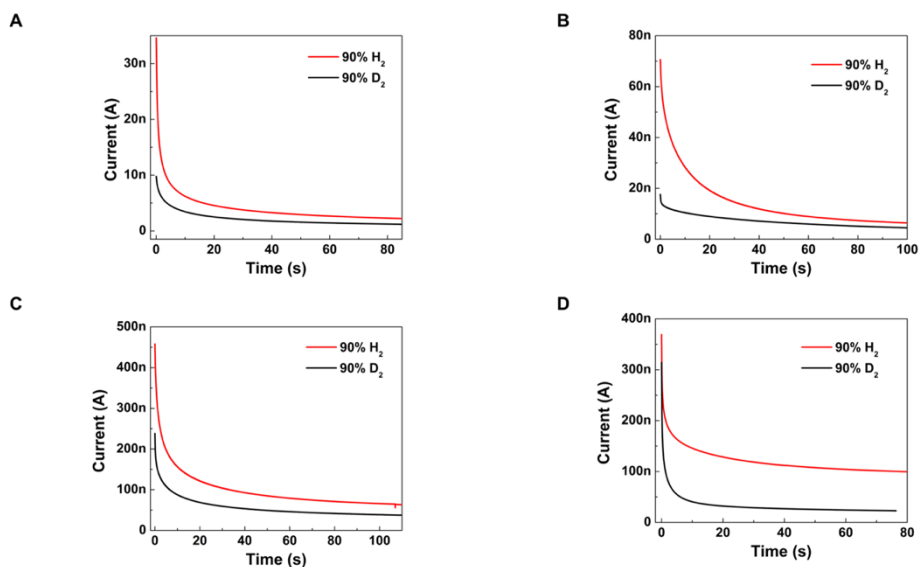


Figure 10 Kinetic isotope effect in members of GAGs family: (a) hyaluronic acid, (b) heparan sulfate, (c) chondroitin sulfate A and (d) dermatan sulfate. Current

*measured in a 5% deuterium (black) atmosphere at 90%RH vs a 5% proton atmosphere at 90%RH (red).*

TLM devices are designed with different lengths between the Pd source and the drain contacts to eliminate the effect of contact resistance in the measurements of the proton conductivity (Figure 8B)<sup>152</sup>. We applied  $V_{SD} = 1$  V on devices with  $L_{SD}$  ranging from 5 to 500  $\mu\text{m}$ , measured  $I_D$ , and calculated the resistance of each device,  $R_L$ . In this geometry,  $R_L$  increases linearly with  $L_{SD}$ , but the contact resistance,  $R_C$ , at the source–KS and drain–KS interface is constant. Considering that different devices contained KS with different thicknesses, we multiplied  $R_L$  by the sample thickness to get the normalized resistance,  $R_{LN}$ . The slope of the plot of  $R_{LN}$  as a function of  $L_{SD}$  is proportional to the resistivity of KS, and the intercept on the  $R_{LN}$  axis for  $L_{SD} = 0$  is  $R_{CN}$  (Figure 8F). Here, we obtain  $\sigma = 0.50 \pm 0.11$   $\text{mS cm}^{-1}$ , which is only one order of magnitude lower than the proton conductivity of Nafion  $\sigma = 58.3 \pm 2.5$   $\text{mS cm}^{-1}$ <sup>152</sup> measured in the same geometry (Figure 11). The proton conductivity of the Nafion control sample ( $58.3 \pm 2.5$   $\text{mS cm}^{-1}$ ) measured in a TLM geometry is extremely close to the reported value of 78  $\text{mS cm}^{-1}$ .<sup>151</sup> Therefore, we conclude that  $\sigma = 0.50 \pm 0.11$   $\text{mS cm}^{-1}$  measured in this way is a good indicator of the proton conductivity of KS. Table 1 shows the proton conductivity of Nafion and known biopolymers, and KS performs well among them.

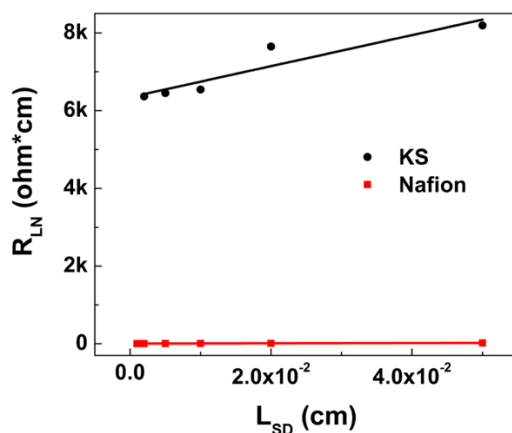


Figure 11 Control experiments on Nafion. Conductivity of Nafion measured with this TLM device is  $58.3 \pm 2.5 \text{ mS cm}^{-1}$ . It's slightly lower than the literature value of  $78 \text{ mS cm}^{-1}$ , which is attributed to sample preparation. The reported literature value is after immersion in heated sulfuric acid, while the sample here was simply drop-cast from solution.

Table 2 Room-temperature proton conductivities of Nafion and known biopolymers.

Materials	Conductivity ( $\text{mS cm}^{-1}$ )	Ref
Nafion	78	151
AoL jelly	$2 \pm 1$	152
Keratan Sulfate	$0.50 \pm 0.11$	This work
Maleic Chitosan	0.7	173
Reflectin	0.1	146
Bovine Serum Albumin	0.05	145

<b>Melanin</b>	0.02	144
----------------	------	-----

Out of the other GAG films measured and reported in Table 2. Hyularonic acid has the highest conductivity  $0.28 \pm 0.06 \text{ mS cm}^{-1}$ . However, some of the other GAGs materials, such as dermatan sulfate, did not form a homogeneous film and it was not possible to measure the conductivity using the TLM geometry. The conductivity reported with the two terminal geometry also contains contact resistance and therefore it is lower as expected. Within experimental error, we did not observe any variation in conductivity with variation in  $\text{pK}_a$  of the acidic groups. It is difficult to relate the concentration of  $\text{H}^+$  in these hydrated states because  $\text{pK}_a$  is determined in infinite dilution. We assume that we are hydrating the films with water at neutral pH, then we expect the vast majority of the sulfonate acidic groups on the GAGs to become ionized independent of their individual variation in  $\text{pK}_a$ .

#### 4.1.4 Conclusions

Inspired by the high conductivity in the jelly of the ampullae of Lorenzini, we measured the proton conductivity of KS and other glycosaminoglicans with similar chemical structures. Using TLM devices at room temperature, we measured the proton conductivities of  $0.50 \pm 0.11 \text{ mS cm}^{-1}$  at 90% RH (5% $\text{H}_2$ ) for KS, which is near to that of ampullae of Lorenzini jelly ( $2 \pm 1 \text{ mS cm}^{-1}$ ). This result supports the claim that KS is a factor in the high proton conductivity of the ampullae of Lorenzini jelly. We leave open the possibility that other materials in the ampullae of Lorenzini

jelly and organization of the KS chains may play additional roles well. We have also measured the proton conductivity of other GAGs including HS, DS, CSA and HA. Their conductivity is lower, but comparable with KS suggesting that proton conductivity is a common property of GAGs with acidic groups upon hydration. In the future, chemical modification of GAGs with precise patterns of acidic groups may provide further insights in this conjecture.

Section 4.1 is reproduced from<sup>174</sup>.



## 4.2 Proton conductivity of the gel within the electrosensory organs of cartilaginous fishes

Although recent studies have identified various components of AoL gel, it has remained unclear how the molecules are structurally arranged and how their structure influences the function of the organs. Here we describe the structure of AoL gel by microscopy and small-angle X-ray scattering and infer that the material is colloidal in nature. To assess the relative function of the gel's protein constituents, we compared the microscopic structure, X-ray scattering, and proton conductivity properties of the gel before and after enzymatic digestion with a protease. We discovered that while proteins were largely responsible for conferring the viscous nature of the gel, their removal did not diminish proton conductivity. The findings lay the ground work for more detailed studies into the specific interactions of molecules inside AoL gel at the nanoscale.

### 4.2.1 Introduction

Electroreception, the ability of some animals to detect electric fields, is widespread among vertebrates. Some of the most well-studied electroreceptive animals are rays, skates, sharks, and chimaeras – cartilaginous fishes of the class Chondrichthyes. These fishes use specialized electrosensory organs for the detection of low-frequency electric fields from biological sources such as prey or mates, and even for navigating using earth's geomagnetic field.<sup>175, 176</sup> These electrosensory organs, called Ampullae

of Lorenzini (AoL), are observable externally as small pores that are open to the surrounding environment (Figure 12). In sharks and chimaeras, pores are most concentrated on the snout and around the mouth, whereas in skates and rays, they are more widespread across the ventral and dorsal surfaces of the animals.<sup>177</sup> AoL pores lead into tubular collagen-wrapped canals of varying lengths and diameters (depending on species and location on the body) that are lined on the inside by two layers of epithelial cells. At the distal end of each canal is a bulbous alveolus containing electrosensory hair cells that synapse with neurons connected to the medulla of the brain (Figure 12). Importantly, the organs are filled with a viscoelastic gel that can be extracted by applying pressure to the skin adjacent to AoL pores and subjected to biophysical examination. While the sensory capabilities of the AoL have been studied in detail over the past several decades, the process by which signals move from the environment through the organs, and how the gel is involved, remains a subject of debate.<sup>176</sup>

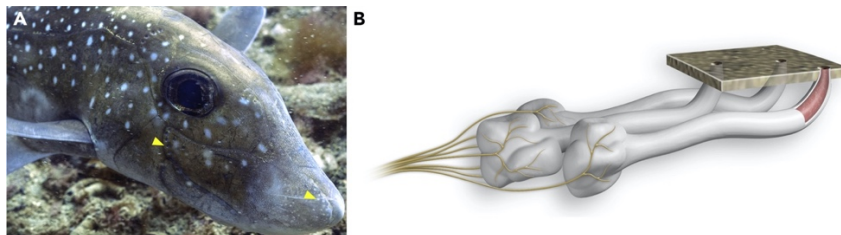


*Figure 12 Anatomy of Ampullae of Lorenzini (AoL)(A) An image showing a type of chimaera called a spotted ratfish (Hydrolagus colliei). Yellow arrowheads delineate the locations of some AoL pores. Image taken by Mick Otten.(B) A diagram showing*

*three AoL below the skin surface. Pores lead into canals filled with a gel (as made visible by the cutaway). Neurons (yellow) synapse with specialized electrosensory cells in the alveoli and project onto the hindbrain.*

Research in the 1960s showed that AoL gel is approximately 95% water containing Na<sup>+</sup>, K<sup>+</sup>, Cl<sup>-</sup>, and urea.<sup>178</sup> By measuring the relative abundances of hexosamines, sulfates, and other chemical groups, researchers identified that the gel contains various “mucopolysaccharides,” but the specific identities of these components have remained unknown until recent years. AoL gel extracted from three fish species demonstrated extremely high proton conductivity, higher than that of any other reported biological material. It has been proposed that keratan sulfate, a glycosaminoglycan, is a component of AoL gel and responsible for conferring the substance’s proton conductive properties. Various studies have attempted to uncover the molecular make up of AoL gel, most with a focus on polysaccharides and proteins. Cellular contamination during AoL gel extraction, however, makes the interpretation of proteomic data sets challenging. We recently reported evidence suggesting that chitin is another polysaccharide component of the gel, but it remains unknown if the chitin molecules are modified in some way or complexed with other components in order to promote solubility in the aqueous gel. Major gel-forming components have been shown to exist as fibrous or rod-like particles, flexible coils, spherical particles, or linear molecules held together by crystalline junctions.<sup>179</sup> However, it is still unclear how the molecular components of AoL gel are arranged and how they

contribute to the gelatinous nature of the material. Furthermore, it is unknown how the gel's viscoelastic structure factors into the proton conductivity of the substance. Using data from proteomics and polysaccharide analyses, Zhang et al. proposed a hypothetical model of AoL gel structure consisting of actin filaments holding together a scaffold of mucins bound to keratan sulfate molecules.<sup>180</sup> Zhang et al. based their model on inferred interactions of gel components that they identified using chemical extraction methods and proteomics; the model was not based on biophysical structural data. Here, we describe an entirely different approach to studying the structure of AoL gel samples from spotted ratfish (*Hydrolagus coliei*) by small-angle X-ray scattering (SAXS), scanning electron microscopy (SEM), and atomic force microscopy (AFM). To understand the influence of the gel's protein component specifically, we digested gel with the proteolytic enzyme, proteinase K, and compared the gross morphology and scattering properties of gel before and after protein removal. Furthermore, we studied the influence of proteins on the proton conductivity of the material using electrochemical impedance spectroscopy. Our results suggest a different model for the gel structure than had previously been suggested.

#### 4.2.2 Result

In order to develop an understanding of the functional differences between AoL gel before and after proteolytic digestion, we compared the proton conductivity of native AoL gel from *H. coliei* and proteinase-K-treated gel with alternating current (a.c.) electrochemical impedance spectroscopy (EIS) (Figure 13). Both gel samples were

dialyzed against H<sub>2</sub>O before measurements to remove other ions that could contribute to the conductivity. The Nyquist plots of both native and digested AoL gel show semicircles in the high-frequency region and an inclined spur in the low-frequency region (Figure 14). These features are fingerprints of materials with predominant ionic conductivity.<sup>181</sup> We calculated the conductivity using a simple equivalent circuit<sup>182</sup> (Figure 15). For native AoL gel, we calculated the effective conductivity to be  $5 \pm 3.5 \text{ mS cm}^{-1}$ , which is consistent with the value of the conductivity ( $2 \pm 1 \text{ mS cm}^{-1}$ ) of AoL gel from other cartilaginous fish species measured previously<sup>183</sup> using transmission line measurement devices. Given the variability associated with samples extracted from biological specimens, the agreement of the values within the uncertainty range is remarkable. For the digested gel, we calculated the effective conductivity to be  $22 \pm 8.5 \text{ mS cm}^{-1}$ . The sizable error observed with both measurements comes from the uncertainty associated in evaluating the thickness of gel material in the devices. Regardless, it appears that the conductivity of the proteinase-K-digested material is higher than that of native AoL gel. To further confirm that the charge carriers in the gel are protons, we studied the kinetic isotope effect by loading the gel with H<sup>+</sup> and D<sup>+</sup> in water (H<sub>2</sub>O) vapor and deuterium oxide (D<sub>2</sub>O) vapor, respectively.<sup>183</sup> The resistance of both native and digested AoL gel in D<sub>2</sub>O vapor was significantly higher than that in water as expected when protons dominate the conductance of the material because the mobility of D<sup>+</sup> is approximately half of the mobility of H<sup>+</sup> (Figures 5D and 5E). This result provides

confirmation that AoL gel from *H. collicei* is a proton conductor at high relative humidity and corroborates our previously reported observations.

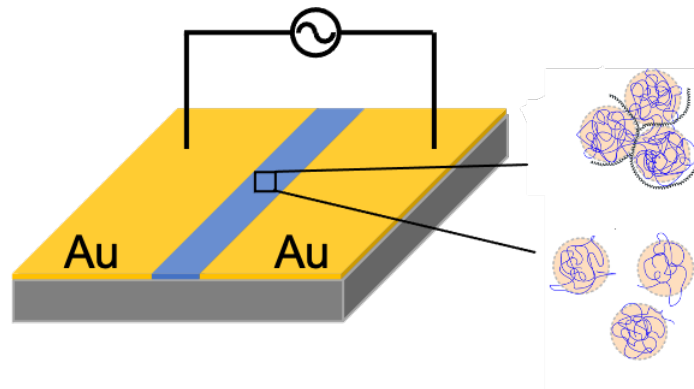


*Figure 13 Proton conductivity of *H. collicei* AoL gel before and after proteinase K digestion. Two-terminal device used for EIS measurement.*

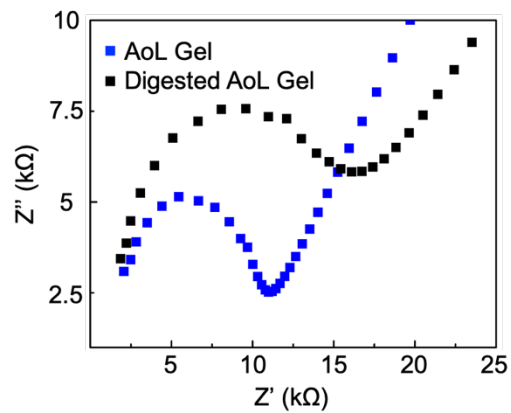


*Figure 14 Nyquist plots of native AoL gel (blue) and digested AoL gel (black) at 90% relative humidity.*

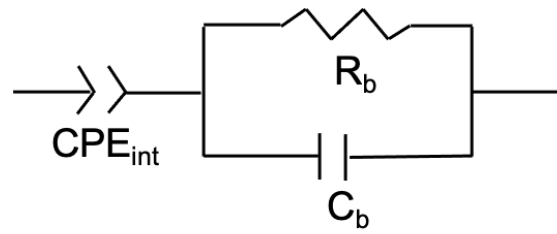


Figure 15 Equivalent circuit model. A constant phase element (CPE) was used to describe the nonideal interface capacitance;  $R_b$  and  $C_b$  represent the resistance and capacitance of the sample, respectively.

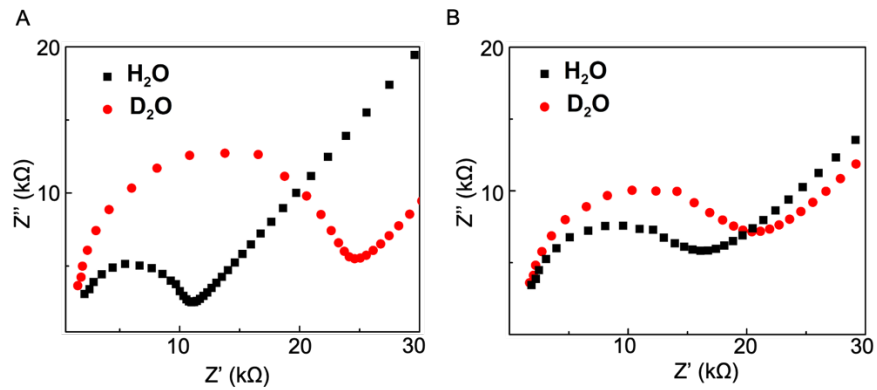


Figure 16 Nyquist plots of native *H. colliei* AoL gel (D) and proteinase-K-digested *H. colliei* AoL gel (E) in the presence of  $H_2O$  vapor (black) and  $D_2O$  vapor (red).

### 4.2.3 Discussion

Evidence from microscopic examination suggested that AoL gel from *H. colliei* is colloidal in nature, with spherical globules comprising a substantial portion of the observable macromolecular structure. SAXS data using concentrated AoL gel revealed a scattering peak corresponding to a real-space length scale of 22 nm. Globules were still observable by AFM in proteolyzed gel samples, whereas the 22-nm peak was completely absent from the SAXS plot generated using the same material. Taken together, these findings suggest that the 22-nm peak represents a length scale related to the average separation of the spherical globules within AoL gel. In addition, for the undigested samples, the range of length scales over which we observed close to ideal chain behavior (6–90 nm) suggests that there is some degree of chain interdigitation between globules in the aggregated structure, producing a continuous polymer network. It is important to point out that ultracentrifugation may have impacted the size of the polymer globules in native AoL gel; therefore, the 22-nm peak would represent a lower correlation length limit. It should also be noted here that other polymer structures, such as fractal aggregates, may possibly give rise to scattering patterns similar to the one reported. Detailed model fitting procedures often used for SAXS data are precluded here owing to the unknown composition of the AoL gel, and thus, future experiments will be necessary to elucidate the internal structure of the globules in more detail. When ambiently dried AoL gel was imaged with AFM, rope-like structures were observed weaving among the globules. These structures were absent in proteinase-K-digested gel, which suggests that they consist



of proteins involved in holding the polymer network together. Elimination of the setethering proteins by enzymatic digestion seemingly collapsed the polymer network, and although the globules remained, they became dispersed randomly in solution. It is still unclear what materials compose the globules entirely. The fact that the globules were still clearly resolvable after proteinase K digestion makes it unlikely that they are highly composed of proteins. Therefore, the material remaining after proteinase K digestion could be composed of polysaccharides, lipids, or a combination of macromolecules. However, the globules comprising AoL gel resemble published images of chitosan nanoparticles;<sup>184</sup> moreover, crystals reminiscent of chitin nano whiskers were formed when the carbohydrate-extracted gel material was sonicated.<sup>185</sup> These observations likely indicate that chitin makes up a substantial portion of the spherical globules, perhaps functioning as a scaffold that organizes proton-conductive keratan sulfate molecules. By comparing the proton conductivity of native and proteinase-K-digested ratfish gel, we learned that proteins may not play a direct role in the conductivity of the material, despite their clear contribution to the gel's observed viscosity. In prior work,<sup>183</sup> we speculated that sulfated polysaccharides, namely keratan sulfate molecules, were responsible for conferring the observed proton conductivity of AoL gel. If we consider the gel as a mixture of highly conductive polysaccharides<sup>174</sup> and less conductive proteins, removing the proteins should lead to a more conductive material as observed here. Nonetheless, the fact that the digested gel is more conductive than native gel confirms that proteins are not directly responsible for the observed proton conductivity. These data, along with the

SAXS spectra, do not indicate which specific proteins play a role in the gel's structure and function. However, our results suggest that proteins do confer the gelatinous nature of the material and contribute to the maintenance of the structured polymer network but are not critical for proton conductivity. Interestingly, we noticed that approximately one out of four measurements on the digested gel sample contains a Nyquist plot that hints at the presence of two semicircles at high and mid frequencies as well as a clear polarization spike at low frequency. Potential reasons for the presence of two semicircles include grain boundary between globules<sup>186</sup> or a nonuniform current distribution.<sup>187</sup> It is possible that the lack of an organized structure in the digested gel may affect the proton conduction and give rise to the two semicircles. This observation also suggests that the proteins may play an indirect role in the proton transport by organizing the polyglycans responsible for the proton conduction. Finally, we note that our proposed model for the structure of the AoL gel is intrinsically different from that given by Zhang et al.<sup>180</sup> This is, in part, due to differences in the data types used. The model of Zhang et al. was generated by inference using proteomics data from the AoL gel and presumptive scaffolding of keratan sulfate, conceptually similar to the bottle-brush model of aggrecan.<sup>188</sup> In contrast, our model is based on AFM and SEM imaging along with corroborating SAXS spectral analysis and proposes a colloidal gel organization. We never observed anything reminiscent of bottle-brush structures in AFM, and given the published sizes of such aggrecan bottle brushes (R200 nm), we doubt that the globules are composed of smaller subunits of such structures. Regardless, it will be important to subject both

models to further physicochemical and structural analyses in order to better deduce the underlying electrosensory mechanisms of the AoL of cartilaginous fishes.

#### 4.2.4 Limitations of the study

To study the molecular makeup and structure of AoL gel, we needed to extract gel material from the tubular organs of deceased fish by applying physical pressure to the skin around the AoL pores. Therefore, all of the studies described here were limited by inevitable contamination of cellular and mucosal debris during the gel's extraction process. Because of this limitation, when studying the macromolecular components of AoL gel, we eliminated the gel's entire protein population as opposed to specific protein species. We also acknowledge that ultracentrifugation of gel samples used for SAXS may have introduced subtle changes to the scattering properties of the materials. Another limitation, as mentioned in the main text, was the need to desiccate AoL gel prior to imaging with AFM and SEM. It is unclear whether or not the observed features of desiccated gel reflect the native structure of aqueous gel. We used supercritical drying in an attempt to overcome this limitation. Finally, when we performed proton conductivity measurements, we filled two circular spacers with native gel and proteinase-K-digested gel. The native gel was extremely viscous, whereas the digested material was a liquid, and the two substances did not necessarily contain the same proportion of dissolved molecules.

Section 4.2 is reproduced from <sup>189</sup>.

### 4.3 Proton conductivity of Single-Crystal Polycationic Polymers

The efficient preparation of single-crystalline ionic polymers and fundamental understanding of their structure–property relationships at the molecular level remains a challenge in chemistry and materials science. Here, we describe the single crystal structure of a highly ordered polycationic polymer (polyelectrolyte) and its proton conductivity. The polyelectrolyte single crystals can be prepared on a gram-scale in quantitative yield, by taking advantage of an ultraviolet/sunlight-induced topochemical polymerization, from a tricationic monomer - a self-complementary building block possessing a preorganized conformation. A single-crystal-to-single-crystal photopolymerization was revealed unambiguously by in situ single-crystal X-ray diffraction analysis, which was also employed to follow the progression of molecular structure from the monomer, to a partially polymerized intermediate, and, finally, to the polymer itself. Collinear polymer chains are held together tightly by multiple Coulombic interactions involving counterions to form two-dimensional lamellar sheets (1 nm in height) with sub-nanometer pores (5 Å). The polymer is extremely stable under 254 nm light irradiation and high temperature (above 500 K). The extraordinary mechanical strength and environmental stability in combination with its impressive proton conductivity ( $\sim 3 \times 10^{-4} \text{ S cm}^{-1}$ ) endow the polymer with potential applications as a robust proton-conducting material. By marrying supramolecular chemistry with macromolecular science, the outcome represents a

major step toward the controlled synthesis of single-crystalline polyelectrolyte materials with perfect tacticity.

#### 4.3.1 Introduction

A good fundamental understanding of the structure–property relationships of polymers at the molecular level remains a bottleneck in chemistry and materials science.<sup>190</sup> Topochemical polymerization a lattice-controlled crystal-to-crystal synthetic protocol offers (Figure 17e) a promising solution for the preparation of macroscopically sized single-crystalline polymers,<sup>191</sup> suitable for single-crystal X-ray diffraction (SCXRD). This solid-state technique not only provides the accurate chemical composition but also affords detailed bonding information, thereby offering guidelines for the further development of materials with finely tuned properties.<sup>192</sup> The high crystallinity of these materials can also enhance many performance-based applications. On the other hand, polyelectrolytes have attracted considerable attention in the field of all-solid-state batteries<sup>193</sup> and fuel cells.<sup>194</sup> The topochemical synthesis of ionic polymeric or polyelectrolyte single crystals (PSCs), however, remains elusive and particularly challenging because of the strong Coulombic repulsive interactions (Figure 17b) which operate during the self-assembly of a pair (Figure 17c) of cationic or anionic appendages from two ionic monomers (Figure 17d). Here, we present a rational design (Figure 17e) for the efficient preparation of PSCs on the basis of a careful selection of appendage<sup>195</sup> in tricationic monomers: they dictate an ensemble of weak interactions and spatial alignments, by combining the principles of

supramolecular chemistry and macromolecular science. First of all, we employ the self complementary both with respect to shape and charge distribution interactions (Figure 17c) between pyridinium-based functional groups, which have been demonstrated by us to be a powerful tool for directing the hierarchical assembly of multicharged molecules, involving there pulsive monomeric units with optimal proximity for topochemical reactions.<sup>196</sup> Second, we have chosen (Figure 17d) the triolefinic tripyridinium monomer 13+, which is expected to adopt a stable conformation in three dimensions and so preorganize discrete reaction sites into an infinite and highly ordered supramolecular network.<sup>197</sup> Last but not least, a certain degree of flexibility highlighted by the black dotted circles in Figure 17d associated with the three appendages of the monomeric structure is also considered in order to cushion the strain released from conformational changes which take place during solid-state reactions and so prevent fragmentation of the crystals. The remarkable advantage of this strategy is it sability to obtain large-sized polycationic polymer single crystals quantitatively by taking advantage of an ultraviolet/sunlight induced single-crystal-to-single-crystal (SCSC) topochemical photopolymerization (Figure 17) of the preorganized monomers, resulting from the crystallization. (E)-4-(2-(Pyridin-4-yl)vinyl) pyridinium units were chosen as reactive sites because of their well-established [2+2] photodimerization, both in the solution phase<sup>195</sup> and in the solid state.<sup>198</sup>

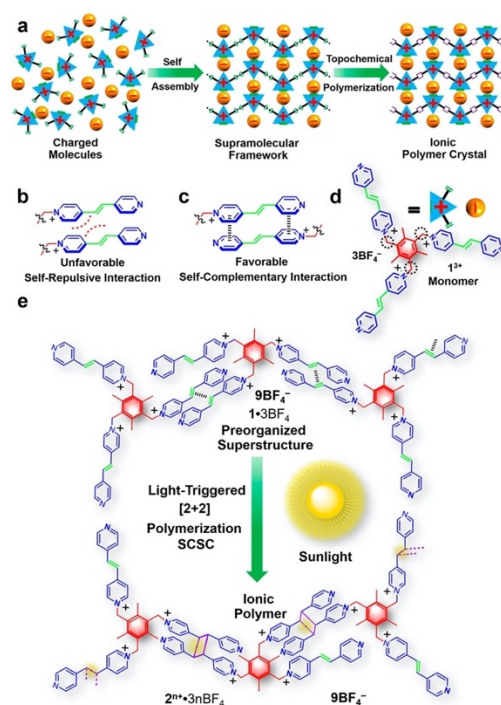
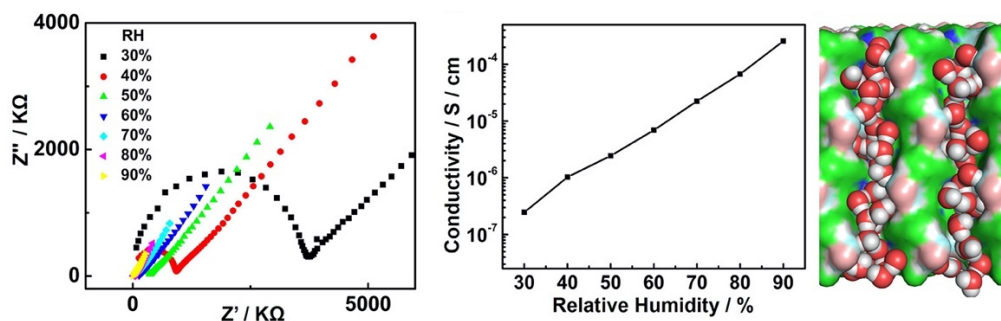


Figure 17 Design concept and strategy for the synthesis of single-crystalline polycationic polymers. (a) Schematic diagram for the preparation of polymer crystals from the crystallization of preorganized monomers, followed by the topochemical photopolymerization. (b) The unfavorable self-repulsive interaction in a parallel manner. (c) The self-complementary interactions facilitate the proximity of two reactive sites in an antiparallel manner. (d) Structural formula of the monomer. (e) Scheme for photopolymerization.

The Single-Crystal-to-Single-Crystal (SCSC) Photopolymerizations, characterization and mechanical properties are omitted here. More details can be found in the published work.<sup>182</sup>

### 4.3.2 Proton Conductivity

Given the ordered 1D ionic channels, high stability toward heat, and concentrated acids, we investigated the proton conductivity of the polymer using electrochemical impedance spectroscopy (EIS). The Nyquist plots show (Figure 18) a semicircle in the high frequency region and an inclined spur in the low-frequency region, both observations that can be associated with a simple equivalent circuit (Figure 20). The values (Figure 18) for proton conductivities are highly humidity dependent and show a significant increase from  $2.5 \times 10^{-7} \text{ S cm}^{-1}$  at 30% relative humidity (RH) to  $2.6 \times 10^{-4} \text{ S cm}^{-1}$  at 90% RH. A distinct isotope effect confirmed that the polymer is a proton conductor (Figure 22).<sup>199</sup> The impressive proton conductivities ( $\sim 3 \times 10^{-4} \text{ S cm}^{-1}$ ) at room temperature are broadly comparable with the values for covalent organic frameworks (COFs) measured under similar conditions. The simulated structure reveals that water molecules form hydrogen-bonded networks in the confined environment of the 1D channels, suggesting the operation of a Grotthuss mechanism<sup>200</sup> in which hydronium ions pass their protons to neighboring water molecules along the well-packed hydrogen-bonded chains.





*Figure 18 Nyquist plots showing the impedance of the polymer at 298 K with varying relative humidity (RH) between 0.1 MHz and 0.1 Hz. The Nyquist plots of 50%–90% RH are also shown in Figure S34 in detail. (e) The dependence of the proton conductivity of the polymer on the RH. (f) A snapshot of water chains in the 1D channels of the simulated structure. H<sub>2</sub>O molecules are illustrated as space-filling representations, while the organic fragments and BF<sub>4</sub><sup>-</sup> counterions are shown as surface model representations.*

Samples were mechanically ground into sufficiently small particle sizes. Impedance data were recorded by Autolab PGSTAT128N between 100 kHz and 0.1 Hz at 20 mV amplitude, and analyzed by Nova 2.0 software. A simple equivalent circuit was used here to simulate the Nyquist plots. Experiments were carried out in a home-made humidity control chamber with N<sub>2</sub> atmosphere. Before each measurement, the sample was incubated for 2 h at different humidities to reach a stable status.

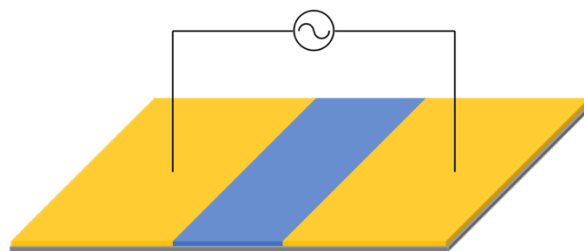


*Figure 19 Two-terminal device used for EIS measurement. The two-terminal devices used in EIS measurements were fabricated on glass. Prior to device fabrication, the*

substrates were cleaned by sequential sonication in Me<sub>2</sub>CO and iPrOH. Then, a 10 nm Titanium adhesion layer overlaid with a 100 nm gold was electron-beam evaporated onto the clean substrates through a shadow mask. The dimensions of the paired electrodes were 2.5 cm wide by 2.0 cm long with an inter-electrode separation of 50 μm. The devices were completed by dropping cast the bulk polymer powders suspended in MeCN solution directly onto the electrode patterns, and the resulting films were allowed to dry in air overnight

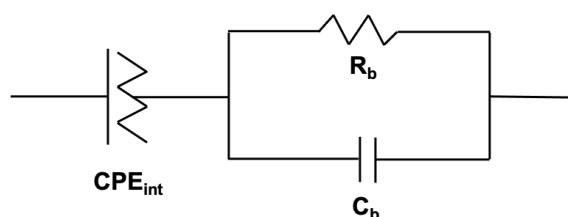


Figure 20 Equivalent circuit model used to fit the impedance data. A Constant Phase Element (CPE) was used to describe the non-ideal interface capacitance, R<sub>b</sub> and C<sub>b</sub> represent the resistance and capacitance of the sample, respectively.

The conductivity (σ) of the sample is calculated with the equation below:

$$\delta = \frac{L}{R_b A}$$

Where S and L are the cross-sectional area and thickness of the sample, respectively, and R<sub>b</sub> is the value of resistance, which was obtained from the impedance plots

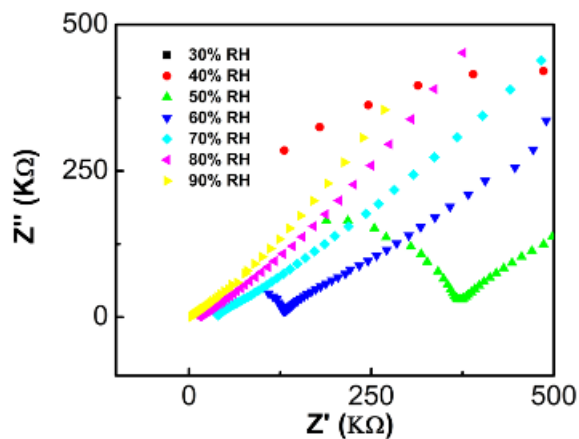


Figure 21 Nyquist plots showing the impedance of the polymer between 0.1 MHz–0.1 Hz at 298 K with varying RH. Zoom-in of Figure 18.

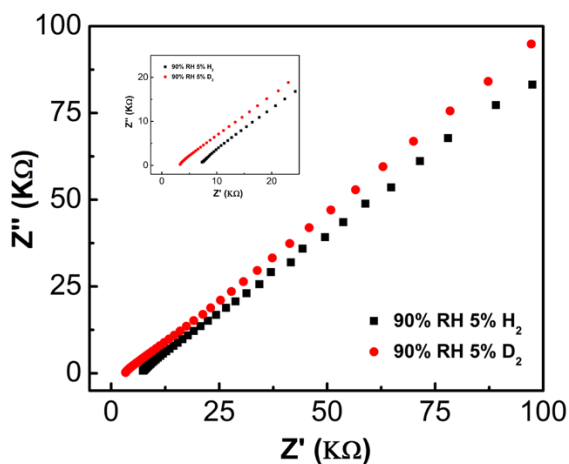


Figure 22 Kinetic isotope effect of the polymer at 90% RH. A Nyquist plot for the polymer-bridged two-terminal device in the presence of water vapour (black) and in the presence of deuterium oxide vapour (red). The conductivity calculated from the Nyquist plots are  $3 \times 10^{-4} \text{ S cm}^{-1}$  ( $\text{H}^+$ ) and  $1.4 \times 10^{-4} \text{ S cm}^{-1}$  ( $\text{D}^+$ ), respectively

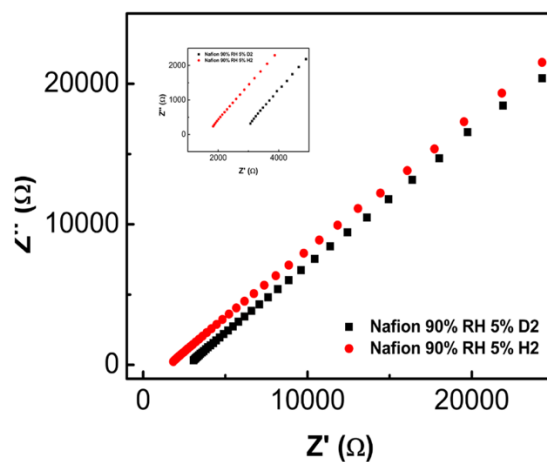


Figure 23 Nyquist plot of Nafion at 90% RH, yielding a value of  $0.1 \text{ S cm}^{-1}$

#### 4.3.3 Conclusion

In summary, we announce a strategy for the quantitative synthesis of polyelectrolyte single crystals with precise control over composition, regioregularity, stereoregularity, and tacticity, from a tricationic monomer. A single-crystal-to-single crystal topochemical photopolymerization has enabled us to gain considerable insight into the molecular structure of the final polymers. The positively charged polymer chains are aligned periodically and held tightly together by multiple ionic interactions with tetrafluoroborate counterions to form 2D monolayer sheets in lamellar crystals. A gram-scale preparation, relying on ultraviolet/sunlight-triggered polymerization, has allowed us to synthesize enough of the polymer to be able to investigate its physicochemical properties and speculate about its potential practical applications.

We have demonstrated that the highly ordered polycationic structure endows this charged polymer with valuable properties. High proton conductivities, in combination with the remarkable mechanical properties and the high thermal stabilities of these polyelectrolytes, point to their promising applications as proton-conducting materials. A comprehensive understanding of how molecular structures dictate proton diffusion in polyelectrolytes is at the heart of the development of better proton conductors. The modular synthetic strategy and fundamental proof-of-concept study of proton conductivities in single-crystalline polyelectrolytes provide compelling clues for the design of novel proton conducting materials that possess better performance characteristics than those exhibited by current state-of-the-art materials.

Section 4.3 is reproduced from <sup>201</sup>.

## 4.4 Proton conductivity of Nanotubes

Macrocycles that assemble into nanotubes exhibit emergent properties stemming from their low dimensionality, structural regularity, and distinct interior environments. We report a versatile strategy to synthesize diverse nanotube structures in a single, efficient reaction by using a conserved building block bearing a pyridine ring. Imine condensation of a 2,4,6-triphenylpyridine-based diamine with various aromatic dialdehydes yields chemically distinct pentagonal [5 + 5], hexagonal [3 + 3], and diamond-shaped [2 + 2] macrocycles depending on the substitution pattern of the aromatic dialdehyde monomer. Atomic force microscopy and in solvo X-ray diffraction demonstrate that protonation of the macrocycles under the mild conditions used for their synthesis drives assembly into high-aspect ratio nanotubes. Each of the pyridine-containing nanotube assemblies exhibited measurable proton conductivity by electrochemical impedance spectroscopy, with values as high as  $10^{-3}$  S m<sup>-1</sup> (90% R.H., 25 °C) that we attribute to differences in their internal pore sizes. This synthetic strategy represents a general method to access robust nanotube assemblies from a universal pyridine-containing monomer, which will enable systematic investigations of their emergent properties.

### 4.4.1 Introduction

Macrocycles that assemble into extended one-dimensional nanotubes exhibit emergent properties because of their low dimensionality, structural regularity, and

distinct interior environments.<sup>202</sup> These features are of potential interest for ion transport,<sup>203</sup> sensing,<sup>204</sup> catalysis,<sup>205</sup> and separations.<sup>206</sup> To access the diverse properties associated with these potential uses, macrocycles that form nanotubes must be derived from readily accessible building blocks and tolerate structural variation without compromising their interaction energies and ability to assemble. General methods to access designed, high-aspect ratio nanotubes remain limited. Noncovalent assemblies based on relatively weak supramolecular interactions are less likely to tolerate significant structural variation and can exhibit poor mechanical integrity.<sup>207</sup> Developing a robust and chemically general macrocycle assembly strategy will enable broad explorations into nanotube design, their emergent properties, and stimuli-responsive<sup>208</sup> or even out-of-equilibrium assembly processes.<sup>209</sup> We recently found that the protonation of imine-linked macrocycles triggers strong electrostatic and solvophobic interactions that drive the formation of high-aspect ratio nanotubes.<sup>210</sup> However, macrocycle assembly that relied exclusively on imine protonation only assembled in the presence of excess acid, whereas lower acid concentrations accelerated macrocycle hydrolysis.<sup>211</sup> We subsequently identified a single macrocycle based on pyridine-2,6-dicarboxaldehyde that was assembled using sub-stoichiometric quantities of acid, giving rise to robust assemblies that formed fibers with mechanical properties comparable to covalent linear polymers (Figure 24).<sup>210</sup> Here, we dramatically expand the modularity of this design by including the pyridine heterocycle and hydrophobic solubilizing groups in a single monomer, thereby enabling the efficient incorporation of many dialdehydes into macrocycles

that assemble into high-aspect ratio nanotubes under mild conditions (Figure 24). Through this approach, ten distinct macrocycles and nanotubes with a range of structural features including different shapes, channel sizes, and chemical functionalities were realized. Because each of these macrocycles forms nanotubes in the presence of less than one equivalent of acid per pyridine moiety, we hypothesized that protons might be mobile within the nanotube interiors, similar to recent reports on proton conduction within assembled D,L- $\alpha$ -cyclic peptides<sup>212</sup> and nanotubes based on metal–ligand coordination bonds.<sup>213</sup> Electrochemical impedance spectroscopy of four nanotube structures indicated that each system exhibited measurable protonic conductivity, with the highest value of  $1.6 \text{ \AA} \sim 10^{-3} \text{ Sm}^{-1}$  at 90% relative humidity and 25 °C. Across the four nanotubes studied, the protonic conductivities appear to depend on the size and/or shape of the macrocycle. These findings highlight the potential of well-defined supra molecular assemblies with precisely installed functional groups for ion transport. Overall, this versatile synthetic platform to target designed nanotubes will enable the broad exploration of synthetic 1D nanostructures, their emergent properties, and their eventual incorporation into devices.



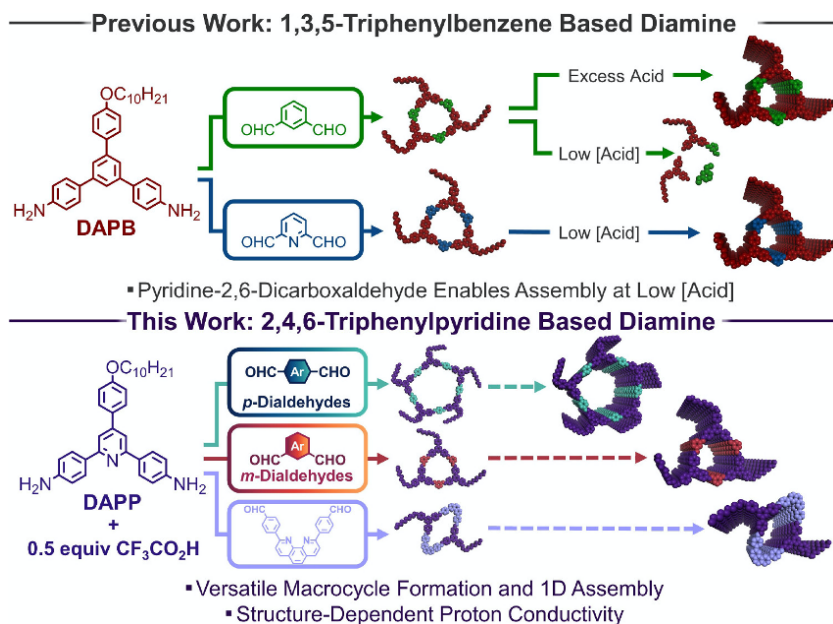


*Figure 24 Accessing high-aspect ratio nanotubes via acid-mediated macrocycle assembly. (Top) Previous work in which assembly under mild conditions was dictated by a pyridine-2,6-dicarboxaldehyde monomer residue, resulting in a system that assembles under mild conditions but is not easily generalized. (Bottom) A modular approach to imine-linked macrocycle formation and assembly relying on a pyridine junction embedded within the diamine monomer, allowing access to chemically and structurally diverse nanotubes in a single step.*

The preparation and characterization of nanotubes are omitted here and can be found in the published work.<sup>214</sup>

#### 4.4.2 Result and discussion

Accessing nanotubes of different sizes and chemical functionalities under sub-stoichiometric acid loadings motivated studies of their proton conductivity. Nanotubes assembled from pyridine-containing imine-linked macrocycles in the presence of 0.5 equiv  $\text{CF}_3\text{CO}_2\text{H}$  per pyridine group demonstrated pore size dependent proton conductivity, with nanotubes assembled from DAPP-IDA exhibiting a conductivity 2 orders of magnitude greater than that of nanotubes assembled from DAPP-PDA or DAPP-PhenDA. To measure the proton conductivity, nanotubes were drop-cast onto a two-terminal device, between two Au contacts ( $2.5 \text{ \AA} \sim 2.0 \text{ cm}$ ) separated by  $50 \text{ \mu m}$ , and subjected to electrochemical impedance spectroscopy (EIS) at 90% relative humidity (R.H., Figure 25A). EIS data was analyzed using Nyquist plots fit to a standard equivalent circuit consisting of a constant phase element ( $\text{CPE}_{\text{int}}$ ) in series with a parallel combination of a resistor ( $R_b$ ) and a capacitor ( $C_b$ , Figure 25B). Despite variation in nanotube shape and number of pyridine moieties, nanotubes assembled from DAPP-PDA, DAPP-IDA, and DAPP-PhenDA all yield a semicircle Nyquist plot in the high-frequency region and an inclined spur in the low frequency region (Figure 25C–F).

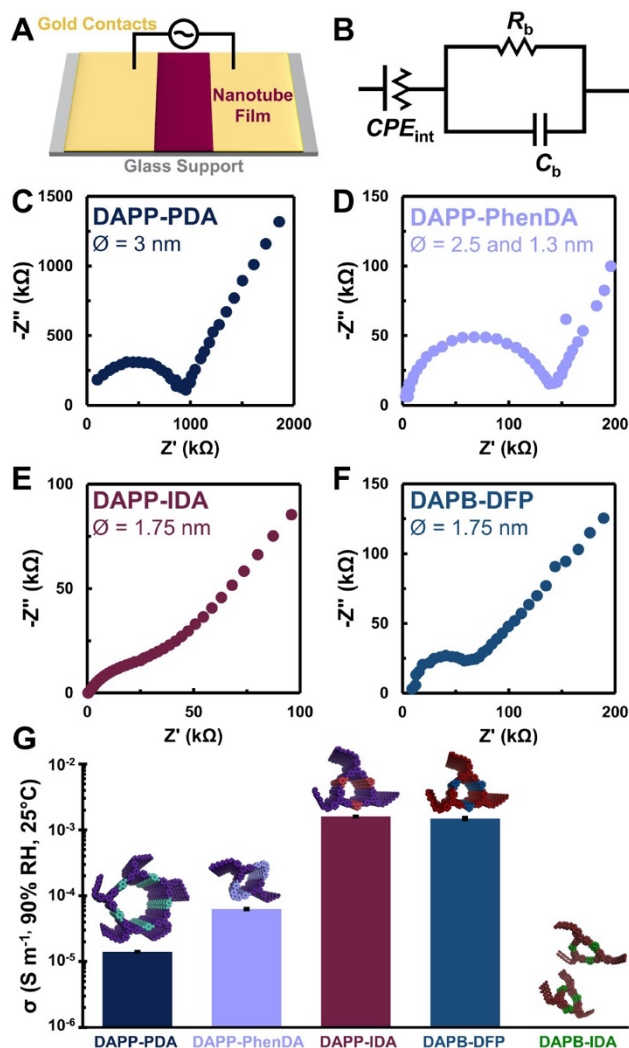


Figure 25 Structure-dependent proton conductivity of nanotubes prepared via acid-mediated macrocycle assembly. (A) Illustration of the two-terminal device used for EIS measurements. (B) Diagram of the equivalent circuit model used to analyze the impedance data. The circuit consists of a Constant Phase Element ( $CPE_{int}$ ) in series with both a resistor ( $R_b$ ) and a capacitor ( $C_b$ ), which correspond to the film/electrode interface capacitance, the film bulk resistance, and the film bulk capacitance, respectively. (C–F) Nyquist plots showing the impedance of nanotubes derived from

*DAPP-PDA, DAPP-PhenDA, DAPP-IDA, and DAPB-DFP macrocycles at 25 °C with 90% R.H. The conductivities calculated from these plots were  $1.4 \times 10^{-5}$ ,  $6.3 \times 10^{-5}$ ,  $1.6 \times 10^{-3}$ , and  $1.5 \times 10^{-3} \text{ S m}^{-1}$ , respectively. (G) Comparison of observed conductivity values in different macrocycles. The data suggest that an increase in the size of the macrocycle results in lower conductivities, but other factors such as macrocycle shape and packing density may also play a role.*

These observations are fingerprints of proton conductivity, a phenomenon which was further validated by observing a sharp decrease in conductivity due to isotope effects when the same measurements were carried out in the presence of D<sub>2</sub>O (Figure 26).<sup>174</sup> The measured deuterium effect is as expected for protons being the major charge carrier within the nanotubes and rules out the possibility that other ions, such as ions present in the solvent or the acid counterion, contribute substantially to the measured current. All samples demonstrate the hallmarks of proton conductivity, and our observations suggest that the conductivity values of various nanotubes have a pore size dependence. Larger [5 + 5]nanotubes ( $\text{Ø} = 3 \text{ nm}$ ) derived from PDA exhibited low conductivity ( $1.4 \pm 0.0 \times 10^{-5} \text{ S m}^{-1}$ , 90% R.H., 25 °C). However, the smaller but irregularly shaped nanotubes ( $\text{Ø} = 2.5$  and  $1.3 \text{ nm}$ ) derived from PhenDA only showed a moderate conductivity increase ( $6.3 \pm 0.2 \times 10^{-5} \text{ S m}^{-1}$ , 90% R.H., 25 °C). The smallest hexagonal nanotubes ( $\text{Ø} = 1.75 \text{ nm}$ ) derived from IDA produced a conductivity 2 orders of magnitude greater than nanotubes with larger channels ( $1.6 \pm 0.0 \times 10^{-3} \text{ S m}^{-1}$ , 90% R.H., 25 °C), suggesting that the size of the hexagonal

pore and the spacing of pyridine moieties in nanotubes derived from IDA provide an optimal path for proton conduction. Pore size dependent proton conductivity within 1D nanochannels has been previously attributed to water molecules adopting a well organized 1D proton wire configuration in smaller systems, thereby realizing larger conductivity values.<sup>120</sup> Despite the apparent dependence of proton conductivity on nanotube diameter, further studies will be needed to definitively elucidate the origin of enhanced conductivity within various nanotubes and to investigate structure–property relationships that promote proton conductivity within these macrocycle-based assemblies. Furthermore, it is likely that the proton conductivity of the nanotubes can be enhanced by increasing the amount of acid used in their assembly, offering a handle to tune conductivity that is independent of macrocycle structure.<sup>215</sup> Comparison of the conductivity trends in nanotubes derived from DAPP with two additional control systems confirmed that proton transport occurs along the cationic 1D nanochannel. Two additional macrocycles were prepared based on a 1,3,5-triphenylbenzene-based diamine (DAPB) and either DFP or IDA. The former is a structural isomer of DAPP-IDA with an identical assembly profile, while the latter lacks pyridine moieties and substantial 1D order, allowing us to further probe the effects of assembly and nanotube size on proton conductivity. Nanotubes assembled from DAPB-DFP macrocycles exhibit proton conductivities ( $1.5 \pm 0.0 \text{ } \text{\AA}^{-1} \sim 10^{-3} \text{ S m}^{-1}$ , 90% R.H., 25 °C), similar to DAPP-IDA systems.

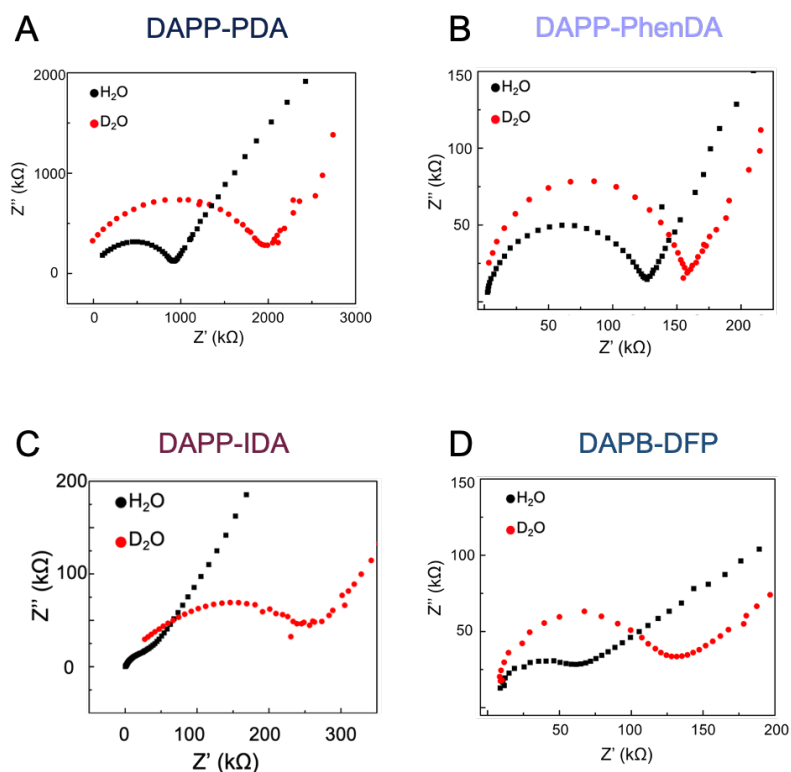


Figure 26 Kinetic isotope effect experiment. Nyquist plots for the polymer-bridged twoterminal device in the presence of water vapor (black) and deuterium oxide vapor (red) of (A) DAPP-PDA, (B) DAPP-PhenDA, (C) DAPP-IDA, and (D) DAPB-DFP nanotubes at 90% R.H.

Furthermore, macrocycles which do not contain any pyridine moieties, and therefore lack substantial 1D order (DAPB-IDA), demonstrate conductivity values at least 3 orders of magnitude lower than those of DAPP-IDA or DAPB-DFP nanotubes (Figure 27). The comparison of these three hexagonal structures suggests that (1) proton conductivity is partially dependent on the pore architecture and (2) substantial 1D order is required for reliable proton transport. Taken together, the results of the

conductivity values obtained for various DAPP-based nanotubes highlight that in order to reliably target optimized performance in a 1Dnanochannel, the chemical functionality and nanotube topology must be independently modifiable. Presumably, using this design strategy to prepare optimally sized nanotubes with higher densities of basic moieties will improve the proton conductivity of these assemblies, thereby enabling explorations into the use of these materials in fuel cell and bioelectronic applications. More broadly, this work demonstrates that structurally well-defined supramolecular assemblies with precisely installed chemical functionalities are promising scaffolds for the development of materials suitable for ion transport.

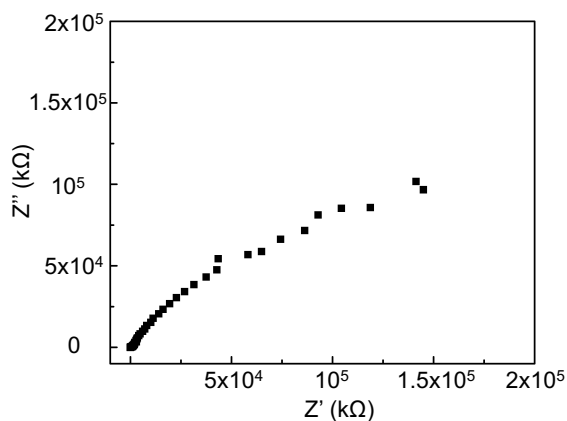


Figure 27 Nyquist plot of DAPB-IDA nanotubes at 90% R.H.

#### 4.4.3 Conclusions

Generalizing the acid-mediated assembly of macrocycles into robust nanotubes will enable access to a broad range of structures and exploration of their emergent properties. Here, we have shown that a 2,4,6-triphenylpyridine-based diamine (DAPP)

enables efficient formation of pentagonal [5 + 5], hexagonal [3 + 3], and diamond shaped [2 + 2] macrocycles depending on the substitution pattern of the aromatic dialdehyde monomer. Protonation of the central pyridine moiety of DAPP under the mild conditions typical for macrocycle synthesis drives macrocycle assembly into high aspect ratio nanotubes, as demonstrated by in solvo XRD measurements and AFM imaging. These structurally well-defined supramolecular polymers with cationic 1D nanochannels demonstrated pore size-dependent proton conductivity, with nanotubes derived from IDA exhibiting a conductivity 2 orders of magnitude greater than those of the nanotubes derived from PDA or PhenDA. These findings, along with the versatility of this synthetic approach, will guide future designs to further improve proton conductivity and further leverage the stimuli responsive nature of the assemblies. Overall, this platform will unlock the potential of functional nanotubes assembled from macrocyclic precursors to provide systems whose emergent properties and functions can be rationally tuned through molecular design.

#### 4.4.4 Experiment section

**Sample Preparation for Proton Conductivity Measurements.** A Two-terminal device was used for electrochemical impedance spectroscopy (EIS) measurements. The two terminal devices used in EIS measurements were fabricated on glass. Prior to device fabrication, the substrates were cleaned by sequential sonication in acetone, isopropanol, and deionized water. After cleaning, a 10 nm Titanium adhesion layer overlaid with a 100 nm gold layer was electron beam evaporated onto the substrates



through a shadow mask. The dimensions of the paired electrodes were 2.5 cm wide by 2.0 cm long with an inter-electrode separation of 50  $\mu\text{m}$ . The devices were completed by drop-casting solutions of the nanotubes in 1,4-dioxane directly onto the electrode patterns. The resulting films were allowed to dry overnight before having their thicknesses measured by profilometry and being subjected to EIS measurements.

Electrochemical Impedance Spectroscopy (EIS). Impedance data were recorded using an Autolab PGSTAT128N between 100 kHz and 0.1 Hz at 50 mV amplitude. The data was subsequently analyzed using a Nova 2.0 software. In doing so, a simple equivalent circuit was used to simulate the Nyquist plots (Figure 4B and S133). Experiments were carried out in a home-made humidity control chamber under an N<sub>2</sub> atmosphere. Before each measurement, the samples were incubated for 24 hours at 90% relative humidity (R.H.) to reach a stable status.

Proton Conductivity Calculation. Proton conductivity values were calculated using the following equation:

$$\delta = \frac{L}{R_b A}$$

Where S and L are the cross-sectional area and thickness of the sample, respectively, and R<sub>b</sub> is the value of resistance, which was obtained from the impedance plots

In this equation,  $A$  is the cross-sectional area of the sample,  $L$  is the length between the two Au terminals, and  $R_b$  is the value of resistance, which was obtained from the impedance data of EIS.

Kinetic Isotope Experiments. Experiments were carried out in a home-made humidity control chamber with  $N_2$  atmosphere. After the EIS measurement using  $H_2O$  vapor, we substituted in  $D_2O$  vapor at 90% R.H., and incubated the sample for an additional 2 hours to reach a stable status. Figure S134 shows the proton conductivity of DAPP-PDA, DAPP-PhenDA, DAPPIDA, and DAPB-DFP nanotubes at 90% RH in both  $H_2O$  vapor (black) and  $D_2O$  vapor (red). We calculated the conductivity from the Nyquist plots using the equivalent circuit in Figure 4B to be  $5.34 \pm 0.74 \times 10^{-6} \text{ S m}^{-1}$  (DAPP-PDA),  $5.05 \pm 0.48 \times 10^{-5} \text{ S m}^{-1}$  (DAPP-PhenDA),  $5.68 \pm 0.2 \times 10^{-4} \text{ S m}^{-1}$  (DAPB-DFP), respectively. It is worth noting that the impedance of DAPP-IDA in  $D_2O$  vapor is much higher than that in  $H_2O$  vapor. We speculate it is due to structural changes that arise in the nanotubes upon replacement of the replacement of  $H^+$  to  $D^+$ , which subsequently changes the charge density within the system.

This section is reproduced from <sup>214</sup>.

## 5. Ion Conducting Hydrogel

Hydrogels have become the material of choice in bioelectronic devices because their high-water content leads to efficient ion transport and a conformal interface with biological tissue. While the morphology of hydrogels has been thoroughly studied, systematic studies on their ionic conductivity is less common. In this section, we present an easy-to-implement strategy to characterize the ionic conductivity of a series of polyelectrolyte hydrogels with different amounts of monomer and crosslinker and correlate their ionic conductivity with microstructure.

Higher monomer increases the ionic conductivity of the polyelectrolyte hydrogel due to the increased charge carrier density, but also leads to excessive swelling that may cause device failure upon integration with bioelectronic devices. Increasing the amount of crosslinker can reduce the swelling ratio by increasing the crosslinking density and reducing the mesh size of the hydrogel, but also cuts down the ionic conductivity. Further investigation on the porosity and tortuosity of the swollen hydrogels correlates the microstructure with the ionic conductivity. These results are generalizable for various polyelectrolyte hydrogel systems with other ions as the charge carrier and provide a facile guidance to design hydrogel with desired ionic conductivity and microstructure for applications in bioelectronic devices.

### 5.1 Introduction

Hydrogels are crosslinked three-dimensional polymeric networks capable of retaining a significant fraction of water within the polymer chains without dissolving.<sup>216</sup> Hydrogels were first used for contact lenses in the 1960's,<sup>88, 217</sup> and have found many bioengineering applications since. Their high-water affinity and porous nature make them good scaffolds to load substances such as functional nanomaterials and cells for applications in drug delivery,<sup>218</sup> wound dressing,<sup>88, 219</sup> tissue engineering,<sup>220, 221</sup> and actuators.<sup>222, 223</sup> In recent years, hydrogels have found use in bioelectronics as the interface between electronic devices and biological systems such as in neuronal recording and stimulation.<sup>12 224, 225</sup> Hydrogels are soft and reduce mechanical mismatch and possible damage to biological tissue.<sup>226</sup> Additionally, hydrogels are wet allowing diffusion of ions and molecules mimicking the physiological environment of cells and tissue and so they are intrinsic ionic conductors.<sup>51, 227</sup> Ionic conductors are particularly important because biological systems use ions and small molecules for information processing and not electrons and holes like semiconductor devices.<sup>2, 228</sup> Hydrogels are good candidate to transfer information between biological system and electronic devices in ion-based bioelectronic device, including ionic diodes,<sup>229</sup> ionic transistors,<sup>230</sup> basic logic circuits,<sup>231</sup> and ion pumps.<sup>3, 23, 24, 109, 232</sup> Although small molecule diffusion in polyelectrolyte hydrogels is well studied for applications such as drug delivery,<sup>233</sup> water desalination,<sup>234</sup> and pressure sensors<sup>235</sup>, relatively less work exists on the study of ionic conduction of hydrogels for bioelectronic applications.

Polyelectrolyte hydrogels are charged monomers crosslinked by crosslinker that forms a network. We aim to study the influence of monomer and crosslinker on the

ionic conduction properties and microstructure of polyelectrolyte hydrogels by designing a series hydrogel with (1) varying amounts of monomer and a fixed amount of crosslinker, (2) varying amounts of crosslinker and fixed amount of monomer. For this investigation, we select 2-acrylamido-2-methylpropane sulfonic acid (AMPSA) as the monomer and poly (ethylene glycol) diacrylate (PEGDA) as the crosslinker. AMPSA is an ionic monomer widely used for the synthesis of polyelectrolyte hydrogels because of its strongly ionizable sulfonate group that dissociates entirely in most of the pH range, and therefore hydrogels derived from AMPSA contain a high number of mobile counter ions.<sup>236</sup> PEGDA is commonly used as the crosslinker in the free-radical polymerization of AMPSA hydrogel, and it is water-soluble, non-toxic, and suitable for biomedical applications.<sup>237</sup> Many studies have been reported on the morphological and mechanical properties of AMPSA/PEGDA polyelectrolyte hydrogel as a function of their ionic group content. For example, Freeman et al. showed that the water uptake and ion sorption of AMPSA/PEGDA hydrogel increases with fixed charge density.<sup>238</sup> Durmaz and co-workers have reported that the elastic modulus of hydrogels first increases with higher charge density but then decreases continuously. Recently, Berggren and co-workers used AMPSA/PEGDA polyelectrolyte hydrogel as the ion exchange membrane for the electrophoretic delivery of different ionic species.<sup>32</sup>

In this paper, we present a comprehensive study on both the ionic conduction properties and the microstructure of a series of AMPSA/PEGDA hydrogels. We found that hydrogels with higher AMPSA show higher ionic conductivity due to the

increased ionized groups and charge carrier density, but also results in excessive water absorption and hydrogel swelling that is detrimental to the integration of hydrogels with bioelectronic devices. By increasing the amount of PEGDA, we reduced the swelling behavior but the ionic conductivity is also decreased. The hinderance of hydrogel microstructure is similar to different ionic species and we further investigated the porosity and tortuosity and correlated the microstructure with the ionic conductivity quantitatively. These results provide simple design rules for tuning hydrogel microstructure and ionic conductivity for applications in bioelectronic devices.

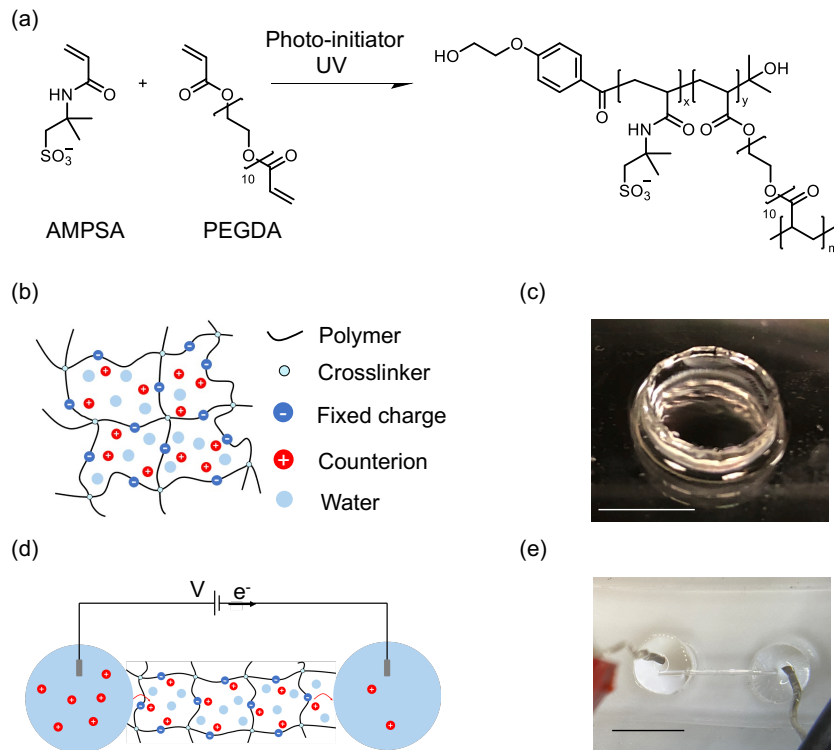


Figure 28 (a) Hydrogel polymerization reaction with AMPSA as the monomer, PEGDA as the crosslinker in the presence of the photo-initiator. (b) Schematic of the crosslinked polyelectrolyte hydrogel with fixed charges on the chain, counterions and water molecules in the polymeric network. (c) Optical image of the bulk hydrogel. Scale bar: 5 mm. (d) Schematic of the hydrogel ionic conductivity measurement experiment setup. A voltage ( $V$ ) across the AgCl electrodes drives  $H^+$  to move through the hydrogel in the capillary fiber, and the ionic flux is translated into an electronic current by the electrochemical reactions at the Ag/AgCl contacts. (e) Optical image of the hydrogel ionic conductivity measurement experiment setup. Scale bar: 5 mm. The hydrogel capillary fiber is between two electrolyte chambers made from PDMS, and AgCl wires are used as the electrode contacts in each chamber.

## 5.2 Results

We prepared AMPSA/PEGDA hydrogels by free radical solution polymerization in the presence of photo-initiator (1-[4-(2-hydroxyethoxy)-phenyl]-2-hydroxy-2-methyl-1-propanone, Irgacure 2959) following a previously published procedure (Figure 28a).<sup>239</sup>

Table 3. Protocols of hydrogels synthesis.

AMPSA (M)	PEGDA (M)	Photo-Initiator (M)
-----------	-----------	---------------------

AP/1/0.5	1	0.5	0.05
AP/2/0.5	2	0.5	0.05
AP/3/0.5	3	0.5	0.05
AP/4/0.5	4	0.5	0.05
AP/2/0.1	2	0.1	0.05
AP/2/0.3	2	0.3	0.05
AP/2/0.5	2	0.5	0.05
AP/2/0.7	2	0.7	0.05

The crosslinked hydrogel has counterions and water molecules in the polymeric network, and fixed charges on the chains (Figure 28b). The hydrogel is transparent and absorbs water when exposed (Figure 28c). To measure the ionic conductivity of the hydrogel, we made the hydrogel into an ionic resistor by filling the hydrogel precursor solution into the glass capillary fiber crosslinked the solution in situ using UV exposure (Figure 29). Prior to the crosslinking, we conducted a surface modification by covalently bonding the hydrogel with the glass capillary fiber with silane A174 (Figure 30). In detail, first we etched the inner surface of glass capillary fiber with 1 M NaOH for 24 hrs to generate hydroxyl groups. Next we flow water (10 min), 10 wt% A174 in toluene (1 hr) and ethanol (10 min) in the channel with 2 ul/min using syringe pump in sequence. The reaction is shown in Figure S1 (a) and the inner surface of glass is modified with alkene. Figure S1 (b) shows the reaction of



hydrogel polymerization and covalent bonding with the silane. Therefore, after the surface treatment, hydrogel

Figure 28d and Figure 28e show a two-terminal experiment setup for the ionic conductivity measurement: the hydrogel fiber is an ionic conductor connected by two electrolytes with AgCl wires as the contacts that serve as the electron-to-ion transducer to close the circuit. For initial measurements, we used 100 mM HCl in both of the electrolytes, and assumed that  $H^+$  are the dominant charge carriers in the hydrogel. We calculated the resistance ( $R$ ) and ionic conductivity ( $\delta$ ) of the hydrogel using Equation 11 and Equation 12, respectively. This approach is simple compared to electrochemical impedance spectroscopy and does not require complicated device fabrication in the cleanroom or expensive equipment such as potentiostat.<sup>182, 199, 214</sup>

$$R = \frac{V}{I} = \frac{L}{A\delta} \text{ Equation 11}$$

$$\delta = \frac{LI}{AV} \text{ Equation 12}$$

where  $R$  is the resistance,  $V$  is the applied voltage,  $I$  is the measured electrical current,  $A$  is the cross-section area of the capillary fiber, and  $\delta$  is the ionic conductivity.

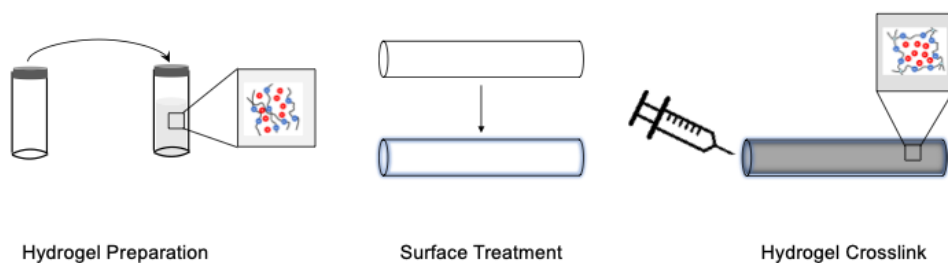


Figure 29 Hydrogel resistor fabrication process.

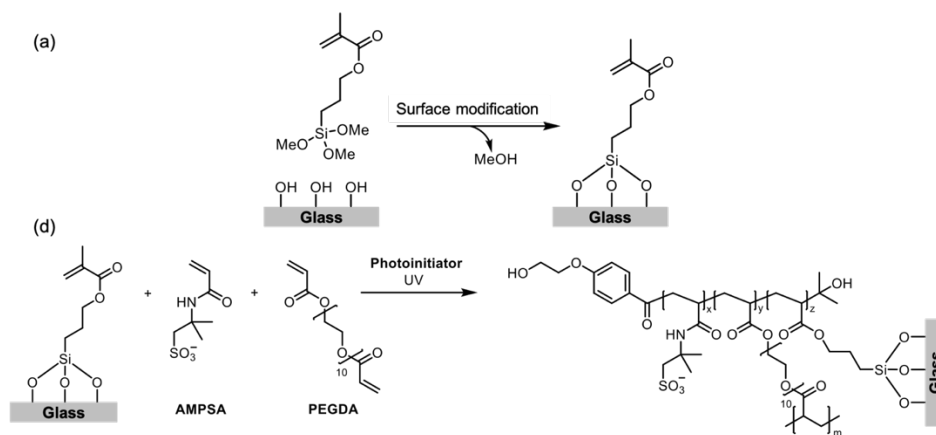


Figure 30 (a) The reaction between the glass and A174. (b) The reaction of hydrogel polymerization and covalent bonding in the glass capillary fiber.

Equation 13 is a general expression of conductivity, and ionic conductivity is usually a summary of all mobile species in the system, where  $q$  is value of charge,  $z_i$  is the charge of each ion,  $n_i$  is charge carrier density per unit volume,  $\mu_i$  is the mobility of each species.

$$\delta = \sum_i n_i |z_i| q \mu_i \text{ Equation 13}$$

In the case of a single ion type contributing to the conductivity, the summation is reduced to one term. The mobility of the ion can be expressed with the Einstein relationship (Equation 14) in term of the diffusion coefficient (D) of the ion in water, where  $K_B$  is the Boltzmann constant and T is the absolute temperature.

$$\mu = \frac{D}{k_B T} \text{ Equation 14}$$

However, ion transport in polyelectrolyte hydrogels is slower than that in the bulk electrolyte because of the interaction of the ions with the hydrogel microstructure. To take this effect into account, we can replace D with the effective diffusion coefficient ( $D_{eff}$ ) in Equation 14. to get the ion mobility in a specific hydrogel.<sup>109</sup> The overall conductivity can then be expressed using Equation 15:

$$\sigma = n \frac{q D_{eff}}{k_B T} \text{ Equation 15}$$

First, we measured the ionic conductivity of all the hydrogels and found that the ionic conductivity increases with more AMPSA and less PEGDA (Figure 31a). When we increase AMPSA from 1 M to 4 M, the ionic conductivity increases from  $8.7 \pm 0.8$  S/m to  $11.6 \pm 0.2$  S/m. When we increased the PEGDA from 0.1 M to 0.7 M, the ionic conductivity decreases from  $14.7 \pm 0.3$  S/m to  $9.7 \pm 0.8$  S/m (Figure 31).

AP/2/0.1 hydrogel shows the highest ionic conductivity to be  $14.7 \pm 0.3$  S/m, which is similar to what has been reported.<sup>32, 240</sup> AP/1/0.5 shows the lowest conductivity,  $8.7 \pm 1.8$  S/m. To understand how AMPSA and PEGDA affect ionic conductivity, respectively, we further studied their influence on the change of charge carrier density and effective diffusion coefficient.

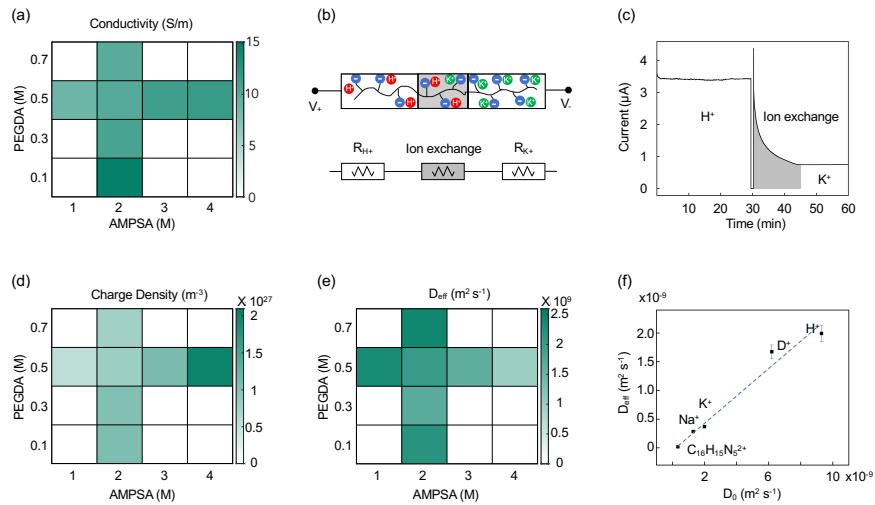


Figure 31 (a) Ionic conductivity of hydrogels as a function of AMPSA and PEGDA content. With more AMPSA and less PEGDA, hydrogels exhibit higher conductivity. (b) Schematic of charge carrier density measurement using the ion exchange process. (c) Current response when we change the charge carrier from  $H^+$  to  $K^+$ . During the ion exchange process, the current under the gray area is integrated and leads to the charge carrier density. (d) Charge carrier density of the hydrogels as a function of AMPSA and PEGDA. The charge carrier density increases with AMPSA content

because AMPSA directly provides charged sites, and slightly decreases with more PEGDA. (e) Effective diffusion coefficient ( $D_{eff}$ ) of the hydrogels as a function of AMPSA and PEGDA. The  $D_{eff}$  decreases with more AMPSA and shows no obvious trend while changing PEGDA. (f) Relationship between effective diffusion coefficient ( $D_{eff}$ ) and bulk diffusion coefficient ( $D_0$ ) of  $Na^+$ ,  $K^+$ ,  $H^+$ ,  $D^+$ , DAPI in AP/2/0.5 hydrogel.

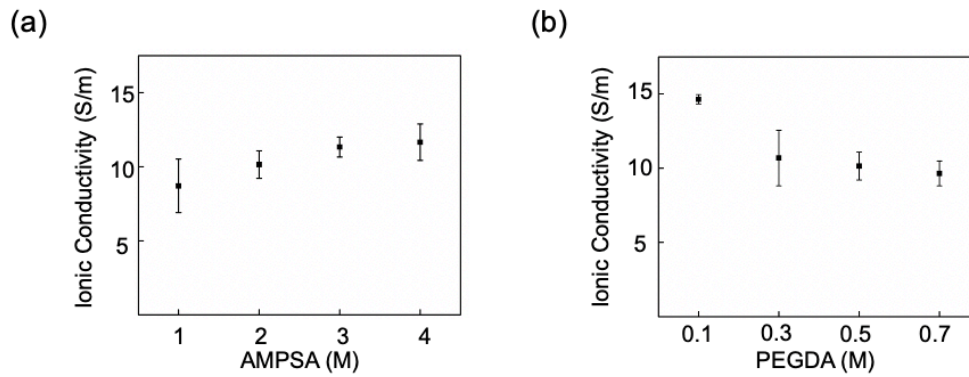


Figure 32. Dependence of ionic conductivity on AMPSA and PEGDA.

Assuming that the hydrogel is electroneutral, the mobile charge carrier density ( $n$ ) in the hydrogel equals to the fixed charge density of the polymeric network.<sup>109</sup> Here, we measure the fixed charge density of the polyelectrolyte hydrogel using an ion exchange process with the same experiment setup in the ionic conductivity measurement (Figure 28 b). First, we use 100 mM HCl as the electrolyte, apply 0.8 V and measure the currents. When all the charged groups in the polyelectrolyte

hydrogels are compensated with  $H^+$ , the resistance of the ionic conductor is stable and the current reaches an equilibrium. Second, we change the electrolyte to 100 mM KCl. The counter ions  $H^+$ , at the fixed charge sites, are gradually exchanged by  $K^+$ , which has lower mobility and therefore the current decreased. When all the  $H^+$  are replaced by  $K^+$ , the resistance of the ionic conductor is only dependent on  $K^+$ , and the current became steady again. Here we assume the total number of fixed charges equals to the transferred ionic charges between the two steady states, which can be estimated by integrating the electronic current with time (Figure 30c).

The hydrogel glass fiber has a precisely defined geometry, so we can easily have an estimate of the mobile charge density in each hydrogel by dividing the number of charges by the hydrogel volume. Figure 31d shows that the charge density increases with higher AMPSA and less PEGDA. In Figure 33, the charge carrier density increases from  $5.6 \pm 0.2 \times 10^{26} \text{ m}^{-3}$  to  $1.6 \pm 0.5 \times 10^{27} \text{ m}^{-3}$  when we increase AMPSA from 1 M to 4 M, which is more significant than that of hydrogels with different PEGDA, from  $1.1 \pm 0.1 \times 10^{27} \text{ m}^{-3}$  to  $7.7 \pm 0.1 \times 10^{26} \text{ m}^{-3}$ . This is because AMPSA provides ionized sulfonate groups directly. Even PEGDA doesn't directly supply fixed charges, its influence on the crosslinking density changes the charge carrier density in a moderate manner.

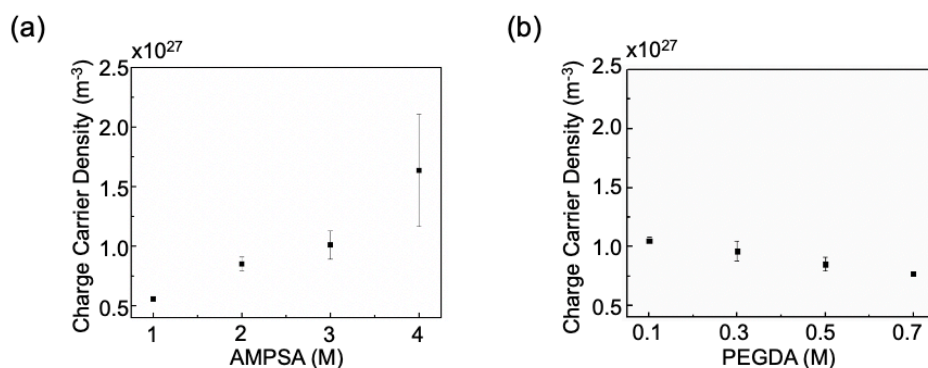


Figure 33 Dependence of charge carrier density on AMPSA and PEGDA ratio.

Then, we calculated the effective diffusion coefficient of  $H^+$  in each hydrogel with the ionic conductivity and charge carrier density (Figure 34), which shows that the  $D_{\text{eff}}$  decreases with higher AMPSA, from  $2.5 \pm 0.5 \times 10^{-9} \text{ m}^2\text{s}^{-1}$  to  $1.1 \pm 0.4 \times 10^{-9} \text{ m}^2\text{s}^{-1}$ , which are in the same magnitude of what reported so far.<sup>241</sup> However,  $D_{\text{eff}}$  does not show monotonical change when we change PEGDA. The reason could be that effective diffusion coefficient is affected by more complicated factors.

Here we consider  $D_{\text{eff}}$  as a description of the hinderance of hydrogel microstructure on the ion transport, and measured the ionic conductivity and  $D_{\text{eff}}$  of different ions and small molecules using AP/2/0.5 hydrogel. By changing the electrolyte that supplies ions to the hydrogel as the charge carrier, we measured the ionic conductivity and calculated the  $D_{\text{eff}}$  of different ions and ionic species ( $H^+$ ,  $D^+$ ,  $Na^+$ ,  $K^+$ , and  $C_{16}H_{12}N_5^{2+}$ ) in the AP/2/0.5 hydrogel (Figure 31f). The results of  $H^+$  and  $K^+$  are almost the same as what reported by Simon and co-workers.<sup>32</sup> In Figure 31f, we plotted the relationship of  $D_{\text{eff}}$  and the diffusion coefficient in bulk solution,  $D_0$ . The linear relationship ( $R^2 = 0.98$ ) indicates that the effect of the hydrogel microstructure

on the ion and ionic species transport is a property of the hydrogel itself and it is generalizable in this transport regime in which we assume that the size of the ionic species is much smaller than the pore size of the hydrogel.

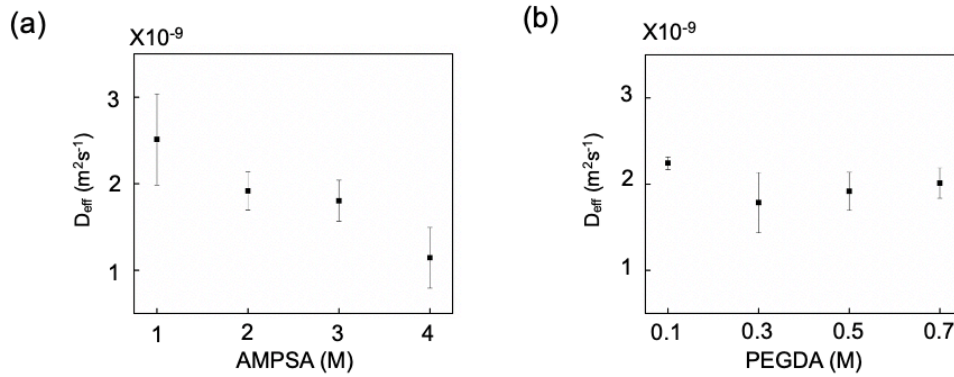


Figure 34 Dependence of effective diffusion coefficient ( $D_{eff}$ ) on AMPSA and PEGDA.

Table 4 Electrical Properties of hydrogel

	Conductivity (S/m)	Charge Carrier Density (/m <sup>3</sup> )	Mobility (m <sup>2</sup> /V·s)	Effective Diffusion coefficient ( $D_{eff}$ ) (m <sup>2</sup> /s)
AP/1/0.5	$8.7 \pm 1.8$	$5.6 \pm 0.2 \times 10^{23}$	$9.8 \pm 2.0 \times 10^{-8}$	$2.5 \pm 0.5 \times 10^{-9}$
AP/2/0.5	$10.1 \pm 0.9$	$8.5 \pm 0.6 \times 10^{23}$	$7.5 \pm 0.9 \times 10^{-8}$	$1.9 \pm 0.2 \times 10^{-9}$
AP/3/0.5	$11.3 \pm 0.7$	$1.0 \pm 0.1 \times 10^{24}$	$7.0 \pm 0.9 \times 10^{-8}$	$1.8 \pm 0.2 \times 10^{-9}$
AP/4/0.5	$11.6 \pm 1.2$	$1.6 \pm 0.5 \times 10^{24}$	$4.4 \pm 1.4 \times 10^{-8}$	$1.1 \pm 0.4 \times 10^{-9}$
AP/2/0.1	$14.7 \pm 0.3$	$1.1 \pm 0.1 \times 10^{24}$	$8.7 \pm 0.3 \times 10^{-8}$	$2.2 \pm 0.1 \times 10^{-9}$
AP/2/0.3	$10.7 \pm 1.9$	$9.6 \pm 0.8 \times 10^{23}$	$6.9 \pm 1.4 \times 10^{-8}$	$1.8 \pm 0.3 \times 10^{-9}$
AP/2/0.5	$10.1 \pm 0.9$	$8.5 \pm 0.6 \times 10^{23}$	$7.5 \pm 0.9 \times 10^{-8}$	$1.9 \pm 0.2 \times 10^{-9}$



AP/2/0.7	$9.7 \pm 0.8$	$7.7 \pm 0.1 \times 10^{23}$	$7.8 \pm 0.7 \times 10^{-8}$	$2.0 \pm 0.2 \times 10^{-9}$
----------	---------------	------------------------------	------------------------------	------------------------------

*Table 5 The electrical properties of AP/2/0.5 with different ions as the charge carriers.*

<b>Charge Carrier</b>	<b><math>D_0</math> (m<sup>2</sup>/s)</b>	<b><math>D_{\text{eff}}</math> (m<sup>2</sup>/s)</b>
H <sup>+</sup>	$9.30 \times 10^{-9}$	$2.0 \pm 0.1 \times 10^{-9}$
D <sup>+</sup>	$6.20 \times 10^{-9}$	$1.7 \pm 0.1 \times 10^{-9}$
K <sup>+</sup>	$2.00 \times 10^{-9}$	$3.7 \pm 0.3 \times 10^{-10}$
Na <sup>+</sup>	$1.30 \times 10^{-9}$	$2.8 \pm 0.2 \times 10^{-10}$
C <sub>16</sub> H <sub>15</sub> N <sub>5</sub> <sup>2+</sup>	$3.40 \times 10^{-10}$	$1.8 \pm 0.6 \times 10^{-11}$

To gain further insights, we characterize the hydrogel microstructure as a function of composition and relate the microstructure to  $D_{\text{eff}}$ . When a hydrogel is brought into contact with water, water diffuses into the pre-existing or dynamically formed spaces between hydrogel chains due to the osmotic pressure.<sup>236</sup> The polymeric network expands and results in swelling of the hydrogel, which involves larger segmental motion and ultimately increased separation between hydrogel chains.<sup>242</sup> The swelling capability is important for applications such as drug delivery and ion-based bioelectronics. However, when we integrate hydrogels with bioelectronic devices, excessive swelling behavior damages the device. Thus, understanding the mechanism

of hydrogel swelling and methods to regulate this property is of great significance for their integration with the bioelectronic devices.

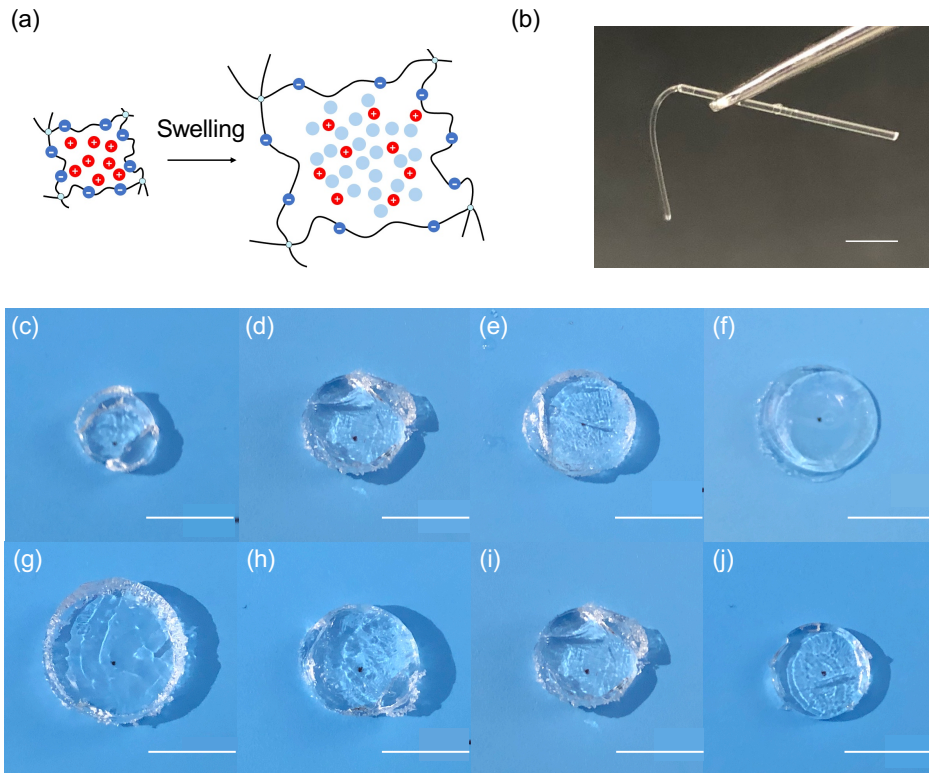


*Figure 35 (a) Schematic of water diffusing into the hydrogel due to osmotic pressure, which results in swelling of the hydrogel and enlarged pores. (b) Hydrogel swells in the glass capillary fiber. Scale bar: 2 mm. Optical images of swollen (c) AP/1/0.5, (d) AP/2/0.5, (e) AP/3/0.5, (f) AP/4/0.5, (g) AP/2/0.1, (h) AP/2/0.3, (i) AP/2/0.5, (j) AP/2/0.7 hydrogels.*

We soaked all the hydrogels in excessive DI water for 48 hrs to reach equilibrium before taking the pictures in Figure (c-j). When we increase AMPSA from 1 M to 4

M, hydrogel swelling ratio increases from  $268 \pm 16 \%$  to  $331 \pm 20 \%$ . This is mainly because the increase of the counterions inside the hydrogel, which increases the osmotic pressure that swells the hydrogel.<sup>243</sup> On the other hand, when we increase the crosslinker from 0.1 M to 0.7 M, the swelling ratio is dramatically reduced from  $1418 \pm 153 \%$  to  $242 \pm 1 \%$ . The crosslinker has a major effect on the polymer chains branching and network. Thus, the network space is decreased with higher crosslinker and less water enters the hydrogel. This result is similar with the study from Patel and co-workers on superporous hydrogels.<sup>244</sup>

To gather further understanding, we conducted SEM characterization to determine the morphology of the polymeric network and understand the average pore size of all the hydrogels. In Figure 35(a-d), all hydrogels except AP/1/0.5 present well-defined pores with average size ranging from  $12 \pm 7 \text{ um}^2$  to  $802 \pm 94 \text{ um}^2$ . AP/1/0.5 seems to have a structure with few pores, which aligns well with its relatively lower swelling ratio. The nonporous structure reduces water absorption and therefore ion transport, but nonporous hydrogels are good candidates for applications that require low swelling ratio or good mechanical properties.<sup>245</sup> AP/2/0.5, AP/3/0.5, and AP/4/0.5 hydrogels are similar in the average pore sizes,  $39 \pm 82 \text{ um}^2$ ,  $54 \pm 33 \text{ um}^2$ , and  $33 \pm 27 \text{ um}^2$ , respectively. In comparison, when PEGDA is increased from 0.1 M to 0.7 M, the average pore sizes of hydrogels show significant decrease:  $802 \pm 93 \text{ um}^2$ ,  $275 \pm 121 \text{ um}^2$ ,  $39 \pm 18 \text{ um}^2$ ,  $13 \pm 7 \text{ um}^2$ , as shown in Figure 35 (e-h).

Diffusion coefficient ( $D_{eff}$ ) is dependent on the porosity ( $\varepsilon$ ) and tortuosity ( $\tau$ ) of the porous media (Equation 16).<sup>246</sup> Here we use Eq 6 to correlate the microstructure and the ionic conductivity.

$$D_{eff} = \frac{\varepsilon}{\tau} D_0 \text{ Equation 16}$$

where  $D_0$  is the diffusion coefficient of  $H^+$  in bulk solution ( $9.31 \times 10^{-9} \text{ m}^2/\text{s}$ ).  $\varepsilon$  is the porosity and  $\tau$  is the tortuosity.

First, we characterize the porosity of hydrogels, which is defined as the ratio of the pores' volume and the total volume of the hydrogel (Equation 17).

$$\varepsilon = \frac{V_{pore}}{V_{total}} \text{ Equation 17}$$

In Figure 35j, when we increase the AMPSA from 1 M to 3 M, the porosity increases from  $0.39 \pm 0.04$  to  $0.56 \pm 0.02$  because the higher osmotic pressure.<sup>236</sup> The porosity doesn't further increase and even decrease to  $0.52 \pm 0.02$  when we increase the AMPSA to 4 M, which might be due to the ion pair formation from the high ionic group contents.<sup>236</sup> In comparison, the porosity decreases from  $0.74 \pm 0.02$  to  $0.48 \pm 0.01$  when we increased the PEGDA from 0.1 M to 0.5 M because of the higher polymeric network density (Figure 35k). However, the porosity doesn't further decrease when we increase the AMPSA to 0.7 M because of the finite shrinkage of the network chains. Apparently, the influence of PEGDA on the porosity is more

significant than APMSA, and these results match well with the SEM images and swelling behaviors.

Various definition and measurements of tortuosity have been reported from the perspective of engineers geologists and chemists,<sup>246, 247</sup> but rarely studied for hydrogels. In fact, hydrogels with low tortuosity is desired for supercapacitors<sup>248</sup> and ion-based bioelectronic devices, so the investigation on the hydrogel tortuosity is in demand. Figure 36i shows the definition of tortuosity: the ratio of the actual distance that ions travel between two points by following the microchannel of the hydrogel to the straight-line distance between the two points (Equation 18).

$$\tau = \frac{L}{x} \text{ Equation 18}$$

A material with perfectly straight pores will have a tortuosity of 1.<sup>249</sup> Here we extracted the tortuosity from  $D_{\text{eff}}$  and  $\varepsilon$ , according to Equation 17. show the tortuosity increases with higher AMPSA, from  $1.44 \pm 0.34$  to  $4.31 \pm 1.33$ , which could be attributed to the increased fixed charge sites that dictate the path ion movement.<sup>250</sup> Figure 36n shows that the tortuosity decreases with more PEGDA, from  $3.08 \pm 0.14$  to  $2.21 \pm 0.23$ , because of the higher network density. Thus, the charged monomer influences the tortuosity more than the crosslinker in polyelectrolyte hydrogels.

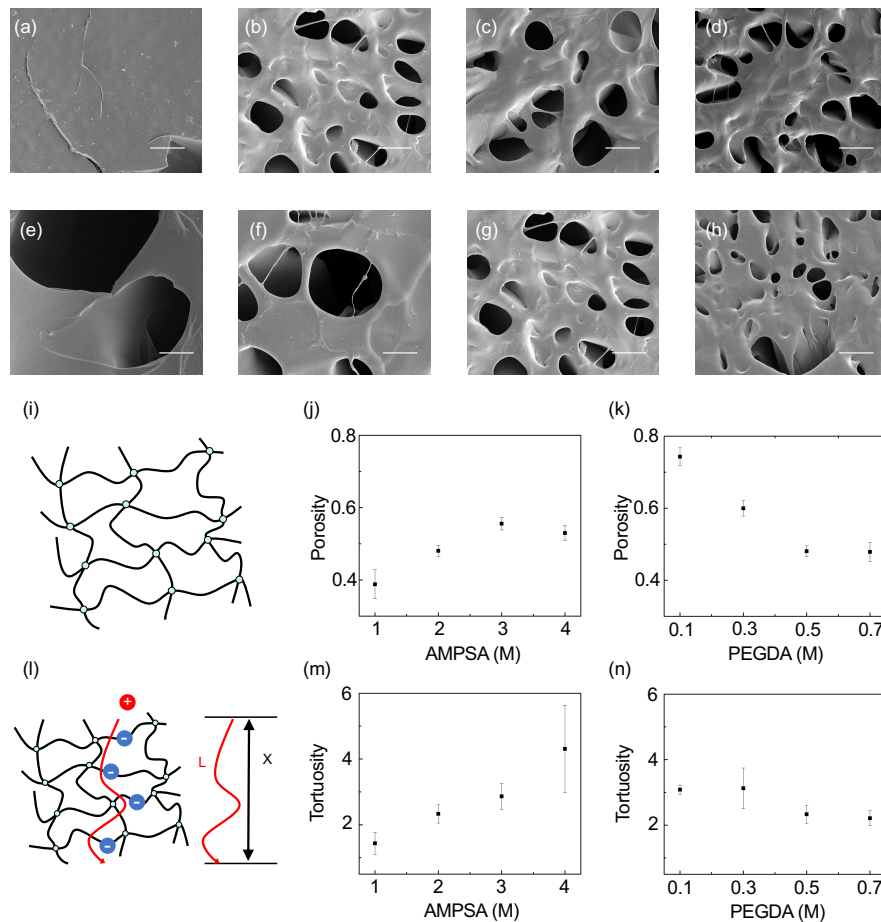
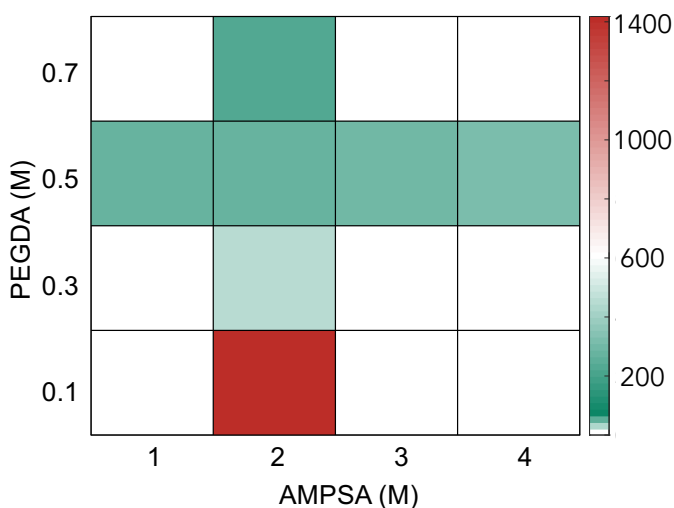


Figure 36 SEM of hydrogels: (a) AP/1/0.5, (b) AP/2/0.5, (c) AP/3/0.5, (d) AP/4/0.5, (e) AP/2/0.1, (f) AP/2/0.3, (j) AP/2/0.5, (h) AP/2/0.7 hydrogels. Scale bar: 10  $\mu\text{m}$ . (i) Schematic of porosity. (j) Porosity change while changing AMPSA. (k) Porosity change while changing PEGDA. (l) Schematic of tortuosity. (m) Tortuosity change while changing AMPSA. (n) Tortuosity change while changing PEGDA.

Table 6 Microstructure properties of the hydrogels.

	<b>Swelling Ratio (%)</b>	<b>Porosity</b>	<b>Tortuosity</b>
AP/1/0.5	268 ± 16	0.39 ± 0.04	1.44 ± 0.34
AP/2/0.5	285 ± 5	0.48 ± 0.01	2.33 ± 0.28
AP/3/0.5	298 ± 2	0.56 ± 0.02	2.87 ± 0.39
AP/4/0.5	331 ± 20	0.53 ± 0.02	4.31 ± 1.33
AP/2/0.1	1418 ± 153	0.74 ± 0.02	3.08 ± 0.14
AP/2/0.3	454 ± 12	0.60 ± 0.02	3.12 ± 0.62
AP/2/0.5	285 ± 5	0.48 ± 0.01	2.33 ± 0.28
AP/2/0.7	242 ± 1	0.48 ± 0.03	2.21 ± 0.23



*Figure 37 Swelling ratio of hydrogels as a function of AMPSA and PEGDA.*

### 5.3 Conclusion

In summary, we presented a comprehensive study on the electrical properties (the ionic conductivity, charge carrier density, and effective diffusion coefficient) and

microstructure (swelling ratio, porosity, and tortuosity) of a series of polyelectrolyte hydrogel. We found that more AMPSA monomer results in higher ionic conductivity due to higher charge carriers directly compensated by sulfonate groups. The charge carriers also influence the hydrogel microstructure by altering the osmotic pressure between the polymeric network and the environment, and therefore the swelling ratios. By further analyzing the hydrogel microstructure by SEM, porosity, and tortuosity, we found that the AMPSA can increase porosity and tortuosity of the hydrogels, but shows negligible influence on the pore size. However, the excessive hydrogel swelling from high AMPSA has the risk of device failure when the hydrogel is integrated in bioelectronic devices. On the other hand, we found that increasing PEGDA content crosslinker can reduce the amount of swelling by increasing the crosslinking density. The relationship between effective diffusion coefficient and porosity and tortuosity correlates the ionic conductivity and microstructure of hydrogels, which can be applied to other ions and even small charged molecules. By tuning the monomer and crosslinker, we provide a strategy to regulate the ionic conductivity and microstructure of the AMPSA/PEGDA hydrogels that could also be extended to other polyelectrolyte hydrogels and will enable applications of such materials in bioelectronic devices to control ionic signals directly.

#### 5.4 Experiments section

*Hydrogel capillary fibers fabrication:* AMPSA, PEGDA, and photo-initiator are mixed in water at room temperature following the protocols in Table S1. The



hydrogel solution was injected into the glass capillary fiber and exposed under UV light (power: 8 mW / cm<sup>2</sup>, wavelength 306 nm) to finalize the ionic resistor fabrication.

*Ionic conductivity measurement:* All electrical measurements were performed using a computer controlled Autolab potentiostat with analytic software Nova 2.0. PDMS with punched holes is used as the substrate to make two isolated electrolytes connected by the hydrogel glass fiber. Home-made AgCl wires are immersed in the electrolyte as the electrode contact.

*Swelling ratio measurement:* First, we crosslinked 100 ul hydrogel solution in PDMS well (8 mm diameter) with UV exposure. Then, we placed each hydrogel sample in excessive distilled water at room temperature for 48 hours to reach the equilibrium. The weight of the swollen hydrogel was recorded as  $W_{wet}$ . Then we dried the hydrogel samples immediately using lyophilizer and recorded the weight of the dried hydrogel as  $W_{dry}$ . The swelling ratio is calculated by the following equation:

$$swelling\ ratio = \frac{W_{wet} - W_{dry}}{W_{wet}}$$

*Porosity measurement:* By substituting  $W_{wet}$  by  $W_{dry}$ , we got the weight of the water in all the hydrogel pores and therefore the volumes of the pores,  $V_{pore}$ . By dividing  $V_{pore}$  by the total volume of the hydrogel,  $100\text{ ul} + V_{pore}$ , we calculated the porosity of

each hydrogel. To achieve good precision, we measured 3 samples for each hydrogel in each measurement and took the average of the results.

*SEM:* First, we crosslinked 100 ul hydrogel solution in PDMS well under UV exposure. Then, we placed each hydrogel sample in an excess of water at room temperature for 48 hours in order to reach the equilibrium. Right after this, we froze the sample by liquid nitrogen and left them in the lyophilizer for another 48 hours. The samples were sputtered with ~20nm of Au-Pd prior to imaging to prevent charging. We used a FEI Quanta 3D Dualbeam microscope operated with the electron beam at 5kV.

*Materials:* All the chemicals used are purchased from Sigma Aldrich and used without further modification unless specifically mentioned. Glass capillary fibers (I.D. = 50 um, O.D. = 350 um) are purchased from Molex. Silver chloride wires are made in house by chlorinating the silver wire with 100 mM KCl solution.

## 6. Electrophoretic Delivery of ions and biomolecules with bioelectronic devices

### 6.1 Delivery of Acetylcholine by polyelectrolyte hydrogel

The porous structure of hydrogels enables the delivery of not only ions, but also biomolecules with larger size. Here is an example of ion pumps that use hydrogels as the ion exchange materials to deliver neurotransmitter, acetylcholine.

In conventional ion pump with horizontal geometry (Figure 38), the reservoir and target are connected by an ion exchange membrane from left to right, and SU8 microfluidic channels are used to isolate the two electrolytes and microfluidic tape are used to seal the channel, which causes bubbles in the microfluidic channel and subsequent device failure and cell death in long term experiments.

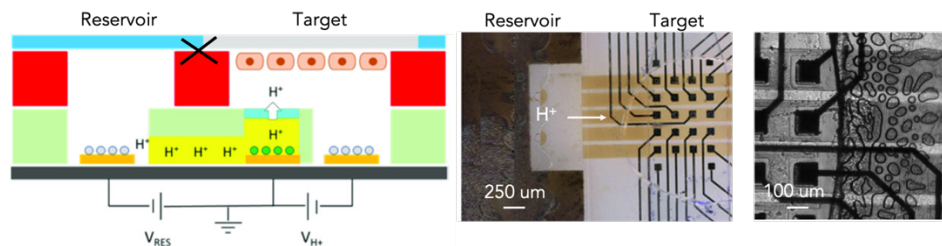


*Figure 38 Horizontal ion pump.*

Figure 39 shows the schematic of the vertical ion pump, in which the reservoir and target are connected by hydrogels from down to top. Thus, the reservoir and target are much far from each other and we don't need microfluidic tape to seal the channel. In comparison to the fabrication of ion exchange membrane by spin coating and photolithography in the horizontal ion pumps, the integration of hydrogels with the

SU8 microfluidic channels are more challenging. First we use a water soluble tape to seal the SU8 opening in the target chamber; then we inject the hydrogel precursor solution made from 2-Acrylamido-2-methyl-1- propanesulfonic acid (AMPSA) crosslinker by Poly (ethylene glycol) diacrylate (PEGDA) in the SU8 microfluidic channel and use UV to crosslink the solution into hydrogel; finally we remove the water soluble tape by dissolving the tape using water.



*Figure 39 Fabrication of hydrogel in the vertical ion pump.*

The bonding between the SU8 channel and the hydrogel is problematic. Hydrogel came out of the SU8 channels of the ion pump while swelling if there is no surface treatment on the SU8 channel to bind them together (Figure 40).

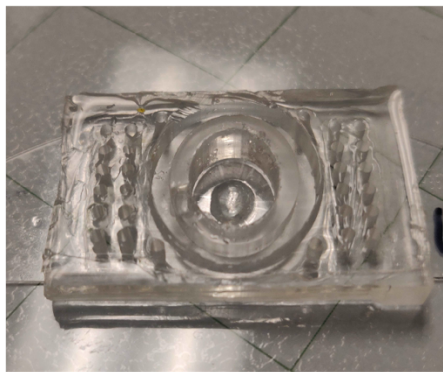


Figure 40 Hydrogel swell out of the SU8 microfluidic channels into the target chamber when there is no silane treatment.

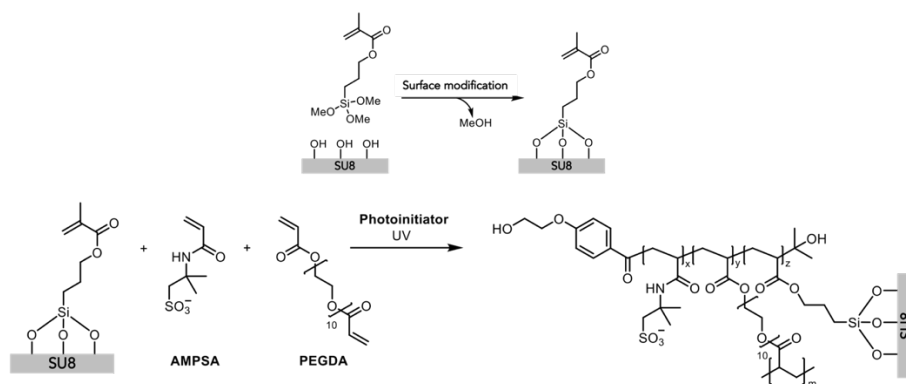
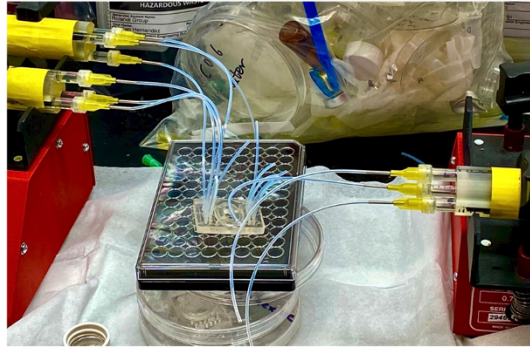


Figure 41 Reactions of SU8 surface treatment and hydrogel binding.

First we used the same protocol that we treated glass capillary fiber as we shown above: flow 10 wt% A174 in toluene in all 9 SU8 channels by syringe pump (Figure 42). It works but brings new risks to the device in this process: (1) PDMS swells in toluene and causes detachment of PDMS and SU8 substrate; (2) the microfluidic tubings used to inject the solution have the risk to destroy the bonding of PDMS and SU8; (3) The water soluble tape used to seal the SU8 opening temporarily will lose effect with time and the contact with the solvent.



*Figure 42 SU8 surface treatment by A174 in toluene.*

To optimize this process, we used chemical vapor deposition (CVD) to deposit A174 monomer. In detail, we activate the surface of SU8 channels by O<sub>2</sub> plasma as usual, and then put the devices in the CVD chamber with A174 at 85C for 3 hours. By doing so, we avoided using any polar solvent that may affect the PDMS, and the mechanical risk induced by plugging microfluidic tubings in and out of the device. Additionally, we can do surface treatment on more than 10 devices at once, which significantly increases the fabrication efficiency.

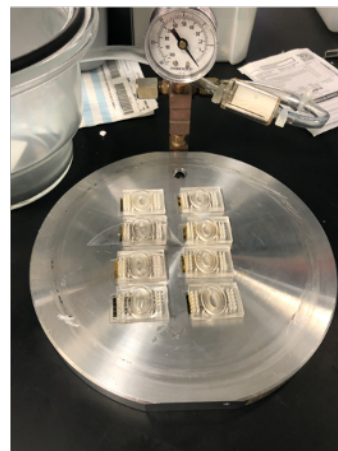


*Figure 43 SU8 surface treatment by A174 vapor in CVD.*

Figure 44 shows the devices filled with hydrogels, whose channels are treated with A174 vapor and the hydrogels are kept in the channel without slipping out.



*Figure 44 Devices with SU8 surface treatment.*

The second challenge of integrating hydrogels in the device is that hydrogels naturally absorb large amount of water and swell in aqueous environment, which break the SU8 microfluidic channels. Figure 45 shows that after the successful surface treatment of SU8 channel, the hydrogels are kept in the SU8 channels instead of slipping out from the SU8 openings. However, the hydrogel swells within the channels and breaks the channels.



*Figure 45 Hydrogels that swell too much break SU8 channels.*

I optimized the protocol of hydrogels to reduce the swelling behavior while maintaining the ionic conductivity by tuning the ratio of monomer, AMPSA, and crosslinker, PEGDA, according to the research shown in the previous section.

The porous hydrogel structure enables the delivery of large biomolecules. As a proof-of-concept, we delivered acetylcholine using this ion pump.

Acetylcholine, as a typical biomolecule, is the primary neurotransmitter of the parasympathetic nervous systems in the brain and body of many types of animals (including human) and shown to markedly stimulate the proliferation of cells (Figure 46). Because of the acetylation at the oxygen atom, acetylcholine possesses a highly polar, charged ammonium group preventing penetrating lipid membranes. Herein, we use acetylcholine as the first choice of biochemical signal to increase cell innervation.



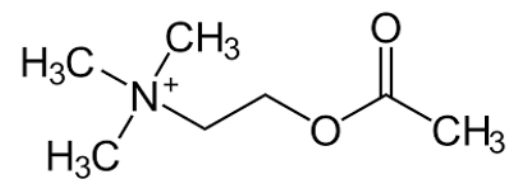


*Figure 46 Molecules structure of acetylcholine.*

We delivered Acetylcholine from reservoir (100mM Acetylcholine chloride (AchCl)) to the target and measured the Ach<sup>+</sup> by Amplex Red Acetylcholine/Acetylcholinesterase Assay Kit (ThermoFisher, A12217).

The Amplex Red Acetylcholine/Acetylcholinesterase Assay kit, providing an ultrasensitive method, supports operators to detect acetylcholine (Ach) in a fluorescence microplate reader (we used 96 wells plate here) or fluorometer. In this facile assay, acetylcholine is converted to choline under the action of acetylcholinesterase initially. Choline oxidase oxidizes choline to oxides consisting of betaine and H<sub>2</sub>O<sub>2</sub>, the latter of which, reacts with 10-acetyl-3, 7-dihydroxyphenoxazine (Amplex Red reagent) in a 1:1 stoichiometry to generate the highly fluorescent product resorufin, in the presence of horseradish peroxidase. This kit is amenable for detecting acetylcholine level with a range of detection from 0.3  $\mu$ M to 100  $\mu$ M (Figure 47). After reaction was incubated at room temperature, the quantity of fluorescence product was measured with a fluorescence microplate reader.

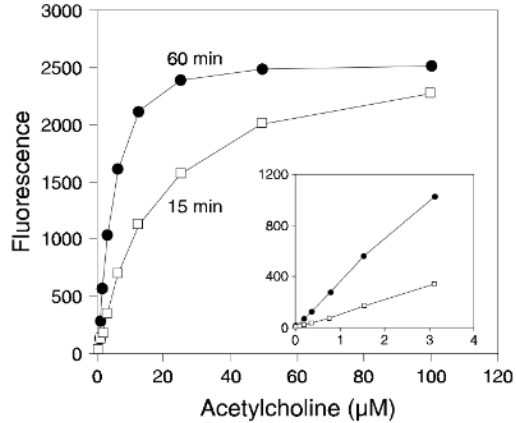


*Figure 47 Detection of acetylcholine. 200 µM Amplex Red reagent, 0.1 U/mL choline oxidase, 0.5 U/mL acetylcholinesterase, 1U/mL HRP and the indicated amount of acetylcholine in 1X Reaction Buffer are contained in each reaction at ambient temperature. After approximately 30 mins, the measurement of fluorescence detection at  $590 \pm 10$  nm was determined by a fluorescence microplate reader.*

Figure 48a shows the photo of the device and experimental setup for Ach<sup>+</sup> delivery. AgCl glass electrode and AgCl wire electrode contacts are cathode and anode and immersed in the target and reservoir electrolytes to close the circuit. 100 mM AchCl was delivered to target solution (1x buffer) and the Ach in the target solution was collected and measured by ELISA kit.

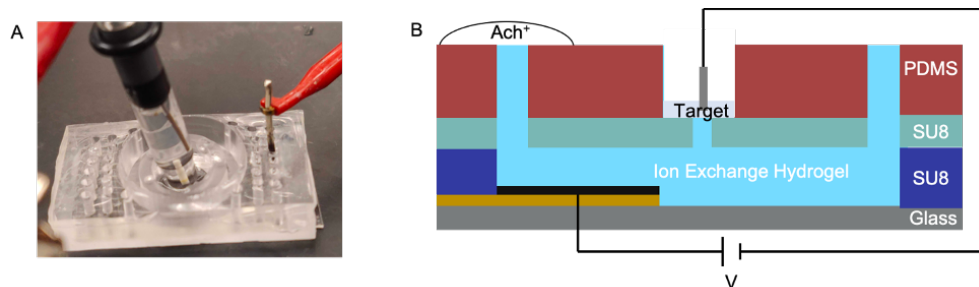
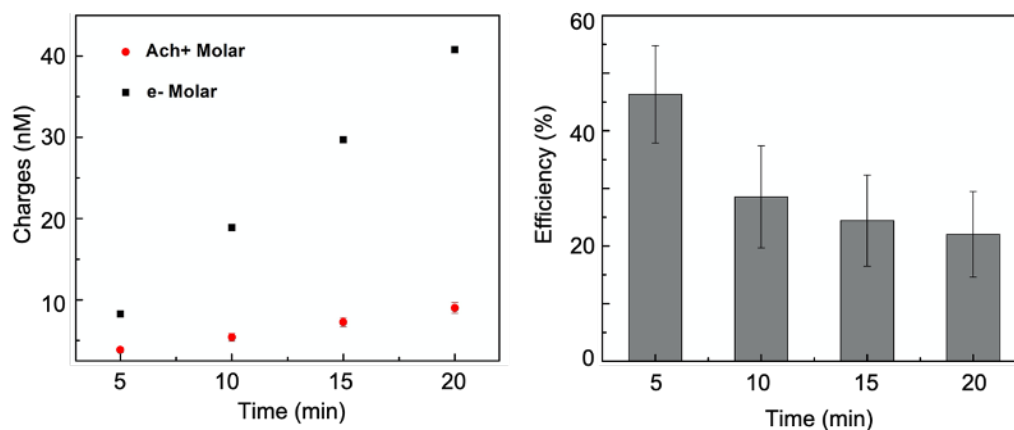


Figure 48 Photo of experimental setup for Ach<sup>+</sup> delivery of device, AgCl glass electrode and AgCl wire electrode contact are cathode and anode and immersed in two solutions, respectively; (B): Schematics of experimental setup. Target solution was 1x buffer with 300  $\mu$ L and the reservoir was 100 mM Acetylcholine chloride.

While the device is run for 20 min continuously, we collected 150  $\mu$ L solution every 5 mins and added equivalent amount of buffer to the target. ELISA kit converted acetylcholine chloride to H<sub>2</sub>O<sub>2</sub> reacting with Amplex red reagent and generated fluorescent product resorufin. We tested two devices with a total of three channels successfully and the results are shown below:



*Figure 49 The experimental result of channel 1 in device 1. According to the diagram, short running time is preferable with a high efficiency (~50 %).*

For the channel 1 of device 1, the current was  $2.6 \mu\text{A}$  and the measured  $\text{Ach}^+$  concentration of target solution was  $1.4 \pm 0.3 \text{ mM}$ . *Figure 49* shows that the delivered  $\text{Ach}^+$  at 5 min, 10 min, 15 min, and 20 min, as well as the measured electrical charges in the circuit at each time point. By dividing the delivered  $\text{Ach}^+$  by the delivered  $e^-$ , we got the efficiency at different time,  $50 \pm 10 \%$ .

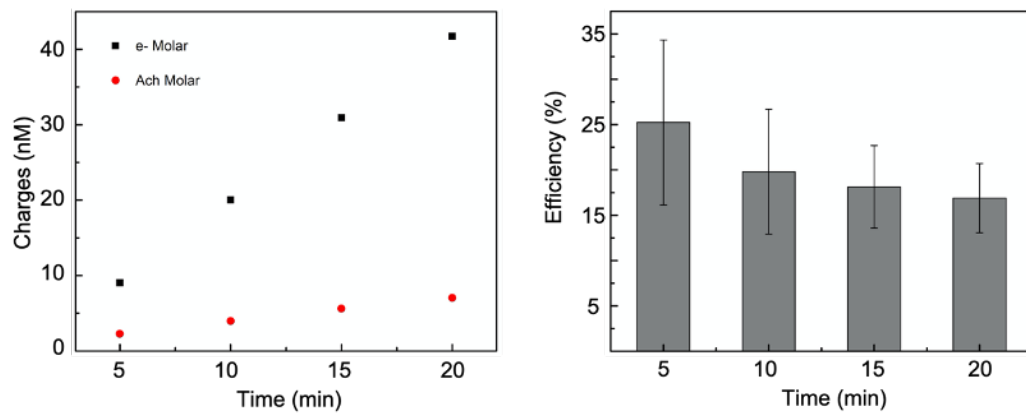


*Figure 50 The experimental result of channel 2 in device 1. The diagram also shows that longer running time will result in low efficiency because of the depletion zone in the reservoir.*

As for the channel 2 of device 1 (*Figure 50*), the current achieved  $2.9 \mu\text{A}$  and the delivered concentration was  $0.9 \pm 0.3 \text{ mM}$ . The efficiency is about  $30 \pm 10\%$ .

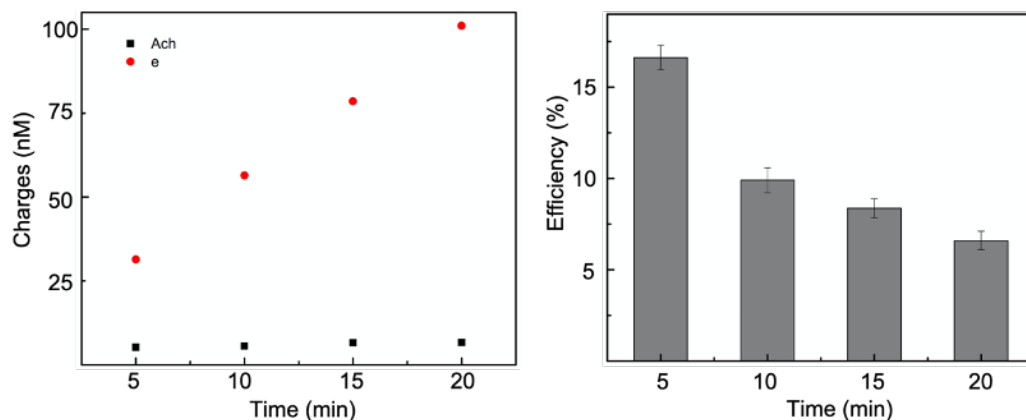
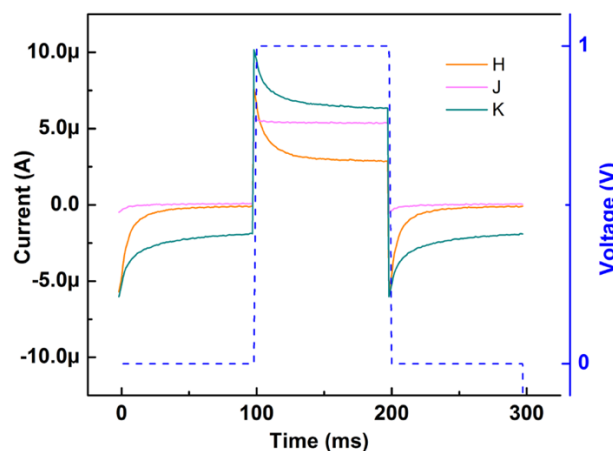


Figure 51 The experimental result of channel 1 in device 2.

The current of channel 1 in device 2 was high ( $13.5 \mu\text{A}$ ) but the delivered  $\text{Ach}^+$  doesn't increase significantly,  $2.4 \pm 0.3 \text{ mM}$ . The calculated efficiency is only  $17 \pm 2\%$ . The reason could be that more side reactions, such as water splitting, happened and reduced the delivery efficiency. Thus, higher voltage, higher current may not improve the actual delivery amount. Additionally, we noticed that the delivery efficiency decreased with time, which is due to the exhausted area in the reservoir. Short time is preferable, which can be achieved by pause signals.



*Figure 52 Current data of three devices within 100 ms.*

Figure 52 shows that the currents when we applied 1 V for 100 ms, and pulsed for 100 ms. By repeating the experiment for 100 cycles, we were able to collect the target solution and measure the Ach<sup>+</sup> concentration (Table 7). The efficiency is generally higher than that of the continuous delivery.

*Table 7 Ach<sup>+</sup> delivery*

Device	Delivered charge (C)	Delivered Ach <sup>+</sup> in total (M)	Efficiency (%)	Delivered e <sup>-</sup> in 100 ms (C)	Delivered Ach <sup>+</sup> in 100 ms in 1 nL (mM)
1	4.3E-4	2.6E-9	58.4	3.9E-7 ± 1.6E-9	3.1 ± 0.01
2	2.3E-4	1.8E-9	77	4.5E-7 ± 5.7E-9	3.6 ± 0.05
3	7.4E-5	2.2E-10	28	1.43E-7 ± 1.40E-7	0.42 ± 0.41

Furthermore, we validated the experimental results by modelling the experiment via Comsol software.

COMSOL physics modeling of the system was used to verify the experimental results. For the initial condition, we took the delivered Ach<sup>+</sup> in 100 ms of Device 3, which is the lowest value among all three devices and other devices all exhibit better performance. Here we assumed that the diffusion is dominant in the system, which is expected because the voltage drop occurs primarily across the hydrogel channel. A 1mm x 1mm x 0.1mm volume describes the area in the cell-culture microfluidic immediately around the array. Figure 53A shows the Ach<sup>+</sup> change over the pore opening after 100 ms delivery, which shows a high-resolution pH gradient around the ion pump pore.

The FWHM of the Ach<sup>+</sup> distribution was examined at 100ms of Ach<sup>+</sup> pumping to examine the spatiotemporal resolution of the pump (Figure 53B, C). The Ach<sup>+</sup> observed at the pore opening with a 100ms pulse at the distance of 10  $\mu\text{m}$  Ach<sup>+</sup> is 2.5 mM with a FWHM of 38.8  $\mu\text{m}$  after 100 ms. As the Ach<sup>+</sup> diffuse out from the pump pore, they expand in a semi-circle. This means that at different heights from the pump pore, the FWHM will have different values. Since, on this in-vitro chip cells will be cultured at the top of the channel, it makes sense to look at the FWHM at 40-100 $\mu\text{m}$  vertically from the pore. With this in mind, we predict a 100 $\mu\text{m}$  FWHM pulse is achievable by operating the pump for 100 ms with the device.

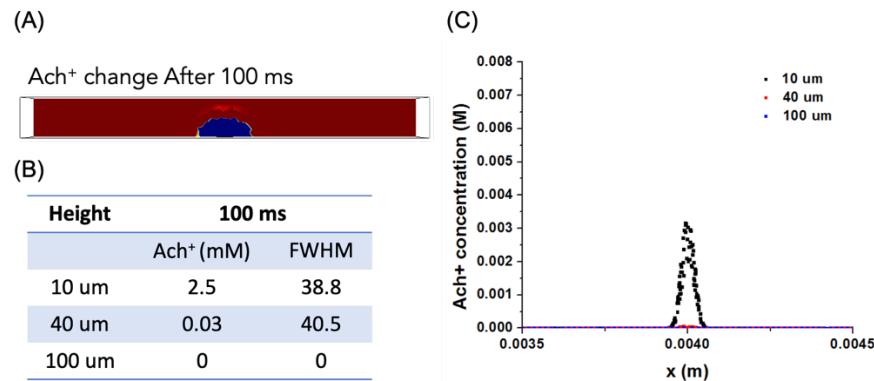


Figure 53 (A) COMSOL model of Ach<sup>+</sup> concentration after 100ms of Ach<sup>+</sup> injection.

(B, C) FWHM at different heights above the ion pump pore from COMSOL model.

## 6.2 Chloride pump

Translation between ionic currents and measurable electronic signals is essential for the integration of natural system and artificial bioelectronic devices. Chloride ions ( $\text{Cl}^-$ ) play a pivotal role in bioelectricity, and they are involved in several brain pathologies, including epilepsy and disorders of the autistic spectra, as well as cancer and birth defects. As such, controlling  $[\text{Cl}^-]$  in solution can actively influence biochemical processes and can be used in bioelectronic therapies. Here, we demonstrate a bioelectronic device that uses Ag/AgCl contacts to control  $[\text{Cl}^-]$  in solution by electronic means. We do so by exploiting the potential dependence of the reversible reaction,  $\text{Ag} + \text{Cl}^- \leftrightarrow \text{AgCl} + \text{e}^-$ , at the contact/solution interface, which is at the basis of the well-known Ag/AgCl reference electrode. In short, a negative potential on the Ag/AgCl contact transfers  $\text{Cl}^-$  from the contact to the solution increasing  $[\text{Cl}^-]$  and vice versa. With this strategy, we demonstrate precise spatiotemporal control of  $[\text{Cl}^-]$  in solution that can be used to affect physiological processes that are dependent on  $[\text{Cl}^-]$ . As proof-of-concept, we use  $[\text{Cl}^-]$  control to affect the membrane voltage on human pluripotent stem cells.

### 6.2.1 Introduction

Ranging from intercellular communication to organ function, ionic species play an important role in natural systems.<sup>251</sup> A majority of physiological processes, such as muscle contraction, neuronal signaling, and metabolism, involve the exchange of ions



between cells.<sup>252</sup> On the other hand, electrons and holes dominate communication between electronic devices. Bioelectronics bridges natural systems and electronic devices by translating ionic signals in the body into electronic signals for sensing and control.<sup>12, 51, 253-255</sup> Iontronic devices, for example, address individual ions and small molecules to control specific physiological pathways.<sup>254, 256, 257</sup> These include the precise delivery of  $\text{Ca}^{2+}$ ,  $\text{K}^+$  and gamma-Aminobutyric acid (GABA) to control epileptiform activities, and treat neuropathic pain with low dosage and less side effect.<sup>26, 28</sup> To this end, our group has demonstrated the control of  $\text{H}^+$  in field-effect transistors<sup>258</sup> and memories<sup>259</sup>, enzymatic logic gates and bioluminescence<sup>133</sup>, ion channel devices<sup>260-263</sup>,  $\text{H}^+$  modulators for delivery of cargo<sup>264, 265</sup> and glucose sensing<sup>265</sup>. These devices are enabled by using Pd/PdH<sub>x</sub> contacts, also known in the reversible H reference electrode, to translate electronic signals into  $\text{H}^+$  signals. This translation occurs according to the potential dependent reversible reduction,  $\text{H}^+ + \text{e}^- \leftrightarrow \text{H}$ , at the Pd/PdH<sub>x</sub> - solution interface and the subsequent physisorption of H onto Pd to form PdH<sub>x</sub>.<sup>131</sup> An electrical potential applied on the Pd/PdH<sub>x</sub> contact shifts the reaction equilibrium and induces the transfer of  $\text{H}^+$  to and from the solution, which effectively controls  $[\text{H}^+]$  in the solution.  $\text{Cl}^-$  is a major anion in physiological environment and functions importantly in many fundamental biological processes, including regulation of intracellular pH gradients, maintenance of intracellular volume, and resting membrane potential.<sup>266-269</sup> Controlling  $[\text{Cl}^-]$  in solution has great significance in regulating extra- and intra- cellular distribution of chloride, which

influences cell growth and differentiation, metastatic conversion, patterning of innervation, and neuronal excitability in the central nervous system.<sup>269-272</sup>

Here, we control  $[Cl^-]$  in solution by exploiting perhaps the best-known reference electrode, Ag/AgCl.<sup>273-276</sup> We do so by driving the reaction  $Ag + Cl^- \leftrightarrow AgCl + e^-$  out of equilibrium condition with a potential ( $V_{Cl^-}$ ) on the Ag/AgCl contact to effectively transfer  $Cl^-$  across the contact / solution interface (Figure 54). While Ag/AgCl is a well-known system, the use of Ag/AgCl to control  $[Cl^-]$  as an  $e^-$  to  $Cl^-$  transducer has yet to be reported to the best of our knowledge. Furthermore, we adapt Ag/AgCl contact to a bioelectronic device, a chloride modulator with a Chloride reservoir and a target chamber that is able to host cells. We use this Chloride modulator to demonstrate proof-of-concept actuation of membrane voltage ( $V_{mem}$ ) on human pluripotent stem cells (hiPSCs).

### 6.2.2 $Cl^-$ to electron transducer

First, we use an Ag/AgCl wire as a chloride transducer to show the ability of Ag/AgCl to control  $[Cl^-]$  in solution. We do so in a standard three-electrode configuration with the Ag/AgCl wire as working electrode (W), a glass Ag/AgCl as the reference electrode (R), platinum (Pt) wire as the counter electrode (C). Figure 54a describes how an anodic voltage,  $V_{Cl^-}$ , transfers  $Cl^-$  from solution to the Ag/AgCl wire according to  $Ag + Cl^- \rightarrow AgCl + e^-$  and thus reduces  $[Cl^-]$ . The excess  $e^-$  flows out of the Ag/AgCl contact into the lead. We use (N-(Ethoxycarbonylmethyl)-6-Methoxyquinolinium Bromide) (MQAE) to monitor  $[Cl^-]$ . MQAE is a diffusion-

limited collisional Cl<sup>-</sup>-quenched fluorescent dye whose intensity decreases when [Cl<sup>-</sup>] increases. We calibrate MQAE using the Stern–Volmer equation (Figure 55) and quantify [Cl<sup>-</sup>].<sup>277</sup> Figure 54b shows [Cl<sup>-</sup>] decreases from 50 mM to 32 mM when V<sub>Cl<sup>-</sup></sub> = 0.4 V for 100 s. Figure 54c describes how a cathodic voltage, V<sub>Cl<sup>-</sup></sub>, transfers Cl<sup>-</sup> from the Ag/AgCl wire to the solution according to  $\text{AgCl} + e^- \rightarrow \text{Ag} + \text{Cl}^-$  and thus increases [Cl<sup>-</sup>]. Figure 54d shows that [Cl<sup>-</sup>] increases from 0 mM to 48 mM when V<sub>Cl<sup>-</sup></sub> = -0.4 V for 100 s. These ranges and changes for [Cl<sup>-</sup>] are comparable to changes in [Cl<sup>-</sup>] plasma, interstitial fluids, and intracellular fluids<sup>266</sup> and they are thus relevant for biological applications.

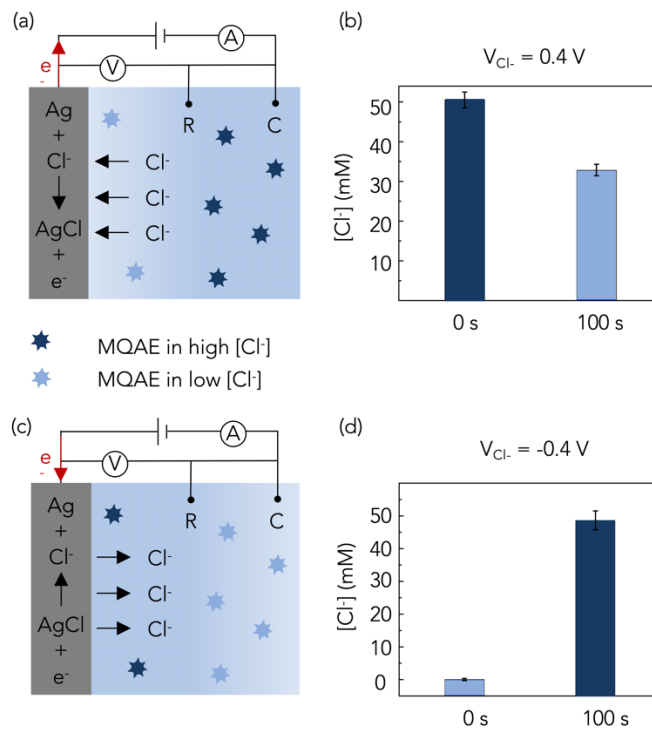


*Figure 54 Schematic of prototype chloride transducer and working mechanism. This setup has a standard three-electrode configuration. MQAE is a fluorescence dye monitoring [Cl<sup>-</sup>] change in solution, whose intensity increases with lower [Cl<sup>-</sup>]. (a) Anodic voltage transfers Cl<sup>-</sup> from solution into the Ag/AgCl contact, which decreases [Cl<sup>-</sup>] and brightens MQAE. (b) [Cl<sup>-</sup>] changes from 50 mM to 32 mM by applying 0.4 V for 100 s. (c) Cathodic voltage transfers Cl<sup>-</sup> from the Ag/AgCl contact into solution thus increasing [Cl<sup>-</sup>] and quenching MQAE. (d) [Cl<sup>-</sup>] changes from 0 mM to 48 mM by applying -0.4 V for 100 s.*

We use Keyence fluorescence microscope to take images of MQAE solution in the PDMS wells using DAPI filter, and ImageJ to analyze the fluorescence intensity. According to Stern–Volmer equation (Equation 19), [Cl<sup>-</sup>] shows linear relationship with  $(F_0/F - 1)$  between 0 – 100 mM.<sup>278</sup> We did the calibration by making 100  $\mu$ M MQAE solution in 0 mM, 2 mM, 8 mM, 10 mM and 50 mM KCl solution and measure the fluorescence intensity with the same imaging parameters, as shown in Figure 55. We're able to convert the intensity of the MQAE to [Cl<sup>-</sup>] to estimate the [Cl<sup>-</sup>] in the solution.

$$\frac{F_0}{F} - 1 = K_{SV}[\text{Cl}^-] \text{ Equation 19}$$

where  $F_0$  is the fluorescence intensity without Cl<sup>-</sup>;  $F$  is the fluorescence intensity in the presence of Cl<sup>-</sup>;  $K_{SV}$  is the Stern–Volmer constant.

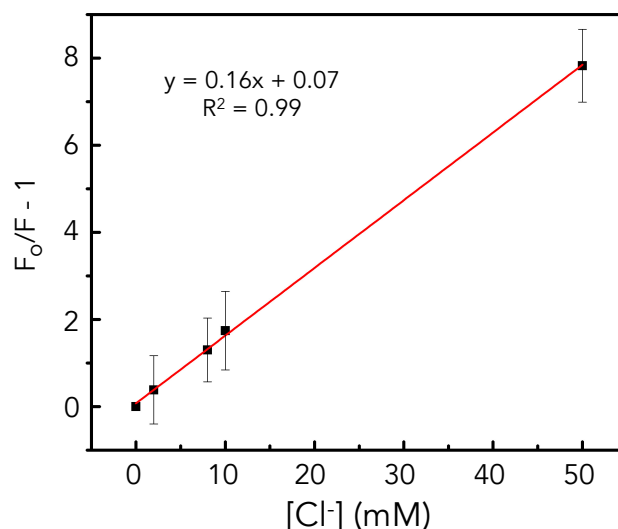
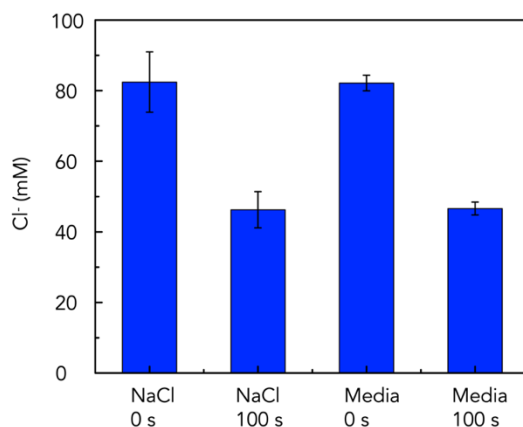


Figure 55 Stern–Volmer plot for quenching of MQAE by chloride. The volume of the solution is 20  $\mu$ L.

One of the advantages of using AgCl to transfer Cl<sup>-</sup> to and from solution is the fact that AgCl is selective to Cl<sup>-</sup> and is able to affect [Cl<sup>-</sup>] in physiological conditions with little to no interference from other ions. To this end, we demonstrate that the Cl<sup>-</sup> transducer works in a complex solution such as stem cell culture media (Neurobasal™-A Medium, ThermoFisher) that contains 79.6 mM NaCl, 26 mM NaHCO<sub>3</sub>, and 0.9 mM KH<sub>2</sub>PO<sub>4</sub>. With  $V_{Cl^-} = 0.6$  V for 100 s, we are still able to remove Cl<sup>-</sup> from solution and reduce [Cl<sup>-</sup>] from 79.6 mM to  $47 \pm 2$  mM. Repeating the experiment without HCO<sub>3</sub><sup>-</sup> and H<sub>2</sub>PO<sub>4</sub><sup>-</sup> ions leads to the same result with the final [Cl<sup>-</sup>] =  $46 \pm 5$  mM (Figure 56). While we are not able to monitor the change in concentration of the other anions, these results indicate that the presence of other

anions does not affect the  $\text{Cl}^-$  transducer indicating that  $\text{AgCl}$  is indeed specific to  $\text{Cl}^-$ . From our work with the  $\text{AgCl}$  wire, we found that transferring  $\text{Cl}^-$  from the  $\text{Ag}/\text{AgCl}$  contact into the solution is more efficient than transferring  $\text{Cl}^-$  from the solution to the contact. One of the reasons can be that when applying an anodic voltage,  $\text{Cl}^-$  are absorbed into  $\text{Ag}/\text{AgCl}$  electrodes immediately and a depletion area forms around the electrodes.<sup>279</sup> Then, the reaction is limited by  $\text{Cl}^-$  migration to the contact/solution interface. We further investigate the electrode kinetics of  $\text{Ag}/\text{AgCl}$  conversion in the next section to verify the hypothesis.



*Figure 56 Selectivity of  $\text{AgCl}$  to  $\text{Cl}^-$  in stem cell culture media.*

### 6.2.3 Kinetics of the conversion between $\text{Ag}$ and $\text{AgCl}$

To better understand and optimize the  $\text{Cl}^-$  transducer, we investigate the kinetics of  $\text{Cl}^-$  transfer at different potentials. Surprisingly, not many investigations on the kinetics of the conversion between  $\text{Ag}/\text{AgCl}$  under dynamic polarization or under other non-equilibrium exist.<sup>280</sup> For a  $\text{Ag}/\text{AgCl}$  electrode in solution containing  $\text{Cl}^-$ ,

the  $\text{Cl}^-$  in the  $\text{AgCl}$  are in equilibrium with the  $[\text{Cl}^-]$  in solution. As such, a  $\text{Ag}/\text{AgCl}$  contact shows a lower electrode potential in a solution with higher  $[\text{Cl}^-]$  and vice versa.<sup>267</sup> The well-known  $\text{Ag}/\text{AgCl}$  reference electrode takes advantage of this relationship by reading a constant potential when encapsulated in an internal electrolyte with a constant  $[\text{Cl}^-]$ .<sup>281</sup>  $\text{AgCl}$  has been used as gate electrode in organic electrochemical transistors (OECTs), which utilized its faradaic reactions in halide electrolytes to achieve higher current modulation compared to Pt electrodes.<sup>282</sup> However, there are few work exploring the dynamic change of  $\text{Ag}/\text{AgCl}$  system. Little is known about the kinetics of the conversion between Ag and  $\text{AgCl}$ .<sup>280, 283</sup> Although people have reported the open circuit potential (OCP) and cyclic voltammetry (CV) of  $\text{Ag}/\text{AgCl}$ , the analysis about the conversion between  $\text{e}^-$  and  $\text{Cl}^-$  is absent. Here, we explore the kinetics of  $\text{Ag}/\text{AgCl}$  conversion of miniaturized on-chip  $\text{Ag}/\text{AgCl}$  nanoparticles (NPs) electrodes. We use  $\text{Ag}/\text{AgCl}$  NPs to create an interface with higher surface area and capacitance for better conversion efficiency.<sup>284</sup> The conversion between  $\text{Ag}/\text{AgCl}$  under non-equilibrium conditions is consistent with  $\text{Cl}^-/\text{e}^-$  transformation, which is critical for controlling  $[\text{Cl}^-]$  with electronic means. We electroplate Ag NPs on thin-film Au contacts and chlorinate the Ag NPs into  $\text{Ag}/\text{AgCl}$  NPs in a 50 mM KCl solution (*Figure 57*). The bare  $\text{Ag}/\text{AgCl}$  NPs electrode we make here is a “quasi-reference electrode”, whose electrical potential depends on  $[\text{Cl}^-]$  in solution according to the thermodynamically-based Nernst relationship.

$$V_{Cl^-} = V_{Cl^-}^0 - 0.059 \lg[Cl^-] \quad \text{Equation 20}$$

where  $V_{Cl^-}^0$  is the standard potential of Ag/AgCl.

#### *Electroplating Ag/AgCl NPs:*

*Figure 57a* shows that silver chloride nanoparticles (Ag NPs) are electroplated on top of thin-film gold contacts on glass (2\*2 mm<sup>2</sup>). The electroplating process is accomplished from 10 mM AgNO<sub>3</sub> in 0.1 M KNO<sub>3</sub> using a three-electrode configuration at room temperature. An Ag/AgCl pellet serves as reference electrode, and a platinum wire coil serves as counter electrode. The following procedure yields the most repeatable and stable results among several plating procedures tested. First, we applied -0.3 V on Au contact for 150s and the surface becomes silver white color. In this process, approximately 0.005 C charges are measured in the circuit, which theoretically equals to the amount of Ag<sup>+</sup> deposited. Then, we oxidize approximately 20% Ag NPs to AgCl NPs by applying a constant anodic current (100 uA) for 10s on Ag NPs in 50 mM KCl solution at room temperature. We observe a clear color change from silver white to dark grey indicating the formation of AgCl NPs. Furthermore, we inspect the surface morphology with scanning electron microscopy (SEM). *Figure 57b* shows Ag NPs electroplated here, which uniformly covers the whole electrode surface. With higher magnification, it shows the signature cubic geometry of Ag NPs with 200 nm grain size in *Figure 57c*. *Figure 57d* shows 20% chlorinated Ag/AgCl NPs. It's clear that an additional layer is visible on top of Ag



NPs, and the grain of AgCl NPs is more amorphous with approximately 500 nm size. With further chlorination of Ag NPs (40%), the SEM image in *Figure 57e* shows more AgCl NPs.

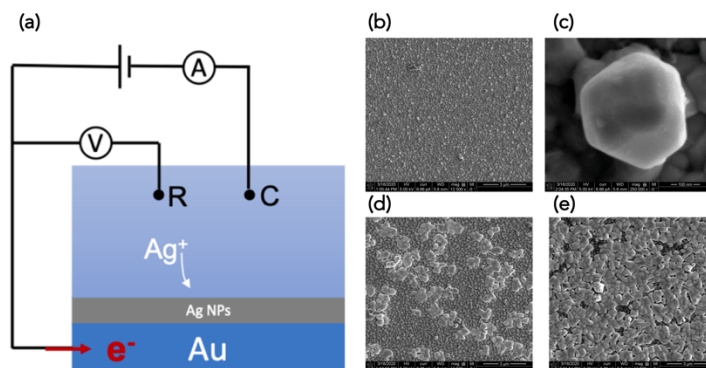


*Figure 57 (a) Ag/ AgCl NPs electroplating and chlorination. (b-e) Morphology of Ag/AgCl NPs by SEM images of (b) Ag NPs after electroplating; (c) single Ag NPs with the signature shape; (d) Ag/AgCl with 20% chlorination; (e) Ag/AgCl with 40% chlorination.*

Ag/AgCl conversion depends on  $[Cl^-]$  in solution and the applied potential ( $V_{Cl}$ ). Here we record the open circuit potential ( $V_{OCP}$ ) of Ag/AgCl contact in various  $[Cl^-]$  solution under equilibrium conditions with a three-electrode configuration at room temperature. Figure 58a shows the  $V_{OCP}$  of Ag/AgCl in 1 mM, 10 mM, 100 mM and 1 M KCl, respectively.  $V_{OCP}$  and logarithmic scale of  $[Cl^-]$  shows a linear relationship with a slope of -55.35 mV and  $R^2 = 0.99$ , as expected from the Nernst equation. We use the values of  $V_{OCP}$  to define process map for the  $Cl^-$  transducer as a function of  $[Cl^-]$  and  $V_{Cl}$  (Figure 58a). The straight line in the graphs joins the  $V_{OCP}$ 's at different

$[\text{Cl}^-]$  and represents equilibrium (as many  $\text{Cl}^-$  transfer from the solution into the electrode as they transfer from the electrode into the solution). This line also marks the threshold of the Ag/AgCl conversion. For a combination of  $V_{\text{Cl}^-}$  and  $[\text{Cl}^-]$  in the gray area below the line,  $\text{Cl}^-$  transfer into the solution increasing  $[\text{Cl}^-]$  and for a combination of  $V_{\text{Cl}^-}$  and  $[\text{Cl}^-]$  above the line in the white area  $\text{Cl}^-$  transfer from the solution decreasing  $[\text{Cl}^-]$ .

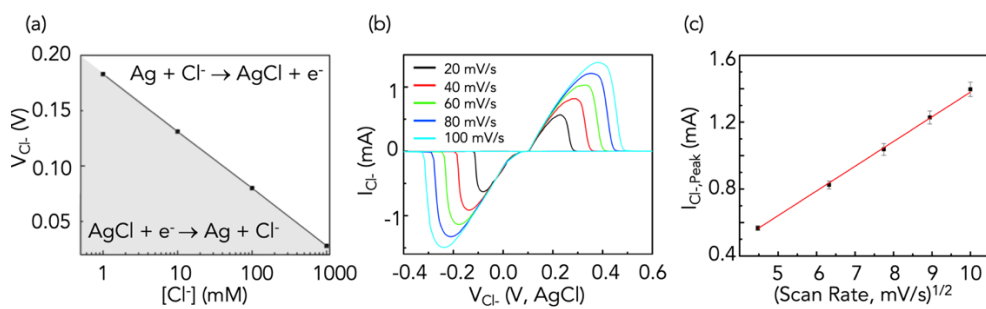


*Figure 58 Kinetics of the conversion between Ag/AgCl. (a) The linear relationship between  $V_{\text{OCP}}$  and logarithmic scale of  $[\text{Cl}^-]$  represents equilibrium as well as the threshold of Ag/AgCl conversion. In the white area above the line,  $\text{AgCl} + e^- \rightarrow \text{Ag} + \text{Cl}^-$ ; in the gray area under the line,  $\text{AgCl} + e^- \leftarrow \text{Ag} + \text{Cl}^-$ , (b) CV of Ag/AgCl electrodes with a series of scan rates, 20 mV/s, 40 mV/s, 60 mV/s, 80 mV/s, 100 mV/s. The redox peaks show that the reaction is electron transfer dominated, and the current increases with higher scan rate due to reduced diffusion layer. (c) Relationship of anodic peak current of Ag/AgCl ( $I_{\text{Cl}^-, \text{Peak}}$ ) versus square root of the scan rate in CV measurements. The excellent linear relationship shows that the*

*reaction is limited by the diffusion of Cl<sup>-</sup> to the electrode following Randles–Sevcik equation.<sup>285</sup> The standard error is derived from 3 electrodes.*

To further study the electrode kinetics at the interface of Ag/AgCl contact and solution, we investigate the limiting mechanism of this electrochemical reaction (Figure 58b). In detail, we cycle the voltage of Ag/AgCl NPs electrodes between -0.8 V and 0.8 V, versus a glass Ag/AgCl electrode. Pt wire is the counter electrode as usual. We use a series of scan rates, 20 mV/s, 40 mV/s, 60 mV/s, 80 mV/s and 100 mV/s, respectively. Taking 40 mV/s as an example, the interfacial reaction can be explained as below. During the scan of  $V_{Cl^-}$  from 0 V to 0.8 V, Cl<sup>-</sup> is absorbed onto Ag/AgCl and oxidizes Ag to AgCl.  $I_{Cl^-}$  increases to a peak with higher  $V_{Cl^-}$  and then becomes smaller by the delivery of Cl<sup>-</sup> from the bulk solution. Thus, the mass transport of Cl<sup>-</sup> becomes the limitation of the electrochemical reaction, and the current decays gradually.<sup>285</sup> After the scan direction is switched to negative,  $V_{Cl^-}$  is still sufficiently positive to oxidize Ag, so  $I_{Cl^-}$  continues until  $V_{Cl^-}$  becomes strong enough to reduce AgCl. Then Cl<sup>-</sup> starts to be released from the electrode, reaches a cathodic peak and decays as AgCl is consumed. With the scan rate increase, the diffusion layer becomes smaller and it takes less time to record one cycle, inducing  $I_{Cl^-}$  increases.<sup>286, 287</sup> The measured current in CV with a redox couple is mainly faradaic current, which is from the charge transfer at the interface of the electrode contact/solution and depends on the kinetics of charge transfer at the surface and the redox species diffusion to the surface.<sup>286</sup> We plot the peak currents ( $I_{Cl^-,Peak}$ ) of CV

versus the square root of scan rates of 3 electrodes in Figure 59, which all show an extraordinary proportional relationship, and the standard error is shown in Figure 58c. According to Randles–Sevcik equation (Equation 21), the analytes, Cl<sup>-</sup>, are not adsorbed on the electrode but freely diffused in the solution. Thus, we conclude that Ag/AgCl conversion is a Cl<sup>-</sup>-diffusion controlled reversible electrochemical reaction.<sup>285</sup>

$$I_{Cl^-,Peak} = 0.4463nFAC\left(\frac{nFvD}{RT}\right)^{\frac{1}{2}} \text{ Equation 21}$$

Where  $I_{Cl^-,Peak}$ , R, F, T are peak current of cathodic or anodic reaction, gas constant, Faraday constant, absolute temperature, respectively. A, C, D, v, are electrode area, concentration of the analyte, diffusion coefficient and scan rate of CV.

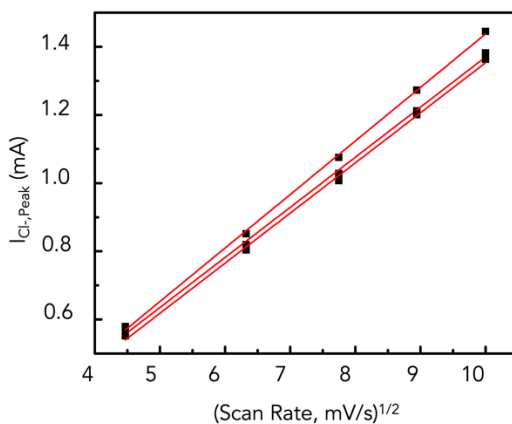


*Figure 59 Relationship of anodic peak current of Ag/AgCl ( $I_{Cl^-,Peak}$ ) versus square root of the scan rate in CV measurements of 3 AgCl NPs electrodes, which all show excellent linear relationship.*

The slight difference of the slope is from the surface area difference of each electrode according to Randles–Sevcik equation, which happens in the AgCl NPs deposition process.

#### 6.2.4 Chloride modulator with cells

As the translation between  $Cl^-$  and  $e^-$  is in parallel with the conversion between Ag/AgCl, which depends on  $V_{Cl^-}$  and  $[Cl^-]$  in solution, we can feasibly adapt Ag/AgCl electrode to various bioelectronic devices and utilize it to selectively control  $[Cl^-]$  in solution with  $V_{Cl^-}$ . Here we design a chloride modulator, which transfers  $Cl^-$  from a reservoir electrolyte with rich  $Cl^-$  source to a target electrolyte under control. The Ag/AgCl NPs are the working electrode. The selectivity of AgCl to  $Cl^-$  ensures it a storage media specifically to  $Cl^-$  and allows  $Cl^-$  to move between reservoir and target depending on  $V_{Cl^-}$ . Thus, the chloride modulator can manipulate  $[Cl^-]$  in a much more extensive range than a single Ag/AgCl contact. As proof-of-concept, we culture cells in the target chamber and study the effect of  $[Cl^-]$  modulation on their function.

Figure 60a shows the schematic of the chloride modulator (side view), and the design is similar to previously reported proton modulator with Pd/PdH<sub>x</sub> electrodes.<sup>264</sup> The chloride modulator is composed of two independent chambers, referred as reservoir

(left) and target (right), respectively, connected by an anion exchange membrane (AEM). Figure 60b shows the optical image of the device. Reservoir has 0.1 M KCl to provide a rich  $\text{Cl}^-$  source, and we change  $[\text{Cl}^-]$  of the target solution, which can contain 100  $\mu\text{M}$  MQAE in DI water (Figure 60c), or cells (Figure 60d, e). We use an Ag/AgCl NPs microelectrode as the working electrodes, providing multiple independent openings for  $\text{Cl}^-$  to enter / leave the target solution. Here we define the potential different between Ag/AgCl and Pt electrode in reservoir as  $V_{\text{Cl-R}}$ , the potential difference between Ag/AgCl and Pt electrode in target as  $V_{\text{Cl-T}}$ . AEM is a polymer with high conductivity for anions due to their large amount of fixed cationic groups that support the storage and transport of mobile anions through the membrane, and its exclusion to cations ensures the majority of measured currents are from the moving of anions.<sup>288</sup> Here, AEM is a mixture of polyvinyl alcohol (PVA) and Poly (diallyldimethylammonium chloride) (PDDA), which work as the hydrophilic matrix and polycation, respectively. To avoid the undesirable passive diffusion current caused by the  $[\text{Cl}^-]$  gradient between reservoir and target, we pattern a thin cation exchange membrane (CEM), PVA and polystyrene sulfated acid (PSS) mixture at the opening of the MEAs to form a Donnan exclusion barrier. The AEM and CEM function together to provide a bridge that allows for an electrophoretic  $\text{Cl}^-$  flow during stimulation with a voltage across the bridge and minimization of passive diffusion current. More details about device fabrication are in Figure 62.

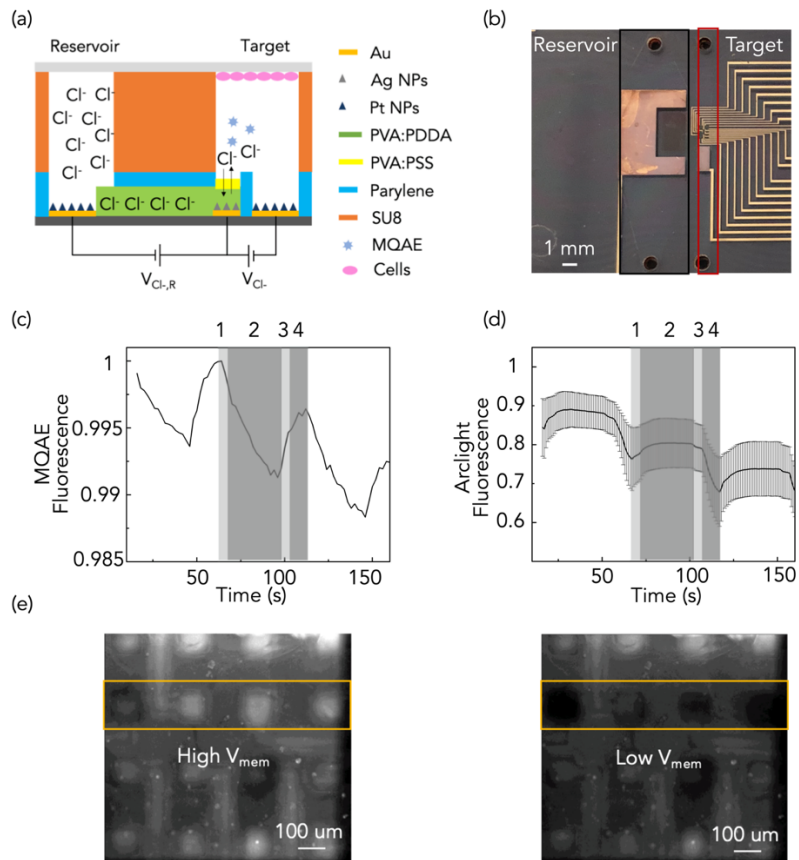


Figure 60 Chloride modulator. (a) Schematic of the chloride modulator (side view) and operating principle. Reservoir and target are connected by an anion exchange membrane (AEM), in which Cl<sup>-</sup> are driven by  $V_{Cl-R}$ . Reservoir has a high [Cl<sup>-</sup>] solution providing Cl<sup>-</sup> source, and [Cl<sup>-</sup>] in target is under control. (b) Optical image of the chloride modulator. The reservoir (black line) and target (red line) are separated by SU 8 microfluidic channels and the holes on the glass slide provides the inlet and outlet. (c) [Cl<sup>-</sup>] change results from the 4-step process in Table 1 for 3 cycles, which is indicated by the MQAE fluorescence intensity. Temporal change corresponding to each step is shown with different colors in the second cycle as a

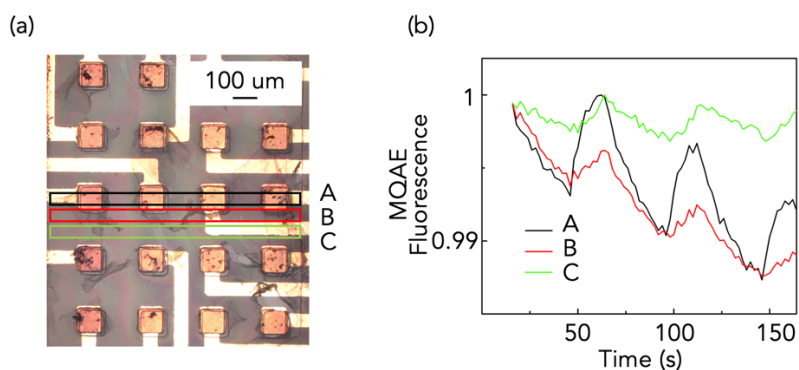
representation. (d)  $V_{mem}$  change of cells results from the same operation is indicated by ArcLight fluorescence intensity. The data come from 3 devices. (e) Fluorescence images of the cells over MEAs with high  $V_{mem}$  ( $t = 75$  s) and low  $V_{mem}$  ( $t = 119$  s). The highlighted row is under operation.

Table 8 4-step process that modulates  $[Cl^-]$  in target solution

	<b>Step</b>	<b><math>V_{Cl^-, R}</math></b> <b>(V)</b>	<b><math>V_{Cl^-}</math></b> <b>(V)</b>	<b>Time</b> <b>(s)</b>	<b><math>[Cl^-]</math></b>
<b>1</b>	Transfer $Cl^-$ from Reservoir to AgCl	2	0	5	High
<b>2</b>	AgCl release $Cl^-$ to Target	0	-1.5	30	High
<b>3</b>	Remove $Cl^-$ from AgCl to Reservoir	-1	0	5	Low
<b>4</b>	AgCl absorb $Cl^-$ from Target	0	1	10	Low

We design a 4-step process in Table 1 to control  $[Cl^-]$  in target solution periodically by driving  $Cl^-$  from and back to the reservoir, which results in the  $[Cl^-]$  changes shown in Figure 60c. The  $Cl^-$  modulator also achieves diffusion limited spatial resolution with larger  $[Cl^-]$  changes occurring close to the contacts that are active, with little or no  $[Cl^-]$  changes observed in the non-active region (Figure 61).





*Figure 61 Diffusion limited spatial resolution of the  $\text{Cl}^-$  modulator.*

In Figure 61, we activate microelectrodes in area A, and analyze  $[\text{Cl}^-]$  distribution in area A, B, C. When we transfer  $\text{Cl}^-$  from reservoir to target solution,  $[\text{Cl}^-]$  change in area B is slightly less than that in area A, because there are sufficient  $\text{Cl}^-$  supply from reservoir. However, it shows much less change when transferring  $\text{Cl}^-$  from target solution to the reservoir, because the reaction to absorb  $\text{Cl}^-$  from target solution is confined by  $\text{Cl}^-$  diffusion from area B to area A. Moreover, when the distance gets further to area C,  $[\text{Cl}^-]$  change is significantly less and shows temporal delay compared to that in area A.

As proof-of-concept, we used the chloride modulator to study the effects of extracellular  $[\text{Cl}^-]$  on human pluripotent mammalian stem cells (hiPSCs) and their  $V_{\text{mem}}$  (Figure 60d and e). A cell's resting potential,  $V_{\text{mem}}$ , is an electrical control signal that occurs between the inside of the cell and the extracellular environment.<sup>289</sup>  $V_{\text{mem}}$  affects cell physiology and functions such as proliferation, differentiation,

migration and apoptosis, as well as cell-cell communication, and large-scale morphogenesis.<sup>290</sup>

Chloride is the major anion in extracellular environments. In hiPSCs, an increase in extracellular  $[Cl^-]$  results in cell hyperpolarization (higher  $V_{mem}$ ), and a decrease in extracellular  $[Cl^-]$  results in cell depolarization (lower  $V_{mem}$ ).<sup>291</sup> We measure  $V_{mem}$  of the hiPSCs using ArcLight, a fluorescent reporter that we expressed on the cell membrane, whose fluorescence intensity increases when  $V_{mem}$  increases.<sup>292</sup> By switching the environment between high  $[Cl^-]$  and low  $[Cl^-]$  conditions using the same protocol in Table 1, we observe that  $V_{mem}$  of hiPSCs shifts with the expected pattern as measured by the ArcLight fluorescence intensity (Figure 60d). Figure 60e shows the fluorescence images of the cells at  $t = 75$  s and  $t = 119$  s, corresponding to high (hyperpolarized) and low  $V_{mem}$  (depolarized), respectively. This change in fluorescence occurs close to the activated area and not far away from the active electrodes indicating that the induced change in  $[Cl^-]$  is responsible for the measured  $V_{mem}$  change. While this is a proof-of-concept, it shows how the  $Cl^-$  modulator is able to affect cell function.

### 6.2.5 Conclusion

Ag/AgCl is a well-known reference electrode that has been used in electrochemistry for decades. Here we first demonstrate Ag/AgCl as a  $Cl^-$  transducer that controls  $[Cl^-]$  by transferring  $Cl^-$  from and to solution controlled by an applied voltage,  $V_{Cl^-}$ . Furthermore, we investigate kinetics of the conversion between Ag/AgCl by

electrochemical techniques, which is consistent with  $\text{Cl}^-/\text{e}^-$  transformation and critical for controlling  $[\text{Cl}^-]$  with electronic means. This control paves the way to the integration Ag/AgCl into complex bioelectronic devices, for dynamic control of bioelectric signaling in vivo and in vitro models of physiology and morphogenesis. As a proof of concept, we adapt Ag/AgCl into a chloride modulator that precisely regulates  $[\text{Cl}^-]$  in solution and affect membrane voltage of pluripotent stem cells. Since  $\text{Cl}^-$  is a critical anion in bioelectricity, the accurate regulation of  $[\text{Cl}^-]$  is currently in high demand and has potential in bioelectronic therapies.

#### 6.2.6 Experiment section

##### *Materials:*

All materials are purchased from Sigma-Aldrich and used without further modification unless specifically mentioned.

##### *Electrochemical characterization*

All the electrochemical characterization is done on a computer controlled Autolab potentiostat with analytic software Nova 2.0.

*Device Fabrication:* Micrometer size  $\text{Cl}^-$  modulator was fabricated using photolithography. Glass slides were sonicated for 20 min in 80% v/v acetone and 20% v/v iso-propanol (IPA), and dried with  $\text{N}_2$ . S1813 (Dow chemicals) photoresist was deposited on top of the glass substrates, following standard protocols

(spin-coated at 3000 rpm, baked 1 min. at 110 °C) to create the Au patterns. Ti 10 nm and Au 100 nm were evaporated using an e-beam evaporator, and a lift-off process (sonication in 80% v/v Acetone and 20% v/v IPA for 5 min) defined the metal contacts and interconnects. An additional S1813 process defined the area of the Au contacts for electrodeposition of Ag/AgCl NPs and Pt NPs, while the metal interconnects were insulated. Then, a 1.4 µm insulating layer of parylene-C was deposited (Specialty Coating Systems Labcoater 2 system) in the presence of A174 adhesion promoter in the deposition chamber. The parylene was etched with an oxygen plasma at 200 W with the regions over the electrodes and contact pads exposed, and the interconnecting regions protected by a thick positive photoresist (SPR220-4.5, Micro-Chem Corp.). Prior to deposition of polymer, wafers were treated with the a 5% solution of (3- Glycidyloxypropyl)trimethoxysilane (GOPS) in ethanol via spin coating at 1000 rpm for 30 s and then baked at 110C for 5 minutes to promote adhesion of the polymer. The AEM is a blend of 10 wt% polyvinyl alcohol (PVA) and 20 wt% Poly (diallyldimethylammonium chloride) (2:1 weight ratio), which was thoroughly mixed (PVA: PDDA solution) and sonicated for 45 min. The PVA: PDDA solution was filtered with a filter porous size of 0.8 µm and was spin-coated on top of the samples at 1500 rpm for 30 s and baked in 120 °C for 2h, yielding a film thickness of 2 µm. The PVA: PDDA AEM was etched with an oxygen plasma at 200 W with the desired pattern defined with SPR220-4.5 photoresist. A second 1.4 µm coating of parylene was then deposited with the same protocol as above to insulate and protect the ion bridge from the subsequent steps. To promote

adhesion between the parylene and SU8 photoresist, GOPS was again deposited using the above process prior to SU8 patterning. SU8 was spun onto the wafer at a speed of 1000 rpm for 30 s and a ramp of 300 rpm, microfluidic channels of height 40  $\mu\text{m}$  were patterned forming the sidewalls reservoir and target chambers. The parylene insulation layer protecting the ion bridge openings in the reservoir and target channels were defined and etched using the same process as the previous parylene etch. Then, a mixture of 8%wt polyvinyl alcohol (PVA) and 2% polystyrene sulfonic acid (PSS) in water was then passed through a 0.8  $\mu\text{m}$  MCE syringe filter and spin coated at 3000rpm for 30s followed by baking at 120C for 2 hours. The polymer film was patterned in SPR220 photoresist and etched with O<sub>2</sub> reactive ion etching. Finally, Single sided microfluidic diagnostic tape (3M 9956) was cut by CNC machine to make the openings over AgCl MEA for imaging and then aligned to features on the device and pressed to seal the microchannels by hand.

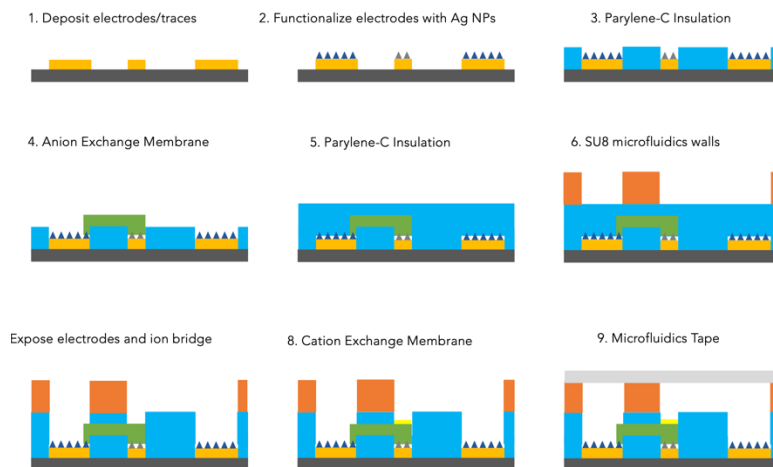


*Figure 62 Fabrication scheme for the proton pump array. (1) E-beam deposition of Au electrodes and traces. (2) Electrochemical deposition of Pd and Ag on the electrodes, followed by chlorination of Ag to form AgCl. (3) Parylene-C deposition. (4) Spin-coating of PVA: PDDA AEM and etching. (5) Parylene-C deposition. (6) SU8 patterning to form microfluidic walls. (7) O<sub>2</sub> etch of Parylene-C to expose the ion bridge and the AgCl electrodes. (8) Spin-coating and patterning of the PVA: PSS CEM. (9) Sealing the fluidics with a thin microfluidic tap.*

#### *Electrodeposition of platinum nanoparticles:*

Pt NPs are electrodeposited on top of the Au contacts of two auxiliary electrodes by using 0.5 mg / ml H<sub>2</sub>PtCl<sub>6</sub> water solution with a constant voltage of -0.06 V for 20 s and 160 s, respectively. Commercial Ag/AgCl electrode is used as a RE and Pt wire was used as a counter electrode (CE).

#### *Device operation*

We assemble the chloride modulator on an acrylic support rig that allows for low pressure clamping of a PDMS slab over the opening of the target microfluidics channel. The acrylic rig also provides a pogo-pin interface for connecting to a custom stimulation board that can stimulate eight independent channels simultaneously.

The custom design stimulation unit is used to stimulate eight individual channels. Each channel has an output range of -4 to +4V with a resolution of 1.95 mV, and the current measurement range from -1.6 to +1.6 uA with a resolution of 0.8 nA. Also,

the stimulation unit has an open-circuit feature where it can completely disconnect some channels without changing the experiment setup. The stimulation has two operating modes: (1) standalone - the unit follows a pre-program protocol (2) networking mode - the unit waits for a command from an external controller (e.g., Machine learning algorithm) via a wireless connection.

### *Cells*

hiPSCs were a generous donation from David Kaplan's group (ND418566, NINDS Human Genetics and DNA Cell Line Repository<sup>293</sup>). Stem cells were maintained at 5% CO<sub>2</sub> in StemFlex Medium (A3349401, ThermoFisher) on hESC Qualified Matrigel Matrix (354277, Corning) coated plates with the dilution recommended by the manufacturer. Cells were disassociated with TrypLE Select (12563029, ThermoFisher). Transgenic cells were made by transfecting 500 ng of plasmid via 1  $\mu$ L of lipofectamine 3000 (L3000008, ThermoFisher) per well of 24 well plate containing 500  $\mu$ L of Opti-MEM (31985062, ThermoFisher) with 1X RevitaCell (A2644501, ThermoFisher). Reagent was removed after 4 hrs and replaced with StemFlex. Cells were allowed to recover for 3 days before being selected with 50  $\mu$ g/mL G418 in StemFlex with 10  $\mu$ g/mL ROCK inhibitor Y-27632 (72304, STEMCELL Technologies). After selection, a stable, clonally pure line was made by serial dilution using StemFlex with 1X RevitaCell. Clones were expanded in StemFlex and then assayed for alkaline phosphatase activity (SCR004, Millipore). The clone with best membrane localization and expression of ArcLight was chosen

for further experimentation and frozen down using NutriFreez D10 (05-713-1E, Biological Industries). Prior to being used in experiments, hiPSC ArcLight cells were plated in mTeSR1 no phenol red (05876, STEMCELL Technologies) and allowed to expand for two passages prior to seeding on PDMS slabs that were coated in hESC Qualified Matrigel Matrix. Slabs were used in bioelectronic chips one to three days after seeding. Cells were perfused with mTeSR1 no phenol red during experiments.

#### *Plasmid Construction*

A pENTR1A plasmid with a CAG promoter and multiple cloning site followed by a SV40 poly A was used to clone in the mammalian codon optimized ArcLight Q239 from the plasmid CMV ArcLightCo (Q239)-T2A-nls-mCherry, a gift from Vincent Pieribone (Addgene plasmid # 85806 ; <http://n2t.net/addgene:85806> ; RRID:Addgene\_85806). Cloning was done by In-Fusion HD Cloning Plus (638909, Takara) with HindIII and Sall restriction enzyme sites added. PCR was done using PrimeSTAR GXL DNA polymerase (R050A, Takara). The resulting pENTR1A CAG ArcLightCo construct was then Gateway LR clonased (11791020, ThermoFisher) into the hyperactive piggyBac transposase-based, helper-independent and self-inactivating delivery system, pmhyGENIE-3 containing a neomycin resistance gene in the backbone for selection, a gift from Stefan Moisyadi<sup>294</sup>. The resulting plasmid HypG3NeoBBArcLightCo (Q239) was used for subsequent transfections.

This section is reproduced from <sup>3</sup>.



### 6.3 Four-ion pump

Ions and biomolecules are signal carriers in biological systems to transfer information for intracellular communication and organism function. As such, bioelectronic devices that conduct ions rather than electrons and holes provide an interface to monitor and control physiological processes. These processes often are affected by multiple distinct ionic species. Here, we develop an ion pump that can control the delivery of multiple ionic species on the same chip. We demonstrate on-chip delivery of  $H^+$ ,  $Na^+$  and  $Cl^-$  by monitoring the dynamic concentration change using fluorescent dyes. We integrate the multi-ion pump with machine-learning (ML) driven closed-loop control of delivery to ensure precise dose control. The ability to deliver multiple ions to the same biological systems with tight control of their concentrations enables to finely regulate the extracellular environment to precisely control several physiological processes.

#### 6.3.1. Introduction

Bioelectronic devices aim to bridge the gap between biological system and electronic devices.<sup>1,2</sup> Signal transmission in biological system mainly relies on ion fluxes and the movement of biomolecules, such as neurotransmitters, while conventional electrical devices control electrons and holes.<sup>2</sup> Various tools have been developed to control or

monitor the activities of ions and biomolecules with electronic or optical signals for the purpose of diagnostics, and therapies.<sup>295, 296</sup>

Iontronic devices generate, store, and transmit signals via modulating the flow and concentration of ion and small molecules.<sup>17</sup> In analogy to electronics, examples of iontronic components include organic electrochemical transistors (OECTs),<sup>18</sup> organic electronic ion pumps (OEIPs),<sup>232</sup> ionic diodes,<sup>297</sup> transistors,<sup>258</sup> and memristors,<sup>259</sup> bipolar membrane junctions.<sup>22</sup> By manipulating ions and biomolecules directly, iontronic devices extend the domain from electrically excitable cells to all cell types, such as stem cells to guide differentiation<sup>298, 299</sup> and skin cells for improved wound healing.<sup>300 301</sup> Furthermore, iontronic devices are more effective on biological processes that are influenced by specific ions and biomolecules, such as H<sup>+</sup> for enzyme activities, gene expression, and neuronal function,<sup>302</sup> Cl<sup>-</sup> for cancer and birth defects,<sup>269</sup> and gamma-aminobutyric acid (GABA) for suppression of epilepsy.<sup>26</sup>

Among these iontronic devices, OEIPs are used to deliver charged ions and biomolecules with high spatiotemporal resolution and dosage precision (one electron per delivered monovalent ion).<sup>25</sup> In recent years, OEIPs have been reported to deliver H<sup>+</sup>, K<sup>+</sup>, Ca<sup>++</sup>, GABA, which enabled triggering cell polarization status in vitro,<sup>25</sup> controlling epileptiform activity in brain slice models,<sup>26</sup> affecting sensory function in vivo,<sup>27</sup> suppressing pain sensation in awake animals,<sup>28</sup> and even modulating plant physiology.<sup>29</sup> Moreover, some physiological processes need more than one species cooperation at the same time, such as the fact that the early embryonic face is patterned by H<sup>+</sup> and K<sup>+</sup> ion gradients.<sup>303, 304</sup> Therefore, we demonstrate the first

multiple-ion pump that can selectively deliver multiple different ionic species simultaneously including both cations and anions. It is composed of four independent reservoir electrolytes connected to one target electrolyte, in which 36 microelectrodes are independently controlled with 50-um resolution and reach almost single-cell level control. Here we used three major ions in physiological processes,  $H^+$ ,  $Na^+$ ,  $Cl^-$  as the model, while they can be replaced with any desired charged species, such as neurotransmitters and drugs. As a proof of concept, we also used machine learning algorithm to change the ion concentration towards the desired goal in a closed-loop manner. Thus, this multi-ion pump not only enables controlling complicated physiological processes that need more than one ionic species, but also provides a highly efficient and customized toolbox for fundamental biological research with an intelligent manner.

### 6.3.2. Result and Discussion

Figure 63a shows the top view of the multi-ion pump, which comprises four independent reservoirs (R1, R2, R3, R4) connected to one target. Each reservoir has one reference electrode to deliver ions from the reservoir to 9 independent microelectrodes (3 x 3 array) in the target through an independent ion channel. Figure 63b shows the mapping of the 36 microelectrodes in the target: every four microelectrodes form an array to deliver different ionic species. Here we used three channels to deliver  $H^+$ ,  $Na^+$ , and  $Cl^-$ , and named each individual type as  $H^+$  pump,  $Na^+$  pump,  $Cl^-$  pump, respectively. We coated nanoparticles on the microelectrodes to

increase the surface area and electrode capacitance. The microelectrodes of  $H^+$  pump were coated with Pd NPs, which are selective to  $H^+$  by forming  $PdH_x$ .<sup>305</sup> AgCl nanoparticles were coated on microelectrodes connected to  $Cl^-$  pump because of its selectivity to  $Cl^-$ . For all the other general ionic species, platinum nanoparticles (Pt NPs) were deposited to increase the surface area of the microelectrodes as well as the capacitance for general delivery, such as  $Na^+$ . The reference electrodes in the reservoir and auxiliary electrode were AgCl NPs, which work as an electron-to-ion transducer.<sup>3</sup> On top of the microelectrodes, we deposited four independent ion channels that connected reservoirs and target by spin-coating and patterned by photolithography in two layers separated by parylene to avoid interfering. Here, negatively charged polymer, Poly vinyl Alcohol: Polystyrene sulfonate (PVA:PSS), was used for cations delivery and coated as 3 ion channels. Positively charged PVA:Chitosan was used for anion delivery and coated as 1 ion channel. Then, SU8 photoresist was used to build the microfluidic channels to provide solutions for the reservoirs and target. The microfluidic channels were sealed by microfluidic tape. More details about the device fabrication are in Experiment Section. Figure 63c is the side view of the multi-ion pump showing the multilayer structure and the electrical circuits with  $H^+$  reservoir as the representative.

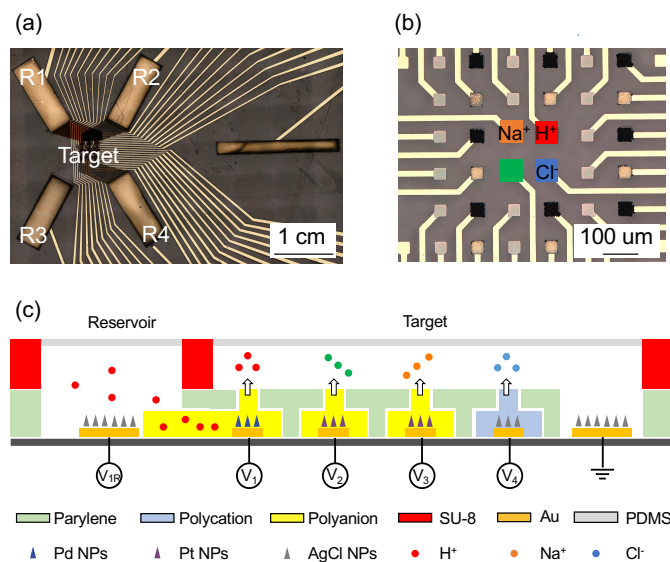


Figure 63 (a) Top view of multiple-ion pump, showing four reference electrodes in the reservoirs (R1, R2, R3, R4), microelectrodes and auxiliary electrode in the target. (b) Mapping of the 36 microelectrodes in the target: every four microelectrodes form an array to deliver different ionic species. Every four microelectrodes form a group that can control four different ions and such groups form a 3 x 3 matrix in the target solution. (c) The side view of the multi-ion pump with one reservoir as the representative, showing the multilayer structure.

Figure 64a shows the fluorescence image of the target electrolyte, and the yellow square highlights a group of microelectrodes that are connected to different reservoirs. Here we demonstrated ion concentration control on three ions: H<sup>+</sup>, Na<sup>+</sup>, Cl<sup>-</sup>. For [H<sup>+</sup>], 0.1 M HCl was used as the reservoir electrolyte and 5-(and-6)-Carboxy SNARF<sup>TM</sup>-1 was used as fluorescent pH indicator in the target electrolyte to monitor pH in real time. In Figure 1b, first, we applied  $V_{IR} = 1.6$  V between the R1 in the H<sup>+</sup> reservoir

and  $H^+$  microelectrodes to deliver  $H^+$  to  $H^+$  channel. Then we applied  $V_1 = 1.6$  V to deliver  $H^+$  from microelectrodes into the target, which increased the  $[H^+]$  in the area close to the microelectrodes. Next, we reversed  $V_1$  to be  $-1.6$  V to absorb  $H^+$  back to the  $H^+$  channel, inducing  $[H^+]$  decrease. Figure 2b shows the  $[H^+]$  change following  $V_1$ , indicating a quick and precise  $[H^+]$  control by the voltage. For  $Na^+$ , 0.1 M NaCl was used in the reservoir electrolyte, and CoroNa fluorescence dye was used in target electrolyte to monitor  $[Na^+]$  in real time.  $[Na^+]$  control was achieved by the same protocol as that of  $[H^+]$  (Figure 2c), because they are all cations. For  $Cl^-$ , 0.1 M NaCl was in the reservoir electrolyte and MQAE was used as fluorescent indicator in the target electrolyte to monitor  $[Cl^-]$  in real time. Here, we applied  $-1.8$  V between R4 in the  $Cl^-$  reservoir and  $Cl^-$  microelectrodes to deliver  $Cl^-$  into  $Cl^-$  channel. Then we applied  $V_4 = -1.8$  V to deliver  $Cl^-$  to the target, which increases  $[Cl^-]$  of the area close to the microelectrode. Next, we reversed  $V_4$  to be  $1.8$  V to absorb  $Cl^-$  and reduced  $[Cl^-]$  (Figure 2d).

Besides the temporal resolution, the high spatial resolution control of ion pumps is another critical advantage for ion/biomolecule delivery. In Figure 2e, when we applied voltage on one working microelectrode (yellow), the fluorescence intensity in the rectangular square (black, red, blue, pink) was measured to show the ion concentration in the adjacent area of the working microelectrode. Following the aforementioned protocols that change  $[H^+]$ ,  $[Na^+]$  and  $[Cl^-]$ , we measured and plotted their fluorescence intensity in different area (Figure f, g, and h). The results show that while the monitored area gets further from the working microelectrodes, the ion

concentration change by the voltage is diminished, indicating a precise control of spatial resolution.

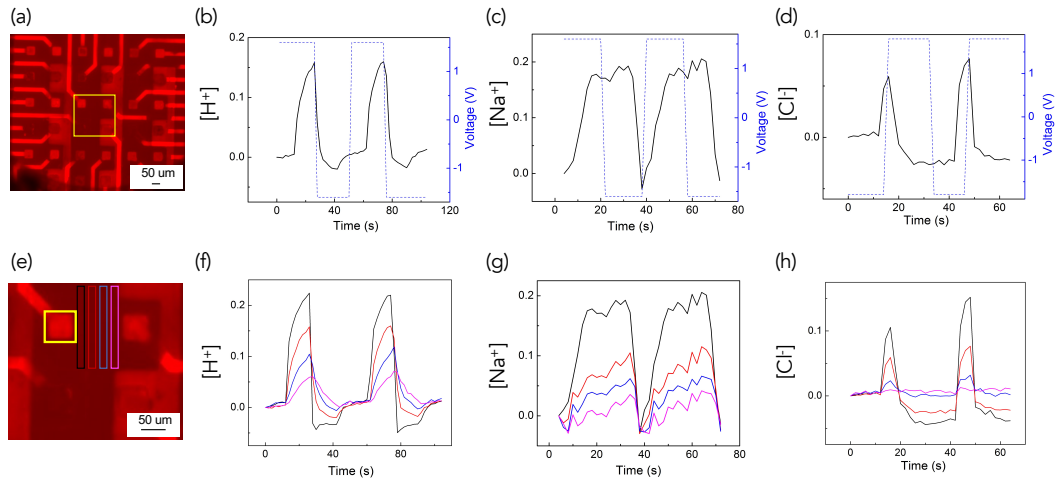


Figure 64 (a) Fluorescence image of the microelectrodes in target electrolyte, where the square highlights a group of microelectrodes that connected to different reservoirs. (b)  $[H^+]$  change following the applied voltage: when  $V1 = 1.6 V$ ,  $H^+$  was delivered to the target, inducing  $[H^+]$  going up, vice versa. (c) The  $[Na^+]$  change, following the applied voltage: when  $V2 = 1.6 V$ ,  $Na^+$  was delivered to the target, inducing  $[Na^+]$  going up, vice versa. (d) The  $[Cl^-]$  change, following the applied voltage: when  $V4 = -1.8 V$ ,  $Cl^-$  was delivered to the target, inducing  $[Cl^-]$  going up, vice versa. (e) Yellow square highlighted one microelectrode where we applied the voltage, and the four rectangles showed the areas whose fluorescence intensity was monitored. (f) The  $[H^+]$  change in the four rectangles highlighted in panel e following the protocol of panel b. (g) The  $[Na^+]$  change in the four rectangles

*highlighted in panel e following the protocol of c. (h) The [Cl<sup>-</sup>] change in the four rectangles highlighted in panel e following the same protocol of d.*

Each microelectrode was designed to function independently. So we also demonstrated spatial ion fluxes control by changing [H<sup>+</sup>] in different direction with two microelectrodes. In Figure 65, we applied 1.6 V and -1.6 V on two microelectrodes, their [H<sup>+</sup>] changes are in the opposite way, indicating a precise dynamic control. We also presented a video that shows the control of each H<sup>+</sup> microelectrode in sequence in Supporting Information.

It being the fact that biological processes are mostly self-regulated, and closed-loop control with feedback is a staple of most biological systems. Traditional control methods are difficult to be applied to the biological systems due to their complex dynamics and sensitivity to environmental changes.<sup>306</sup> Therefore, integrating the machine learning-based closed-loop control with the versatile multi-ion pump platform could introduce a powerful toolbox to further manipulate complex biological processes and will open up great possibilities for fundamental biological research. Here, we successfully demonstrated the automated closed-loop control of ion fluxes by machine learning using the multi-ion pump.

Figure 3a shows the general architecture of implemented online machine learning-based controller designed for the multi-ion pump system. By user choice, the ML-



controller is selecting one of the four sub-controllers<sup>307</sup> for controlling the predefined ions. The blue line is the reference signal, and the red line is the system output (i.e., fluorescence intensity). In Figure 3(b-d), we set different reference signals for different ions with blue lines. Then we applied voltage through the controller to the corresponding microelectrodes and made the output to track the reference signals. The results show that we're able to control the ion fluxes of  $H^+$ ,  $Na^+$ ,  $Cl^-$  following different patterns. In addition, the output of the controller applied to the multi-ion pump and the tracking error of the system are provided in Figure S2. The tracking performance of the multi-ion pump shows a promising response to the controller commands.

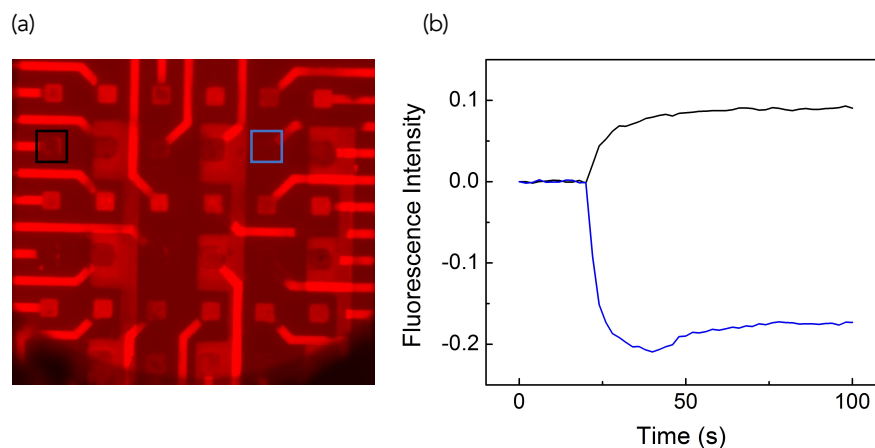


*Figure 65 (a) -1.6 V was applied to the microelectrode in the black square versus the auxiliary electrode while 1.6 V was applied to the one in the blue square. (b) The fluorescence intensity in the black square went up, indicating pH increase, and*

meanwhile, the fluorescence intensity in the blue square went down, indicating pH decrease.

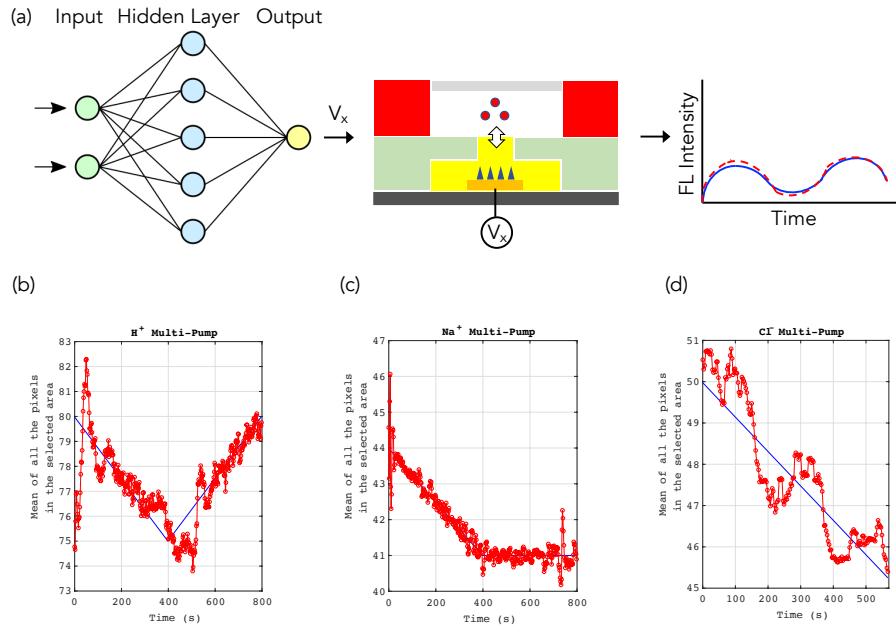


Figure 66 Multi-ion pump controlled by machine learning with desired targets.

### 6.3.3 Conclusion

In summary, we presented the first bioelectronic device capable of electrophoretic delivering 4 different ionic species simultaneously, including both cations and anions to date. The delivery sites are composed of 36 independent 50-um microelectrodes, which achieved different outputs with high spatiotemporal resolution. Additionally, we demonstrated the machine learning based closed-loop control of ion concentration in aqueous environment using the multi-ion pump, which is a mimic of the self-

regulated biological system. The control of multiple ionic species not only opens the chance to manipulate complicated physiological processes, but also provides a new tool for fundamental biological research.

#### 6.2.4 Experiment section:

*Device fabrication:* Multiple-ion pump platform was fabricated on 4-inch borosilicate glass wafer. Positive photoresist (S1813; Micro-Chem Corp.) was used to pattern Au contacts and traces followed by e-beam evaporation (10 nm Ti, 100 nm Au). Acetone and IPA are used for liftoff. Subsequently, S1813 photoresist is again used to selectively expose the Au contacts for nanoparticles electrodeposition (see “Electrodeposition” section). After electrodeposition, a 1.5  $\mu\text{m}$  thick insulating layer of parylene-C was deposited (Specialty Coating Systems Labcoater 2 system) in the presence of A174 adhesion promoter. The parylene was etched by an oxygen plasma with the regions over the electrodes and contact pads exposed, and the rest protected by SPR220 - 4.5 or SPR220 - 7 (Micro-Chem Corp). Prior to the deposition of ion channels, (3-glycidyloxypropyl) trimethoxysilane (GOPS) was deposited on the wafer to promote adhesion of the polymer. 5% GOPS was dispersed in ethanol and spin coated at 1000 rpm for 30 s and then baked at 110 C for 5 min.

A blend of 8 wt% polyvinyl alcohol (PVA) with 2 wt% polystyrene sulfonic acid (4:1 weight ratio) was thoroughly mixed by microwave and hotplate. The PVA:PSS solution was filtered by a cellulose esters (MCE) syringe filter with 0.8  $\mu\text{m}$  pore size and spin - coated on top of the wafer at 1500 rpm for 30 s and baked at 120 C for 2h,

yielding a film thickness of 2  $\mu\text{m}$ . A positive photoresist Dow SPR220 - 4.5 was spin - coated following protocols of the manufacturer. The PVA:PSS film was etched with an oxygen plasma with the desired pattern defined with SPR220-4.5 photoresist. A second 1.5  $\mu\text{m}$  coating of parylene was then deposited with the same protocol as above to insulate and protect the PVA:PSS film by only exposing the 36 microelectrodes. To promote adhesion between the parylene and the next polymer layer, PVA:Chitosan, GOPS was again deposited using the aforementioned process prior to PVA:Chitosan patterning. Chitosan is dissolved in 1% acetic acid and mixed with 10 wt% PVA (1:2 weight ratio) thoroughly with the help of microwave and hotplate. The PVA:Chitosan solution was filtered by a cellulose esters (MCE) syringe filter with 0.8  $\mu\text{m}$  pore size and spin - coated on top of the wafer at 1000 rpm for 5 s with 500 rpm/s ramp and then 4500 rpm for 30 s with 1500 rpm/s and baked at 80 C for 2h, yielding a film thickness of 2  $\mu\text{m}$ . The PVA:Chitosan film was etched with an oxygen plasma with the desired pattern defined with SPR220-4.5 photoresist. A third 1.5  $\mu\text{m}$  coating of parylene was deposited with the same protocol as above to insulate and protect all the polymers from the subsequent SU8 deposition. To promote adhesion between the parylene and SU8 photoresist, GOPS was again deposited using the aforementioned process prior to SU8 patterning. SU8 3025 was spun onto the wafer at 500 rpm for 5 s with 100 rpm/s ramp, 1000 rpm for 30 s with 300 rpm/s ramp, 3000 rpm for 1 s with 3000 rpm/s ramp. The patterned 70  $\mu\text{m}$  high SU8 photoresist formed the sidewalls of microfluidic channels for reservoir and target chambers. The third parylene insulation layer protecting the polymers was etched to

expose the electrode contacts in the reservoir and target channels using the same process as the previous parylene etch. Lastly, devices were diced from the wafers prior to sealing the microfluidics with single-sided microfluidic transparent diagnostic tape (3M 9964). Features in the tape layer were punched out with 1 mm and 2 mm diameter biopsy punches for exposing imaging area and fluidic inlets. The tapes were then aligned to SU8 features on the device and pressed to seal by hand. PDMS was also punched with the 1.5 mm diameter biopsy punches to provide support from the fluidic inlets.

*Electrodeposition:* All the electrodeposition is accomplished with a three-electrode configuration at room temperature with an Ag/AgCl pellet as reference electrode, and a platinum wire coil as counter electrode using an Autolab Potentiostat. The following procedure yields the most repeatable and stable results among several plating procedures tested.

*Pd NPs deposition:* 1 wt% PdNO<sub>3</sub> solution was diluted from 10 wt% PdNO<sub>3</sub> and used to electroplate the nanoparticles by applying a DC voltage of -0.3 V for 5s.

*Pt NPs deposition:* H<sub>2</sub>PtCl<sub>6</sub> was dissolved in DI-water by 1:1 and used to electroplate the nanoparticles by applying a DC voltage of -0.06 V for 8 s.

*AgCl NPs deposition:* 10 mM AgNO<sub>3</sub> in 0.1 M KNO<sub>3</sub> was used to deposit Ag nanoparticles followed by chlorinating Ag nanoparticles into AgCl nanoparticles. For microelectrodes, -0.2 V was applied for 5 s. For reference electrode and auxiliary electrode, -0.3 V was applied for 50 s. Then, we oxidize approximately Ag NPs to AgCl NPs by applying a constant anodic current (100 uA) for 10 s on Ag NPs in 50 mM KCl solution at room temperature. We observe a clear color change from silver white to dark grey indicating the formation of AgCl NPs.

*Microcontroller:* The modular microcontroller is a unique piece of equipment that can operate multiple electrochemical devices or a single electrochemical device with more than one working electrode. The modular aspect allows the microcontroller to scale from 8 to 64 channels by adding more stackable boards. The stackable board provides eight channels of circuits with the output range of +4V and input range of +1.65 uA. In addition, the modular microcontroller also offers an external control mode where it allows interfacing with external software such as a machine learning control algorithm. More detailed information of the microcontroller can be found here.<sup>308</sup>

*Fluorescence probes:* We used microscope based real-time imaging over the microelectrodes to monitor ion concentration change. We used 50 uM 5-(and-6)-Carboxy SNARF™-1 (SNARF, ThermoFisher) dispensed in 0.1M Tris buffer as a fluorescent indicator for H<sup>+</sup>, 50 uM CoroNa™ Green (CoroNa, ThermoFisher)

dispensed in 0.1M Tris buffer for Na<sup>+</sup>, 100 uM (N-(ethoxycarbonylmethyl)-6-methoxyquinolinium bromide) (MQAE, ThermoFisher) dispensed in 0.1M Tris buffer for Cl<sup>-</sup>, 100 uM PBFI, Tetraammonium Salt dispensed in 0.1M Tris buffer for K<sup>+</sup>. The fluorescent probe solution was flowed into the target chamber via a sealed microfluidic channel. Thereafter, the device was monitored by BZ-X710 fluorescence microscope with 10 x Nikon objective. Different filters are selected by the ion we're interested to image: TxRed (ex: 560/40 nm, em: 630/75 nm) for SNARF, GFP for CoroNa (ex: 502/30 nm, em: 520/36 nm), customized (ex: 340/40 nm, em: 510/80 nm) for PBFI, and DAPI (ex: 377/50 nm, em: 447/60 nm) for MQAE. Imaging data were collected every 2 s in real time. Data were analyzed using ImageJ software.

## 7. Outlook

Bioelectronics has joined the toolbox of health care for many decades and played a critical role in clinical settings with cardiac pacemakers, brain implants, and more recently vagus nerve stimulation. The emergence of soft, water-rich materials such as polyelectrolyte polymers and hydrogels provide an opportunity for better integration of bioelectronic devices with the wet and soft biological tissue. The ionic conductivity and ability to deliver small biochemicals of hydrogels opens new avenues for device-tissue communication. More importantly, this communication extends limited to electrically excitable cells but extended to non-excitable cells, such as stem cells to guide differentiation<sup>298, 299</sup> and skin cells for improved wound healing.<sup>300 301</sup>

Ion conducting materials, specifically, polyelectrolytes that are selectively permeable to cations or anions, play a critical role in iontronic devices. However, the study on ionic conducting materials is much less compared to that of the electron conducting materials. Polyelectrolyte hydrogels are intrinsic ionic conductors, biocompatible and biodegradable, and appear as the core of iontronic devices for eco-friendly biosensors, implantable/wearable devices, as well as biological information processors.

Although the outlook of iontronic devices is widely open, many challenges have yet to be tackled. One is the under developed ion conducting materials. The second is the fabrication of ion conducting materials and their integration with electrical contacts in electronic devices. To this end, microfabrication of photo-crosslinkable hydrogels<sup>309</sup>



using conventional photolithography techniques have been reported to be a feasible method. Covalent chemical bonding between the hydrogel and the electrodes is also shown to improve hydrogel adhesion and reduces delamination.<sup>310</sup> Other challenges include the long term stability and batch-to-batch reproducibility for the translation to clinical settings.

Nonetheless, given the rapid development for those problems as well as the tremendous potential benefits, iontronic devices deserve to be explored more as new tools for human-machine interface in the near future.

## 8. Reference

1. T. Someya, Z. Bao and G. G. Malliaras, *Nature*, 2016, **540**, 379.
2. D. T. Simon, E. O. Gabrielson, K. Tybrandt and M. Berggren, *Chemical Reviews*, 2016, **116**, 13009-13041.
3. M. Jia, H. Dechiruji, J. Selberg, P. Pansodtee, J. Mathews, C. Wu, M. Levin, M. Teodorescu and M. Rolandi, *Apl Mater*, 2020, **8**, 091106.
4. M. Bresadola, *Brain Research Bulletin*, 1998, **46**, 367-380.
5. G. Finkelstein, *Emil du Bois-Reymond: neuroscience, self, and society in nineteenth-century Germany*, MIT Press, 2013.
6. M. Brignole, C. Menozzi, A. Moya, D. Andresen, J. J. Blanc, A. D. Krahn, W. Wieling, X. Beiras, J. C. Deharo and V. Russo, *Circulation*, 2012, **125**, 2566-2571.
7. A. L. Benabid, *Curr. Opin. Neurobiol.*, 2003, **13**, 696-706.
8. T. Dvir, B. P. Timko, M. D. Brigham, S. R. Naik, S. S. Karajanagi, O. Levy, H. Jin, K. K. Parker, R. Langer and D. S. Kohane, *Nature nanotechnology*, 2011, **6**, 720.
9. K. Famm, B. Litt, K. J. Tracey, E. S. Boyden and M. Slaoui, *Nature*, 2013, **496**, 159.
10. C. S. Wood, M. R. Thomas, J. Budd, T. P. Mashamba-Thompson, K. Herbst, D. Pillay, R. W. Peeling, A. M. Johnson, R. A. McKendry and M. M. Stevens, *Nature*, 2019, **566**, 467.
11. J.-W. Jeong, G. Shin, S. I. Park, K. J. Yu, L. Xu and J. A. Rogers, *Neuron*, 2015, **86**, 175-186.
12. H. Yuk, B. Lu and X. Zhao, *Chemical Society Reviews*, 2019, **48**, 1642-1667.
13. S. J. Head, M. M. Mokhles, R. L. Osnabrugge, P. Pibarot, M. J. Mack, J. J. Takkenberg, A. J. Bogers and A. P. Kappetein, *European heart journal*, 2012, **33**, 1518-1529.
14. E. Caló and V. V. Khutoryanskiy, *European Polymer Journal*, 2015, **65**, 252-267.

15. N. A. Peppas, J. Z. Hilt, A. Khademhosseini and R. Langer, *Advanced materials*, 2006, **18**, 1345-1360.
16. A. Khademhosseini and R. Langer, *Biomaterials*, 2007, **28**, 5087-5092.
17. H. Chun and T. D. Chung, *Annual Review of Analytical Chemistry*, 2015, **8**, 441-462.
18. J. Rivnay, S. Inal, A. Salleo, R. M. Owens, M. Berggren and G. G. Malliaras, *Nature Reviews Materials*, 2018, **3**, 1-14.
19. H. Siringhaus, *Advanced materials*, 2014, **26**, 1319-1335.
20. M. Seitanidou, R. Blomgran, G. Pushpamithran, M. Berggren and D. T. Simon, *Advanced healthcare materials*, 2019, **8**, 1900813.
21. W. Guan, R. Fan and M. A. Reed, *Nature communications*, 2011, **2**, 1-8.
22. E. O. Gabrielsson, K. Tybrandt and M. Berggren, *Lab on a Chip*, 2012, **12**, 2507-2513.
23. V. S. Meka, M. K. Sing, M. R. Pichika, S. R. Nali, V. R. Kolapalli and P. Kesharwani, *Drug discovery today*, 2017, **22**, 1697-1706.
24. T. Arbring Sjöström, M. Berggren, E. O. Gabrielsson, P. Janson, D. J. Poxson, M. Seitanidou and D. T. Simon, *Advanced Materials Technologies*, 2018, **3**, 1700360.
25. J. Selberg, M. Jafari, J. Mathews, M. Jia, P. Pansodtee, H. Dechiraju, C. Wu, S. Cordero, A. Flora and N. Yonas, *Advanced Intelligent Systems*, 2000140.
26. A. Williamson, J. Rivnay, L. Kergoat, A. Jonsson, S. Inal, I. Uguz, M. Ferro, A. Ivanov, T. A. Sjöström and D. T. Simon, *Advanced Materials*, 2015, **27**, 3138-3144.
27. D. T. Simon, S. Kurup, K. C. Larsson, R. Hori, K. Tybrandt, M. Goiny, E. W. Jager, M. Berggren, B. Canlon and A. Richter-Dahlfors, *Nature materials*, 2009, **8**, 742-746.
28. A. Jonsson, Z. Song, D. Nilsson, B. A. Meyerson, D. T. Simon, B. Linderoth and M. Berggren, *Science Advances*, 2015, **1**, e1500039.
29. D. J. Poxson, M. Karady, R. Gabrielsson, A. Y. Alkattan, A. Gustavsson, S. M. Doyle, S. Robert, K. Ljung, M. Grebe and D. T. Simon, *Proceedings of the National Academy of Sciences*, 2017, **114**, 4597-4602.

30. S.-M. Lim, H. Yoo, M.-A. Oh, S. H. Han, H.-R. Lee, T. D. Chung, Y.-C. Joo and J.-Y. Sun, *Proceedings of the National Academy of Sciences*, 2019, **116**, 13807-13815.
31. T. Kajisa and T. Sakata, *Science and Technology of Advanced Materials*, 2017, **18**, 26-33.
32. M. Seitanidou, K. Tybrandt, M. Berggren and D. T. Simon, *Lab on a Chip*, 2019, **19**, 1427-1435.
33. S. F. Cogan, *Annu. Rev. Biomed. Eng.*, 2008, **10**, 275-309.
34. T. Rose and L. Robblee, *IEEE Transactions on Biomedical Engineering*, 1990, **37**, 1118-1120.
35. A. B. Frazier, D. P. O'Brien and M. G. Allen, 1993.
36. D. Borkholder, J. Bao, N. Maluf, E. Perl and G. Kovacs, *Journal of neuroscience methods*, 1997, **77**, 61-66.
37. S. F. Cogan, P. R. Troyk, J. Ehrlich and T. D. Plante, *IEEE Transactions on Biomedical Engineering*, 2005, **52**, 1612-1614.
38. B. S. Wilson, C. C. Finley, D. T. Lawson, R. D. Wolford, D. K. Eddington and W. M. Rabinowitz, *Nature*, 1991, **352**, 236.
39. M. S. Humayun, E. de Juan Jr, J. D. Weiland, G. Dagnelie, S. Katona, R. Greenberg and S. Suzuki, *Vision research*, 1999, **39**, 2569-2576.
40. J.-M. Seo, S. J. Kim, H. Chung, E. T. Kim, H. G. Yu and Y. S. Yu, *Materials Science and Engineering: C*, 2004, **24**, 185-189.
41. V. S. Polikov, P. A. Tresco and W. M. Reichert, *Journal of neuroscience methods*, 2005, **148**, 1-18.
42. Z. Aqrawe, J. Montgomery, J. Travas-Sejdic and D. Svirskis, *Sensors and Actuators B: Chemical*, 2018, **257**, 753-765.
43. M. Wang, G. Mi, D. Shi, N. Bassous, D. Hickey and T. J. Webster, *Advanced Functional Materials*, 2018, **28**, 1700905.
44. D. R. Merrill, M. Bikson and J. G. Jefferys, *Journal of neuroscience methods*, 2005, **141**, 171-198.
45. S. Arcot Desai, J. D. Rolston, L. Guo and S. M. Potter, *Frontiers in neuroengineering*, 2010, **3**, 5.

46. A. Feltham and M. Spiro, *Chemical Reviews*, 1971, **71**, 177-193.
47. C. A. Marrese, *Analytical chemistry*, 1987, **59**, 217-218.
48. S. Inal, J. Rivnay, A.-O. Suiu, G. G. Malliaras and I. McCulloch, *Accounts of chemical research*, 2018, **51**, 1368-1376.
49. T. F. Akbar, C. Tondera and I. Minev, in *Neural Interface Engineering*, Springer, 2020, pp. 237-265.
50. T. Someya, Z. Bao and G. G. Malliaras, *Nature*, 2016, **540**, 379-385.
51. M. Jia and M. Rolandi, *Advanced healthcare materials*, 2020, **9**, 1901372.
52. J. Yi, G. Choe, J. Park and J. Y. Lee, *Polymer Journal*, 2020, 1-15.
53. R. Aversa, R. V. Petrescu, A. Apicella and F. I. Petrescu, *American Journal of Biochemistry and Biotechnology*, 2016, **13**, 34-41.
54. D. Khodagholy, J. N. Gelinas, T. Thesen, W. Doyle, O. Devinsky, G. G. Malliaras and G. Buzsáki, *Nature neuroscience*, 2015, **18**, 310.
55. R. Chen, A. Canales and P. Anikeeva, *Nature Reviews Materials*, 2017, **2**, 1-16.
56. A. Kotwal and C. E. Schmidt, *Biomaterials*, 2001, **22**, 1055-1064.
57. X. Cui, J. Wiler, M. Dzaman, R. A. Altschuler and D. C. Martin, *Biomaterials*, 2003, **24**, 777-787.
58. K. Wang, H. A. Fishman, H. Dai and J. S. Harris, *Nano letters*, 2006, **6**, 2043-2048.
59. E. W. Keefer, B. R. Botterman, M. I. Romero, A. F. Rossi and G. W. Gross, *Nature nanotechnology*, 2008, **3**, 434.
60. N. K. Guimard, N. Gomez and C. E. Schmidt, *Progress in polymer science*, 2007, **32**, 876-921.
61. B. Guo and P. X. Ma, *Biomacromolecules*, 2018, **19**, 1764-1782.
62. T. Nezakati, A. Seifalian, A. Tan and A. M. Seifalian, *Chemical reviews*, 2018, **118**, 6766-6843.
63. X. Cui, J. F. Hetke, J. A. Wiler, D. J. Anderson and D. C. Martin, *Sensors and Actuators A: Physical*, 2001, **93**, 8-18.

64. M. R. Abidian, J. M. Corey, D. R. Kipke and D. C. Martin, *small*, 2010, **6**, 421-429.
65. Z. Aqrawe, B. Wright, N. Patel, Y. Vyas, J. Malmstrom, J. M. Montgomery, D. Williams, J. Travas-Sejdic and D. Svirskis, *Sensors and Actuators B: Chemical*, 2019, **281**, 549-560.
66. R. Green, P. Matteucci, R. Hassarati, B. Giraud, C. Dodds, S. Chen, P. Byrnes-Preston, G. Suaning, L. Poole-Warren and N. Lovell, *Journal of neural engineering*, 2013, **10**, 016009.
67. M. Berggren and A. Richter-Dahlfors, *Advanced Materials*, 2007, **19**, 3201-3213.
68. L. Lu, X. Fu, Y. Liew, Y. Zhang, S. Zhao, Z. Xu, J. Zhao, D. Li, Q. Li and G. B. Stanley, *Nano letters*, 2019, **19**, 1577-1586.
69. S. Bosi, A. Fabbro, C. Cantarutti, M. Mihajlovic, L. Ballerini and M. Prato, *Carbon*, 2016, **97**, 87-91.
70. S. K. Rastogi, A. Kalmykov, N. Johnson and T. Cohen-Karni, *Journal of Materials Chemistry B*, 2018, **6**, 7159-7178.
71. X. Luo, C. L. Weaver, D. D. Zhou, R. Greenberg and X. T. Cui, *Biomaterials*, 2011, **32**, 5551-5557.
72. S. Smart, A. Cassady, G. Lu and D. Martin, *Carbon*, 2006, **44**, 1034-1047.
73. S. Kim, L. K. Jang, M. Jang, S. Lee, J. G. Hardy and J. Y. Lee, *ACS applied materials & interfaces*, 2018, **10**, 33032-33042.
74. M. R. Abidian and D. C. Martin, *Advanced Functional Materials*, 2009, **19**, 573-585.
75. X. T. Cui and D. D. Zhou, *IEEE Transactions on Neural Systems and Rehabilitation Engineering*, 2007, **15**, 502-508.
76. Y. Lu, T. Li, X. Zhao, M. Li, Y. Cao, H. Yang and Y. Y. Duan, *Biomaterials*, 2010, **31**, 5169-5181.
77. Z. Aqrawe, J. Montgomery, J. Travas-Sejdic and D. Svirskis, *Trends in biotechnology*, 2017, **35**, 93-95.
78. W. R. Stauffer and X. T. Cui, *Biomaterials*, 2006, **27**, 2405-2413.

79. R. A. Green, N. H. Lovell and L. A. Poole-Warren, *Acta biomaterialia*, 2010, **6**, 63-71.
80. F. Lim and A. M. Sun, *Science*, 1980, **210**, 908-910.
81. I. Yannas, E. Lee, D. P. Orgill, E. Skrabut and G. F. Murphy, *Proceedings of the National Academy of Sciences*, 1989, **86**, 933-937.
82. N. A. Peppas, *Hydrogels in medicine and pharmacy: fundamentals*, CRC press, 2019.
83. D. Seliktar, *Science*, 2012, **336**, 1124-1128.
84. J. A. Tuszynski, in *Brain and Human Body Modeling: Computational Human Modeling at EMBC 2018*, eds. S. Makarov, M. Horner and G. Noetscher, Springer International Publishing, Cham, 2019, DOI: 10.1007/978-3-030-21293-3\_11, pp. 195-208.
85. A. Zhang and C. M. Lieber, *Chemical Reviews*, 2016, **116**, 215-257.
86. S. Q. Liu, C. Yang, Y. Huang, X. Ding, Y. Li, W. M. Fan, J. L. Hedrick and Y. Y. Yang, *Advanced Materials*, 2012, **24**, 6484-6489.
87. M. Czerner, L. S. Fellay, M. P. Suárez, P. M. Frontini and L. A. Fasce, *Procedia Materials Science*, 2015, **8**, 287-296.
88. S. Cascone and G. Lamberti, *International Journal of Pharmaceutics*, 2020, **573**, 118803.
89. E. S. Place, J. H. George, C. K. Williams and M. M. Stevens, *Chemical society reviews*, 2009, **38**, 1139-1151.
90. M. Sasaki, B. C. Karikkineth, K. Nagamine, H. Kaji, K. Torimitsu and M. Nishizawa, *Advanced healthcare materials*, 2014, **3**, 1919-1927.
91. S. Zhao, P. Tseng, J. Grasman, Y. Wang, W. Li, B. Napier, B. Yavuz, Y. Chen, L. Howell and J. Rincon, *Advanced Materials*, 2018, **30**, 1800598.
92. A. Guiseppi-Elie, *Biomaterials*, 2010, **31**, 2701-2716.
93. Z. Jia, Y. Zeng, P. Tang, D. Gan, W. Xing, Y. Hou, K. Wang, C. Xie and X. Lu, *Chemistry of Materials*, 2019, **31**, 5625-5632.
94. L. Han, K. Liu, M. Wang, K. Wang, L. Fang, H. Chen, J. Zhou and X. Lu, *Advanced Functional Materials*, 2018, **28**, 1704195.

95. L. Han, X. Lu, M. Wang, D. Gan, W. Deng, K. Wang, L. Fang, K. Liu, C. W. Chan and Y. Tang, *Small*, 2017, **13**, 1601916.
96. L. Han, L. Yan, M. Wang, K. Wang, L. Fang, J. Zhou, J. Fang, F. Ren and X. Lu, *Chemistry of Materials*, 2018, **30**, 5561-5572.
97. Z. Shi, X. Gao, M. W. Ullah, S. Li, Q. Wang and G. Yang, *Biomaterials*, 2016, **111**, 40-54.
98. K. B. Rufato, J. P. Galdino, K. S. Ody, A. G.B. Pereira, E. Corradini, A. F. Martins, A. T. Paulino, A. R. Fajardo, F. A. Aouada, F. A. La Porta, A. F. Rubira and E. C. Muniz, in *Hydrogels - Smart Materials for Biomedical Applications*, 2019, DOI: 10.5772/intechopen.81811.
99. J. L. Drury and D. J. Mooney, *Biomaterials*, 2003, **24**, 4337-4351.
100. C. Wang, T. Yokota and T. Someya, *Chemical Reviews*, 2021.
101. H. Tan and K. G. Marra, *Materials*, 2010, **3**, 1746-1767.
102. C.-J. Lee, H. Wu, Y. Hu, M. Young, H. Wang, D. Lynch, F. Xu, H. Cong and G. Cheng, *ACS Applied Materials & Interfaces*, 2018, **10**, 5845-5852.
103. Y. Guo, X. Zhou, Q. Tang, H. Bao, G. Wang and P. Saha, *Journal of Materials Chemistry A*, 2016, **4**, 8769-8776.
104. P. G. Bruce, *Solid state electrochemistry*, Cambridge university press, 1997.
105. B. B. Owens and G. R. Argue, *Science*, 1967, **157**, 308-310.
106. Y.-F. Y. Yao and J. Kummer, *Journal of Inorganic and Nuclear Chemistry*, 1967, **29**, 2453-2475.
107. K. A. Mauritz and R. B. Moore, *Chemical reviews*, 2004, **104**, 4535-4586.
108. B. D. Paulsen, K. Tybrandt, E. Stavrinidou and J. Rivnay, *Nature materials*, 2020, **19**, 13-26.
109. D. J. Poxson, E. O. Gabrielsson, A. Bonisoli, U. Linderhed, T. Abrahamsson, I. Matthiesen, K. Tybrandt, M. Berggren and D. T. Simon, *ACS Applied Materials & Interfaces*, 2019, **11**, 14200-14207.
110. T. M. W. J. Bandara and B. E. Mellander, in *Ionic Liquids: Theory, Properties, New Approaches*, 2011, DOI: 10.5772/15183.



111. M. Barrande, R. Bouchet and R. Denoyel, *Analytical chemistry*, 2007, **79**, 9115-9121.
112. W. Barros Jr, *Physical Review E*, 2019, **99**, 052501.
113. J.-H. Cao, B.-K. Zhu and Y.-Y. Xu, *Journal of membrane science*, 2006, **281**, 446-453.
114. K. D. Kreuer, A. Rabenau and W. Weppner, *Angewandte Chemie International Edition in English*, 1982, **21**, 208-209.
115. M. W. Tsang and S. Holdcroft, in *Polymers for a Sustainable Environment and Green Energy*, 2012, vol. 10, p. 651.
116. N. Agmon, *Chemical Physics Letters*, 1995, **244**, 456-462.
117. H. J. Morowitz, *American Journal of Physiology-Regulatory, Integrative and Comparative Physiology*, 1978, **235**, R99-R114.
118. D. Dong, W. Zhang, A. C. Van Duin and D. Bedrov, *The journal of physical chemistry letters*, 2018, **9**, 825-829.
119. T. Ogawa, K. Kamiguchi, T. Tamaki, H. Imai and T. Yamaguchi, *Analytical chemistry*, 2014, **86**, 9362-9366.
120. T. Miyake and M. Rolandi, *Journal of Physics: Condensed Matter*, 2015, **28**, 023001.
121. C. A. Wraight, *Biochimica et Biophysica Acta (BBA)-Bioenergetics*, 2006, **1757**, 886-912.
122. G. A. Luduena, T. D. Kühne and D. Sebastiani, *Chemistry of Materials*, 2011, **23**, 1424-1429.
123. G. Bardelmeyer, *Biopolymers: Original Research on Biomolecules*, 1973, **12**, 2289-2302.
124. Y. X. Deng, E. Josberger, J. H. Jin, A. F. Roudsari, B. A. Helms, C. Zhong, M. P. Anantram and M. Rolandi, *Sci Rep-Uk*, 2015, **5**.
125. T. Miyake and M. Rolandi, *J Phys-Condens Mat*, 2016, **28**.
126. F. H. Muhammad, R. H. Y. Subban and T. Winie, *Materials Today: Proceedings*, 2017, **4**, 5130-5137.

127. G. Ruano, J. I. Iribarren, M. M. Pérez-Madrigal, J. Torras and C. Alemán, *Polymers*, 2021, **13**, 1337.
128. X. Strakosas, J. Selberg, P. Pansodtee, N. Yonas, P. Manapongpun, M. Teodorescu and M. Rolandi, *Scientific reports*, 2019, **9**, 1-7.
129. J. Ma and Y. Sahai, *Carbohydrate Polymers*, 2013, **92**, 955-975.
130. G. Wu, J. Zhang, X. Wan, Y. Yang and S. Jiang, *Journal of Materials Chemistry C*, 2014, **2**, 6249-6255.
131. M. Amit, S. Roy, Y. Deng, E. Josberger, M. Rolandi and N. Ashkenasy, *ACS applied materials & interfaces*, 2018, **10**, 1933-1938.
132. C. Gabrielli, P. Grand, A. Lasia and H. Perrot, *Journal of The Electrochemical Society*, 2004, **151**, A1925.
133. T. Miyake, E. E. Josberger, S. Keene, Y. Deng and M. Rolandi, *APL Materials*, 2015, **3**, 014906.
134. T. E. DeCoursey, *Physiological Reviews*, 2003, **83**, 1067-1067.
135. P. Mitchell, *Biol Rev*, 1966, **41**, 445-&.
136. J. K. Lanyi, *Annual Review of Physiology*, 2004, **66**, 665-688.
137. D. Busath and G. Szabo, *Nature*, 1981, **294**, 371-373.
138. S. M. Smith, D. Morgan, B. Musset, V. V. Cherny, A. R. Place, J. W. Hastings and T. E. Decoursey, *Proc Natl Acad Sci U S A*, 2011, **108**, 18162-18167.
139. H. J. Morowitz, *Am J Physiol*, 1978, **235**, R99-R114.
140. S. Cukierman, *Biochim Biophys Acta*, 2006, **1757**, 876-885.
141. G. H. Bardelmeyer, *Biopolymers*, 1973, **12**, 2289-2302.
142. J. E. Algie, J. G. Downes and B. H. Mackay, *Textile Research Journal*, 1960, **30**, 432-434.
143. J. T. Robinson, J. J. Pietron, B. Blue, F. K. Perkins, E. Josberger, Y. Deng and M. Rolandi, *Journal of Materials Chemistry C*, 2017, **5**, 11083-11091.

144. J. Wünsche, Y. Deng, P. Kumar, E. Di Mauro, E. Josberger, J. Sayago, A. Pezzella, F. Soavi, F. Cicoira, M. Rolandi and C. Santato, *Chemistry of Materials*, 2015, **27**, 436-442.
145. N. Amdursky, X. Wang, P. Meredith, D. D. Bradley and M. M. Stevens, *Adv Mater*, 2016, **28**, 2692-2698.
146. D. D. Ordinario, L. Phan, W. G. t. Walkup, J. M. Jocson, E. Karshalev, N. Husken and A. A. Gorodetsky, *Nat Chem*, 2014, **6**, 596-602.
147. R. Kautz, D. D. Ordinario, V. Tyagi, P. Patel, T. N. Nguyen and A. A. Gorodetsky, *Advanced Materials*, 2018, **30**, 1704917.
148. M. Eigen and L. Demaeyer, *Proceedings of the Royal Society of London Series a-Mathematical and Physical Sciences*, 1958, **247**, 505-533.
149. Y. Deng, B. A. Helms and M. Rolandi, *Journal of Polymer Science Part A: Polymer Chemistry*, 2015, **53**, 211-214.
150. Y. Deng, E. Josberger, J. Jin, A. F. Roudsari, A. F. Rousdari, B. A. Helms, C. Zhong, M. P. Anantram and M. Rolandi, *Sci Rep*, 2013, **3**, 2481.
151. Y. Sone, P. Ekdunge and D. Simonsson, *Journal of the Electrochemical Society*, 1996, **143**, 1254-1259.
152. E. E. Josberger, P. Hassanzadeh, Y. X. Deng, J. Sohn, M. J. Rego, C. T. Amemiya and M. Rolandi, *Sci Adv*, 2016, **2**.
153. J. L. Funderburgh, *Glycobiology*, 2000, **10**, 951-958.
154. V. H. Pomin, *Int J Biol Macromol*, 2015, **72**, 282-289.
155. L. Fu, X. Sun, W. He, C. Cai, A. Onishi, F. Zhang, R. J. Linhardt and Z. Liu, *Glycobiology*, 2016, **26**, 693-700.
156. A. Weyers, B. Yang, K. Solakyildirim, V. Yee, L. Li, F. Zhang and R. J. Linhardt, *FEBS J*, 2013, **280**, 2285-2293.
157. J. F. Nagle, M. Mille and H. J. Morowitz, *The Journal of Chemical Physics*, 1980, **72**, 3959-3971.
158. A. Dorfman and R. Matalon, *Proc Natl Acad Sci U S A*, 1976, **73**, 630-637.
159. N. S. Gandhi and R. L. Mancera, *Chem Biol Drug Des*, 2008, **72**, 455-482.
160. A. B. Souza-Fernandes, P. Pelosi and P. R. M. Rocco, *Crit Care*, 2006, **10**.

161. P. D. Smith, V. J. Coulson-Thomas, S. Foscarin, J. C. Kwok and J. W. Fawcett, *Exp Neurol*, 2015, **274**, 100-114.
162. N. Afratis, C. Gialeli, D. Nikitovic, T. Tsegenidis, E. Karousou, A. D. Theocharis, M. S. Pavao, G. N. Tzanakakis and N. K. Karamanos, *FEBS J*, 2012, **279**, 1177-1197.
163. Z. Hemmatian, T. Miyake, Y. Deng, E. E. Josberger, S. Keene, R. Kautz, C. Zhong, J. Jin and M. Rolandi, *J. Mater. Chem. C*, 2015, **3**, 6407-6412.
164. Y. Deng, T. Miyake, S. Keene, E. E. Josberger and M. Rolandi, *Sci Rep*, 2016, **6**, 24080.
165. X. Strakosas, J. Selberg, Z. Hemmatian and M. Rolandi, *Adv Sci (Weinh)*, 2017, **4**, 1600527.
166. M. Amit, S. Roy, Y. Deng, E. Josberger, M. Rolandi and N. Ashkenasy, *ACS Appl Mater Interfaces*, 2018, **10**, 1933-1938.
167. M. Yamauchi, H. Kobayashi and H. Kitagawa, *Chemphyschem*, 2009, **10**, 2566-2576.
168. Y. Zhang, E. P. Go, H. Jiang and H. Desaire, *J Am Soc Mass Spectrom*, 2005, **16**, 1827-1839.
169. W. Park and K. Na, *Biotechnology and Bioprocess Engineering*, 2009, **14**, 668-674.
170. Y. H. Liao, S. A. Jones, B. Forbes, G. P. Martin and M. B. Brown, *Drug Deliv*, 2005, **12**, 327-342.
171. P. L. Chandran and F. Horkay, *Acta Biomater*, 2012, **8**, 3-12.
172. S. B. Rienecker, A. B. Mostert, G. Schenk, G. R. Hanson and P. Meredith, *J Phys Chem B*, 2015, **119**, 14994-15000.
173. C. Zhong, Y. Deng, A. F. Roudsari, A. Kapetanovic, M. P. Anantram and M. Rolandi, *Nat Commun*, 2011, **2**, 476.
174. J. Selberg, M. Jia and M. Rolandi, *PloS one*, 2019, **14**.
175. A. J. Kalmijn, in *Electroreceptors and Other Specialized Receptors in Lower Vertebrates*, Springer, 1974, pp. 147-200.
176. K. C. Newton, A. B. Gill and S. M. Kajiura, *Journal of fish biology*, 2019, **95**, 135-154.

177. R. Kempster, I. McCarthy and S. Collin, *Journal of Fish Biology*, 2012, **80**, 2055-2088.
178. R. Murray and W. Potts, *Comparative Biochemistry and Physiology*, 1961, **2**, 65-&.
179. M. Djabourov, *Contemporary Physics*, 1988, **29**, 273-297.
180. X. Zhang, K. Xia, L. Lin, F. Zhang, Y. Yu, K. St. Ange, X. Han, E. Edsinger, J. Sohn and R. J. Linhardt, *ACS chemical biology*, 2018, **13**, 1677-1685.
181. S. Bureekaew, S. Horike, M. Higuchi, M. Mizuno, T. Kawamura, D. Tanaka, N. Yanai and S. Kitagawa, in *Materials For Sustainable Energy: A Collection of Peer-Reviewed Research and Review Articles from Nature Publishing Group*, World Scientific, 2011, pp. 232-237.
182. Q.-H. Guo, M. Jia, Z. Liu, Y. Qiu, H. Chen, D. Shen, X. Zhang, Q. Tu, M. R. Ryder and H. Chen, *Journal of the American Chemical Society*, 2020, **142**, 6180-6187.
183. E. E. Josberger, P. Hassanzadeh, Y. Deng, J. Sohn, M. J. Rego, C. T. Amemiya and M. Rolandi, *Science advances*, 2016, **2**, e1600112.
184. J. Haas, M. V. R. Kumar, G. Borchard, U. Bakowsky and C.-M. Lehr, *Aaps Pharmscitech*, 2005, **6**, E22-E30.
185. M. Phillips, W. J. Tang, M. Robinson, D. O. Daza, K. Hassan, V. Leppert, L. S. Hirst and C. T. Amemiya, *Current Biology*, 2020, **30**, R1254-R1255.
186. J. Maier, *Materials for Sustainable Energy: A Collection of Peer-Reviewed Research and Review Articles from Nature Publishing Group*, 2011, 160-170.
187. S. Harm, A.-K. Hatz, I. Moudrakovski, R. Eger, A. Kuhn, C. Hoch and B. V. Lotsch, *Chemistry of Materials*, 2019, **31**, 1280-1288.
188. A. Harder, V. Walhorn, T. Dierks, X. Fernández-Busquets and D. Anselmetti, *Biophysical journal*, 2010, **99**, 3498-3504.
189. M. Phillips, A. Wheeler, M. J. Robinson, V. Leppert, M. Jia, M. Rolandi, L. S. Hirst and C. T. Amemiya, *bioRxiv*, 2021, 2021.2001.2004.425255.
190. H. M. Colquhoun and D. J. Williams, *Accounts of chemical research*, 2000, **33**, 189-198.
191. T. Hoang, J. W. Lauher and F. W. Fowler, *Journal of the American Chemical Society*, 2002, **124**, 10656-10657.

192. Z. Gadjourova, Y. G. Andreev, D. P. Tunstall and P. G. Bruce, *Nature*, 2001, **412**, 520-523.
193. F. Croce, G. Appetecchi, L. Persi and B. Scrosati, *Nature*, 1998, **394**, 456-458.
194. M. A. Hickner, H. Ghassemi, Y. S. Kim, B. R. Einsla and J. E. McGrath, *Chemical reviews*, 2004, **104**, 4587-4612.
195. S. Yamada, N. Uematsu and K. Yamashita, *Journal of the American Chemical Society*, 2007, **129**, 12100-12101.
196. Q.-H. Guo, Z. Liu, P. Li, D. Shen, Y. Xu, M. R. Ryder, H. Chen, C. L. Stern, C. D. Malliakas and X. Zhang, *Chem*, 2019, **5**, 2353-2364.
197. K. J. Wallace, W. J. Belcher, D. R. Turner, K. F. Syed and J. W. Steed, *Journal of the American Chemical Society*, 2003, **125**, 9699-9715.
198. S. Yamada and Y. Tokugawa, *Journal of the American Chemical Society*, 2009, **131**, 2098-2099.
199. J. Selberg, M. Jia and M. Rolandi, *PLoS One*, 2019, **14**, e0202713.
200. J. F. Nagle and H. Morowitz, *Proceedings of the National Academy of Sciences*, 1978, **75**, 298-302.
201. Q.-H. Guo, M. Jia, Z. Liu, Y. Qiu, H. Chen, D. Shen, X. Zhang, Q. Tu, M. R. Ryder and H. Chen, *Journal of the American Chemical Society*, 2020.
202. K. Sato, Y. Itoh and T. Aida, *Journal of the American Chemical Society*, 2011, **133**, 13767-13769.
203. A. J. Hesel, A. L. Brown, K. Yamato, W. Feng, L. Yuan, A. J. Clements, S. V. Harding, G. Szabo, Z. Shao and B. Gong, *Journal of the American Chemical Society*, 2008, **130**, 15784-15785.
204. N. Kameta, M. Masuda and T. Shimizu, *Chemical Communications*, 2015, **51**, 6816-6819.
205. Y. Xu, T. Wang, Z. He, A. Zhong, W. Yu, B. Shi and K. Huang, *Polymer Chemistry*, 2016, **7**, 7408-7415.
206. N. Kameta, J. Dong and H. Yui, *Small*, 2018, **14**, 1800030.
207. T. Shimizu, W. Ding and N. Kameta, *Chemical reviews*, 2020, **120**, 2347-2407.

208. D. W. Balkenende, C. A. Monnier, G. L. Fiore and C. Weder, *Nature communications*, 2016, **7**, 1-9.
209. K. Dai, J. R. Fores, C. Wanzke, B. Winkeljann, A. M. Bergmann, O. Lieleg and J. Boekhoven, *Journal of the American Chemical Society*, 2020, **142**, 14142-14149.
210. M. J. Strauss, A. M. Evans, I. Castano, R. L. Li and W. R. Dichtel, *Chemical science*, 2020, **11**, 1957-1963.
211. C. Sun, M. Shen, A. D. Chavez, A. M. Evans, X. Liu, B. Harutyunyan, N. C. Flanders, M. C. Hersam, M. J. Bedzyk and M. O. de la Cruz, *Proceedings of the National Academy of Sciences*, 2018, **115**, 8883-8888.
212. O. Silberbush, M. Engel, I. Sivron, S. Roy and N. Ashkenasy, *The Journal of Physical Chemistry B*, 2019, **123**, 9882-9888.
213. K.-i. Otake, K. Otsubo, T. Komatsu, S. Dekura, J. M. Taylor, R. Ikeda, K. Sugimoto, A. Fujiwara, C.-P. Chou and A. W. Sakti, *Nature communications*, 2020, **11**, 1-7.
214. M. J. Strauss, M. Jia, A. M. Evans, I. Castano, R. L. Li, X. Aguilar-Enriquez, E. K. Roesner, J. L. Swartz, A. D. Chavez and A. E. Enciso, *Journal of the American Chemical Society*, 2021.
215. S. Chandra, T. Kundu, S. Kandambeth, R. BabaRao, Y. Marathe, S. M. Kunjir and R. Banerjee, *Journal of the American Chemical Society*, 2014, **136**, 6570-6573.
216. E. M. Ahmed, *Journal of advanced research*, 2015, **6**, 105-121.
217. O. Wichterle and D. Lim, *Nature*, 1960, **185**, 117-118.
218. J. Li and D. J. Mooney, *Nature Reviews Materials*, 2016, **1**, 1-17.
219. A. Gupta, M. Kowalczyk, W. Heaselgrave, S. T. Britland, C. Martin and I. Radecka, *European Polymer Journal*, 2019, **111**, 134-151.
220. T. Distler and A. R. Boccaccini, *Acta Biomaterialia*, 2020, **101**, 1-13.
221. N. Eslahi, M. Abdorahim and A. Simchi, *Biomacromolecules*, 2016, **17**, 3441-3463.
222. H. Yuk, S. Lin, C. Ma, M. Takaffoli, N. X. Fang and X. Zhao, *Nature communications*, 2017, **8**, 1-12.

223. X. Le, W. Lu, J. Zhang and T. Chen, *Advanced Science*, 2019, **6**, 1801584.
224. K. C. Spencer, J. C. Sy, K. B. Ramadi, A. M. Graybiel, R. Langer and M. J. Cima, *Scientific reports*, 2017, **7**, 1-16.
225. Y. Cho, S. Park, J. Lee and K. J. Yu, *Advanced Materials*, 2021, 2005786.
226. A. Vedadghavami, F. Minooei, M. H. Mohammadi, S. Khetani, A. R. Kolahchi, S. Mashayekhan and A. Sanati-Nezhad, *Acta biomaterialia*, 2017, **62**, 42-63.
227. M. Jia, J. Kim, T. Nguyen, T. Duong and M. Rolandi, *Biopolymers*, 2021, e23433.
228. C. Yang and Z. Suo, *Nature Reviews Materials*, 2018, **3**, 125.
229. K. Nyamayaro, P. Keyvani, F. D’Acierno, J. Poisson, Z. M. Hudson, C. A. Michal, J. D. Madden, S. G. Hatzikiriakos and P. Mehrkhodavandi, *ACS Applied Materials & Interfaces*, 2020, **12**, 52182-52191.
230. M.-J. Yin, Z. Yin, Y. Zhang, Q. Zheng and A. P. Zhang, *Nano Energy*, 2019, **58**, 96-104.
231. D. Gao and P. S. Lee, *Science*, 2020, **367**, 735-736.
232. J. Selberg, M. Jafari, J. Mathews, M. Jia, P. Pansodtee, H. Dechiraju, C. Wu, S. Cordero, A. Flora and N. Yonas, *Advanced Intelligent Systems*, 2020, **2**, 2000140.
233. D. Caccavo, *International journal of pharmaceuticals*, 2019, **560**, 175-190.
234. Y. Guo, X. Zhou, F. Zhao, J. Bae, B. Rosenberger and G. Yu, *ACS nano*, 2019, **13**, 7913-7919.
235. Y. Zhou, C. Wan, Y. Yang, H. Yang, S. Wang, Z. Dai, K. Ji, H. Jiang, X. Chen and Y. Long, *Advanced Functional Materials*, 2019, **29**, 1806220.
236. S. Durmaz and O. Okay, *Polymer*, 2000, **41**, 3693-3704.
237. K. McAvoy, D. Jones and R. R. S. Thakur, *Pharmaceutical research*, 2018, **35**, 1-17.
238. N. Yan, D. R. Paul and B. D. Freeman, *Polymer*, 2018, **146**, 196-208.
239. K. Nalampang, R. Panjakha, R. Molloy and B. J. Tighe, *Journal of Biomaterials Science, Polymer Edition*, 2013, **24**, 1291-1304.



240. E. Zygadło-Monikowska, Z. Florjańczyk, E. Wielgus-Barry and E. Hildebrand, *Journal of power sources*, 2006, **159**, 392-398.
241. E. Karadağ, A. Nalbantoğlu, S. Kundakçı and Ö. B. Üzüm, *Polymer-Plastics Technology and Engineering*, 2014, **53**, 54-64.
242. A. Bhattacharyya, C. O'Bryan, Y. Ni, C. D. Morley, C. R. Taylor and T. E. Angelini, *Biotribology*, 2020, **22**, 100125.
243. P. J. Flory, *Principles of polymer chemistry*, Cornell University Press, 1953.
244. H. Chavda and C. Patel, *International journal of pharmaceutical investigation*, 2011, **1**, 17.
245. H. Omidian, J. G. Rocca and K. Park, *Journal of controlled release*, 2005, **102**, 3-12.
246. A. A. Garrouch, L. Ali and F. Qasem, *Industrial & engineering chemistry research*, 2001, **40**, 4363-4369.
247. K. Hormann, V. Baranau, D. Hlushkou, A. Höltzel and U. Tallarek, *New Journal of Chemistry*, 2016, **40**, 4187-4199.
248. M. Hua, S. Wu, Y. Jin, Y. Zhao, B. Yao and X. He, *Advanced Materials*, 2021, 2100983.
249. B. M. O'Connell, T. M. McGloughlin and M. T. Walsh, *Biomedical engineering online*, 2010, **9**, 1-16.
250. Y. Guy, A. H. Faraji, C. A. Gavigan, T. G. Strein and S. G. Weber, *Analytical chemistry*, 2012, **84**, 2179-2187.
251. D. S. Adams, A. Masi and M. Levin, *Development*, 2007, **134**, 1323-1335.
252. M. Levin, J. Selberg and M. Rolandi, *iScience*, 2019.
253. J. Leger, M. Berggren and S. Carter, *Iontronics: Ionic carriers in organic electronic materials and devices*, CRC Press, 2016.
254. G. Tarabella, F. M. Mohammadi, N. Coppede, F. Barbero, S. Iannotta, C. Santato and F. Cicoira, *Chemical Science*, 2013, **4**, 1395-1409.
255. J. Selberg, M. Gomez and M. Rolandi, *Cell Systems*, 2018, **7**, 231-244.
256. M. Nishizawa, *Bulletin of the Chemical Society of Japan*, 2018, **91**, 1141-1149.

257. J. Isaksson, P. Kjäll, D. Nilsson, N. Robinson, M. Berggren and A. Richter-Dahlfors, *Nature materials*, 2007, **6**, 673-679.
258. C. Zhong, Y. Deng, A. F. Roudsari, A. Kapetanovic, M. Anantram and M. Rolandi, *Nature communications*, 2011, **2**, 1-5.
259. E. E. Josberger, Y. Deng, W. Sun, R. Kautz and M. Rolandi, *Advanced materials*, 2014, **26**, 4986-4990.
260. Z. Hemmatian, S. Keene, E. Josberger, T. Miyake, C. Arboleda, J. Soto-Rodríguez, F. Baneyx and M. Rolandi, *Nature communications*, 2016, **7**, 1-8.
261. T. Jiang, A. Hall, M. Eres, Z. Hemmatian, B. Qiao, Y. Zhou, Z. Ruan, A. D. Couse, W. T. Heller and H. Huang, *Nature*, 2020, **577**, 216-220.
262. Z. Hemmatian, R. H. Tunuguntla, A. Noy and M. Rolandi, *PloS one*, 2019, **14**.
263. J. Soto-Rodríguez, Z. Hemmatian, E. E. Josberger, M. Rolandi and F. Baneyx, *Advanced Materials*, 2016, **28**, 6581-6585.
264. X. Strakosas, J. Selberg, X. Zhang, N. Christie, P. H. Hsu, A. Almutairi and M. Rolandi, *Advanced Science*, 2019, **6**, 1800935.
265. Z. Hemmatian, E. Jalilian, S. Lee, X. Strakosas, A. Khademhosseini, A. Almutairi, S. R. Shin and M. Rolandi, *ACS applied materials & interfaces*, 2018, **10**, 21782-21787.
266. N. a. M. Yunus, R. Bellomo, D. Story and J. Kellum, *Critical care*, 2010, **14**, 226.
267. V. Dam, M. Zevenbergen and R. Van Schaijk, *Procedia engineering*, 2015, **120**, 237-240.
268. P. J. White and M. R. Broadley, *Annals of Botany*, 2001, **88**, 967-988.
269. D. Arosio and G. M. Ratto, *Frontiers in cellular neuroscience*, 2014, **8**, 258.
270. A. Hodgkin and P. Horowicz, *The Journal of physiology*, 1959, **148**, 127.
271. D. Blackiston, D. S. Adams, J. M. Lemire, M. Lobikin and M. Levin, *Disease models & mechanisms*, 2011, **4**, 67-85.
272. D. J. Blackiston, G. M. Anderson, N. Rahman, C. Bieck and M. Levin, *Neurotherapeutics*, 2015, **12**, 170-184.

273. G. J. Janz and D. J. Ives, *Annals of the New York Academy of Sciences*, 1968, **148**, 210-221.
274. G. Inzelt, in *Handbook of Reference Electrodes*, Springer, 2013, pp. 331-332.
275. M. A. Climent-Llorca, E. Viqueira-Pérez and M. M. López-Atalaya, *Cement and Concrete Research*, 1996, **26**, 1157-1161.
276. F. Pargar, H. Kolev, D. A. Koleva and K. van Breugel, *Journal of materials science*, 2018, **53**, 7527-7550.
277. Y. Ikeuchi, H. Kogiso, S. Hosogi, S. Tanaka, C. Shimamoto, T. Inui, T. Nakahari and Y. Marunaka, *The Journal of Physiological Sciences*, 2018, **68**, 191-199.
278. J. Wang, X. Wu, C. Chon, T. Gonska and D. Li, *Measurement Science and Technology*, 2012, **23**, 025701.
279. Y. Abbas, D. B. de Graaf, W. Olthuis and A. van den Berg, *Analytica chimica acta*, 2014, **821**, 81-88.
280. J. Peng, Y. Deng, D. Wang, X. Jin and G. Z. Chen, *Journal of Electroanalytical Chemistry*, 2009, **627**, 28-40.
281. I.-Y. Huang, R.-S. Huang and L.-H. Lo, *Sensors and Actuators B: Chemical*, 2003, **94**, 53-64.
282. G. Tarabella, C. Santato, S. Y. Yang, S. Iannotta, G. G. Malliaras and F. Cicoira, *Applied Physics Letters*, 2010, **97**, 205.
283. Y. Deng, D. Wang, W. Xiao, X. Jin, X. Hu and G. Z. Chen, *The Journal of Physical Chemistry B*, 2005, **109**, 14043-14051.
284. B. J. Polk, A. Stelzenmuller, G. Mijares, W. MacCrehan and M. Gaitan, *Sensors and Actuators B: Chemical*, 2006, **114**, 239-247.
285. N. Elgrishi, K. J. Rountree, B. D. McCarthy, E. S. Rountree, T. T. Eisenhart and J. L. Dempsey, *Journal of Chemical Education*, 2018, **95**, 197-206.
286. J.-M. Savéant, *Willey-VCH, New Jersey*, 2006.
287. A. J. Bard and L. R. Faulkner, *Electrochemical Methods*, 2001, **2**, 580-632.
288. N. Berezina, N. Kononenko, O. Dyomina and N. Gnusin, *Advances in colloid and interface science*, 2008, **139**, 3-28.

289. J. L. Whited and M. Levin, *Current opinion in genetics & development*, 2019, **57**, 61-69.
290. M. Levin, G. Pezzulo and J. M. Finkelstein, *Annual review of biomedical engineering*, 2017, **19**, 353-387.
291. A. Shiozaki, E. Otsuji and Y. Marunaka, *World Journal of Gastrointestinal Oncology*, 2011, **3**, 119.
292. Y. Xu, P. Zou and A. E. Cohen, *Current opinion in chemical biology*, 2017, **39**, 1-10.
293. S. Almeida, Z. Zhang, G. Coppola, W. Mao, K. Futai, A. Karydas, M. D. Geschwind, M. C. Tartaglia, F. Gao, D. Gianni, M. Sena-Esteves, D. H. Geschwind, B. L. Miller, R. V. Farese, Jr. and F. B. Gao, *Cell Rep*, 2012, **2**, 789-798.
294. J. Marh, Z. Stoytcheva, J. Urschitz, A. Sugawara, H. Yamashiro, J. B. Owens, I. Stoytchev, P. Pelczar, R. Yanagimachi and S. Moisyadi, *Proc Natl Acad Sci U S A*, 2012, **109**, 19184-19189.
295. A. D. Mickle, S. M. Won, K. N. Noh, J. Yoon, K. W. Meacham, Y. Xue, L. A. McIlvried, B. A. Copits, V. K. Samineni and K. E. Crawford, *Nature*, 2019, **565**, 361-365.
296. J. Kim, R. Ghaffari and D.-H. Kim, *Nature Biomedical Engineering*, 2017, **1**, 1-4.
297. Y. Deng, E. Josberger, J. Jin, A. F. Roudsari, B. A. Helms, C. Zhong, M. Anantram and M. Rolandi, *Scientific reports*, 2013, **3**, 2481.
298. J. Zhu, *Biomaterials*, 2010, **31**, 4639-4656.
299. M. Mehrali, A. Thakur, C. P. Pennisi, S. Talebian, A. Arpanaei, M. Nikkhah and A. Dolatshahi-Pirouz, *Advanced Materials*, 2017, **29**, 1603612.
300. E. A. Kamoun, E.-R. S. Kenawy and X. Chen, *Journal of advanced research*, 2017, **8**, 217-233.
301. A. Tseng and M. Levin, *Communicative & Integrative Biology*, 2013, **6**, 13192-13200.
302. M. Chesler, *Physiological reviews*, 2003, **83**, 1183-1221.

303. D. S. Adams, S. G. Uzel, J. Akagi, D. Wlodkowic, V. Andreeva, P. C. Yelick, A. Devitt-Lee, J. F. Pare and M. Levin, *The Journal of physiology*, 2016, **594**, 3245-3270.
304. L. N. Vandenberg, R. D. Morrie and D. S. Adams, *Developmental Dynamics*, 2011, **240**, 1889-1904.
305. M. Jia, S. Ray, R. Breault and M. Rolandi, *APL Materials*, 2020, **8**, 120704.
306. J. Selberg, M. Jafari, C. Bradley, M. Gomez and M. Rolandi, *APL Materials*, 2020, **8**, 120904.
307. M. Jafari, G. Marquez, J. Selberg, M. Jia, H. Dechiraju, P. Pansodtee, M. Teodorescu, M. Rolandi and M. Gomez, *IEEE Control Systems Letters*, 2020.
308. P. Pansodtee, J. Selberg, M. Jia, M. Jafari, H. Dechiraju, T. Thomsen, M. Gomez, M. Rolandi and M. Teodorescu, *arXiv preprint arXiv:2105.09810*, 2021.
309. J. R. Choi, K. W. Yong, J. Y. Choi and A. C. Cowie, *BioTechniques*, 2019, **66**, 40-53.
310. W.-C. Huang, F. Ali, J. Zhao, K. Rhee, C. Mou and C. J. Bettinger, *Biomacromolecules*, 2017, **18**, 1162-1171.